

Mechanisms of diffusion in nuclear pore complex mimics

by

Laura K. Maguire

B.S., Harvey Mudd College, 2013

A thesis submitted to the
Faculty of the Graduate School of the
University of Colorado in partial fulfillment
of the requirements for the degree of
Doctor of Philosophy
Department of Physics
2019

This thesis entitled:
Mechanisms of diffusion in nuclear pore complex mimics
written by Laura K. Maguire
has been approved for the Department of Physics

Assistant Professor Loren Hough

Professor Meredith Betterton

Date _____

The final copy of this thesis has been examined by the signatories, and we find that both the content and the form meet acceptable presentation standards of scholarly work in the above mentioned discipline.

Maguire, Laura K. (Ph.D., Physics)

Mechanisms of diffusion in nuclear pore complex mimics

Thesis directed by Assistant Professor Loren Hough

Placeholder text for abstract.

Dedication

Nice dedication goes here.

Acknowledgements

There are lots of people to acknowledge.

Contents

Chapter

1	Introduction	1
1.1	Intrinsically disordered proteins are essential to cellular function	1
1.2	Major components of nucleocytoplasmic transport	2
1.2.1	Scaffold nucleoporins are ordered and form ringlike complexes.	3
1.2.2	FG nucleoporins are disordered and fill the central channel of the pore. . . .	3
1.2.3	Energy for selective transport is provided by the Ran cycle.	4
1.2.4	Transport factors	5
1.3	Observed features of nucleocytoplasmic transport	6
1.3.1	Flux through the NPC is very high.	6
1.3.2	TFs show millisecond dwell times.	7
1.3.3	TF-FG Nup binding kinetics are ultrafast.	7
1.3.4	Passive permeability barrier	7
1.3.5	Effect of transport factors	8
1.3.6	Permeability barrier/flux studies	8
1.4	Theoretical models of the NPC	8
1.4.1	Entropic barrier model	8
1.4.2	Hydrogel model	9
1.4.3	Forest/intermediate models	9
1.4.4	Effect of crowding	9

1.4.5	Effect of transport factors	9
1.4.6	Energy landscape models	9
1.5	Synthetic NPCs have seen limited success.	10
1.5.1	Gold nanopores (Rout group)	10
1.5.2	Hydrogels (Gorlich)	10
1.5.3	Other models (peptide hydrogels, DNA origami, etc)	10
1.6	Conclusions of introduction?	11
2	Modeling	12
2.1	Biophysical model of transport through the NPC	13
2.1.1	No selective transport occurs if bound TFs are immobile	15
2.1.2	Bound-state diffusion allows selective transport	16
2.2	Mechanisms of bound transport factor mobility	17
2.2.1	FG Nup flexibility allows tethered diffusion	18
2.2.2	Inter-chain hopping increases selectivity	20
2.2.3	Detailed explanation of hopping simulation	21
2.2.4	Hopping simulation results	23
2.2.5	Fickian diffusion	23
2.3	Discussion	24
2.3.1	Overcoming the limitations of binding	25
2.3.2	Design principles of selective transport by binding	26
3	Hydrogel design for protein separation	27
3.1	Hydrogel fabrication	28
3.2	Flow chamber fabrication	33
3.3	Hydrogel geometries	37
3.4	FSFG	39
3.5	Pore size	39

3.6	Porogens	40
3.6.1	Alginate nanospheres	41
3.6.2	Dextran/dextranase porogen system	43
3.7	Polymerization using confocal microscope	47
3.8	Nup and transport factor constructs	53
3.8.1	SSSG negative control	53
3.8.2	Covalently-tethered NTF2 dimer	54
3.8.3	NTF2-GFP	55
3.8.4	Kap121 and NLS-GFP	55
3.8.5	FSFG concat 2 and concat 3	56
3.9	Dye-labeling and free dye	58
3.9.1	Labeling NTF2 with fluorescein-NHS	58
3.9.2	Labeling NTF2 with Alexa Fluor 488 - SDP	60
3.9.3	Labeling NTF2-cys or FSFG-cys with Alexa Fluor 488 - maleimide	61
4	Bound diffusion measurements	65
4.1	Experimental setup	65
4.1.1	Hydrogels	65
4.1.2	Influx experiments	66
4.1.3	Fluorescence recovery after photobleaching	66
4.2	Influx analysis	67
4.2.1	Profile analysis	68
4.2.2	Accumulation analysis	69
4.2.3	Gel dimension estimations	69
4.2.4	Partition coefficient and bound probability calculations	70
4.2.5	Bound-diffusion calculation	71
4.3	FRAP analysis	71

4.4 Discussion	71
5 FG Nup aggregation under crowded conditions	72
5.1 Results	73
5.1.1 Thioflavin timecourses	73
5.1.2 Fluorimetry	78
5.2 Discussion	80
5.3 Materials and Methods	80
5.3.1 Buffers	80
5.3.2 FG124 preparation	81
5.3.3 Timecourse preparation	81
5.3.4 NMR sample preparation	82
5.3.5 NMR experiments	82
5.3.6 Fluorimetry	82
Bibliography	83
Appendix	
A Appendix test	88

Tables**Table**

2.1 Comparison between experimental results for NTF2 and GFP (a similarly-sized non-binding protein) and model predictions. Flux measured in units of molecules per pore per second.	17
5.1 FG124 aggregation lifetime and lag time with varying pH. Each condition run with 6 replicates in PTB buffer. One-way ANOVAs show no statistically significant differences between conditions. Standard errors are shown.	76

Figures

Figure

- 2.1 Schematics of the nuclear-pore complex and model. (A) The nuclear pore complex (gray) is filled with FG Nups (green polymers) that selectively passage transport factors that bind to FG Nups (blue) while blocking non-binding proteins (red). The central channel of the pore has length L . Protein concentration is high on the left (inlet) and low on the right (outlet). (B) Selectivity quantifies the degree of selective transport through the pore. A non-selective pore with $S = 1$ has the same flux for a transport factor as for a non-binding protein (top). A selective pore with $S > 1$ has a larger flux for a transport factor than a non-binding protein (lower). (C) The bound diffusion coefficient quantifies the mobility of a bound transport factor. A transport factor may be immobile (top) or mobile (lower) when bound. 12
- 2.2 Flux through the pore and selectivity for TFs with varying bound mobility. (A) Flux as a function of time when TFs are immobile while bound, with varying binding affinity as in (B). (B) Flux as a function of time when TFs are mobile while bound with $D_B = D_F$, with varying binding affinity. (C) Selectivity as a function of dissociation constant with varying bound diffusion coefficient. 14

2.3	(A) Schematic of the flexible tether model of bound-state diffusion. FG Nups are treated as entropic springs that constrain the motion of TFs more (top and center left, longer FG Nup) or less (top and center right, shorter Nup), which corresponds to changing width of the harmonic potential well (lower). (B) Ratio of bound to free diffusion coefficient as a function of dissociation constant, with varying polymer length in the tethered-diffusion model. (C) Selectivity as a function of K_D , with varying polymer length in the tethered-diffusion model.	16
2.4	(A) Schematic of the inter-chain hopping model of bound-state diffusion. FG Nups are treated as entropic springs that constrain the motion of TFs, and inter-chain hopping allows a TF to move from one FG Nup (top and center left, green Nup) to another (top and center right, red Nup) without unbinding, which corresponds to switching from one harmonic potential well to another (lower). (B) Ratio of bound to free diffusion coefficient as a function of dissociation constant, with varying hopping rate in the inter-chain hopping model. (C) Selectivity as a function of K_D with varying hopping rate. FG Nup contour length $L_c = 40$ nm in (B, C).	20
2.5	(A) Examples of mean-squared displacement (MSD) of a simulated TF in the inter-chain hopping model, with varying hopping rate. (B) Examples of MSD distributions $\rho_{\text{MSD}}(t)$ used in estimating the diffusion coefficient, with varying unbinding rate. Tethers have 40 nm contour length; other parameters are as discussed in the text.	23
2.6	Bound diffusion and selectivity as a function of dissociation constant, with varying hopping rate for FG Nups with $L_c = 4$ nm.	24
2.7	Bound diffusion and selectivity as a function of dissociation constant, with varying hopping rate for FG Nups with $L_c = 12$ nm.	25
2.8	Bound diffusion and selectivity as a function of dissociation constant, with varying hopping rate for FG Nups with $L_c = 120$ nm.	26

3.1 Overview of hydrogel fabrication and fluorescent protein influx. A precursor solution is mixed, containing hydrogel monomers, crosslinkers, a photoinitiator, and the Nup fragment. Upon exposure to UV light, the precursor solution crosslinks, and one end of each Nup is conjugated to the hydrogel. The diffusion of a fluorescently-tagged transport factor can then be compared to that of a similarly-sized inert fluorescent protein.	29
3.2 Chemical structures of monomers and crosslinkers for PEG and acrylamide hydrogels. The total molecular weight of the 8-armed PEG-norbornene was 20 kD, and either a 1-kD or 8-kD PEG dithiol crosslinker was used. Structures from Sigma and CreativePEGWorks.	31
3.3 Absorption spectra of (A) Irgacure 2959 and (B) LAP (solid lines) and with that of their cleavage products (dotted lines) [43]. (C) Chemical structures of the APS/TEMED crosslinking system. Structures from Sigma.	32
3.4 Procedure for photopolymerization with (A) or without (B) a photomask. (A) A flow chamber is filled with precursor solution. The photomask is placed to hide all areas that should not be crosslinked, and the chamber is exposed to UV illumination. Excess precursor solution is removed with a buffer rinse. (B) Microliter droplets of precursor solution are pipetted onto the slide surface before the chamber is assembled. After assembly, the chamber is exposed to UV illumination. The chamber is then filled with buffer.	34
3.5 Flow chamber design and geometries. (A) Schematic of the most common flow chamber, showing slide, coverslip, gasket, ports, and hydrogels. (B)-(F) Common hydrogel geometries. Those in the left-hand column are suitable for selectivity measurements as well as diffusion measurements, while the right-hand column cannot be used to measure selectivity.	34

3.6 Microfluidic sticker fabrication from [44]. (A) A PDMS mold is used to shape an NOA droplet on a flat slide. The NOA is briefly cured but retains a sticky surface. (B) NOA can also be wicked into a PDMS mold. (C) The NOA sticker is placed onto a permanent surface, sealed, and cured entirely.	36
3.7 Alginate crosslinking from [46]. Alginate is composed of alternating guluronate (G) and manuronate (M) blocks. Addition of calcium ions leads to an “egg-box” crosslinked structure. Add a cartoon of spheres in our gel (with positive poly-L-lysine coating around negative alginate gel) and the spaces they should leave upon depolymerization.	41
3.8 Exit of fluorescent dextran from hydrogels after digestion with dextranase.	44
3.9 Dextranase digestion of FSFG	45
3.10 Accumulation of fluorescent proteins in gels treated with dextranase.	46
3.11 Suppression of mCherry in control gels that were in the presence of dextranase, dextran, and dextran digestion products (maltose).	47
3.12 Image of laser-written hydrogels. (A) Ring hydrogels containing no Nups. Reservoir contains 20 μM NTF2-A488 and mCherry. (B) Line hydrogels containing FSFG-A647. Reservoir contains precursor solution with FSFG-A647. Photobleaching within gel by 405 nm laser is evident.	49
3.13 Sample (A) accumulation and (B) intensity profile plots for a 50 μm thick confocal-crosslinked ring nominally containing 10 mg/mL FSFG. Intensity normalized to inlet reservoir. Inlet contains 25 μM NTF2-Alexa488 and mCherry in PTB.	49
3.14 Images of laser-written hydrogels nominally containing 10 mg/mL FSFG. Reservoirs contain 20 μM NTF2-A488 and mCherry. (A) Hydrogel ring, likely with lightly-crosslinked inner reservoir. (B) Hydrogel bar separating large inlet and small outlet.	50

3.15 Effect of dwell time and loop number on edge-dip effect in equilibrated, confocal-crosslinked ring hydrogels. Nominal FSFG concentration is 10 mg/mL. Reservoirs contain 20 <i>μM</i> NTF2-A488 and mCherry in PTB. Intensity profiles are shown for a hydrogel polymerized with $t_{\text{dwell}} = 1/32$ and two loops (solid lines) and a hydrogel polymerized with $t_{\text{dwell}} = 1$ and 64 loops.	51
3.16 Comparison of intensity profiles for SSSG and no-nup (control) gels.	54
3.17 Intensity profile for GFP-NTF2 and mCherry showing no binding to FSFG hydrogel. .	55
3.18 Cartoon of various NTF2 constructs	56
3.19 SDS-PAGE showing Kap121 purification (purified by Chris Lawton), picture of influx, intensity profiles	57
5.1 Sample sigmoid fit. Look up conditions. (Pulled this from Sophie's thesis but I did the fit)	74
5.2 test	75
5.3 test	77
5.4 Emission scan of fresh and aggregated FG124 in crowded conditions. Data normalized by subtracting blank sample.	78
5.5 Emission scan of phenylalanine, FSFG, and FG124. Excited at 240 nm. Phe data is not mine, need to check reference. Data normalized to a maximum amplitude of 1. .	79
5.6 Emission scan of phenylalanine, FSFG, and FG124. Excited at 240 nm. Phe data is not mine, need to check reference. Data normalized to a maximum amplitude of 1. .	79
5.7 Absorbance of 5% PEG and PVP solutions in PTB. Normalized by subtracting PTB absorbance.	80

Chapter 1

Introduction

1.1 Intrinsically disordered proteins are essential to cellular function

For decades, it was conventional wisdom among biologists that a protein's folded shape determined its function. Most enzymes and other proteins that were studied had a stable folded configuration, the lowest point on a well-defined folding energy landscape. A protein's conformation provided specific docking points through which it could interact with ligands or other proteins in a "lock-and-key" model.

However, a few decades ago, it began to become clear that not all proteins have a well-defined ternary or even secondary structure, but rather exist as extended polymer chains. These intrinsically disordered proteins (IDPs) were initially dismissed as nonfunctional, but evidence began to accumulate that they were in fact essential for cellular function, overturning the structure-function paradigm [?]. Their roles and importance are still being understood, as are the unusual mechanisms by which they accomplish their functions without a well-defined structure.

Today, it is estimated that 30% of eukaryotic proteins are disordered or contain significant disordered regions [?]. While there is significant sequence heterogeneity among IDPs, they tend to contain a large proportion of hydrophilic residues, and often have long stretches of low-complexity regions where only a few amino acids are represented. They also often have high net charge.

Some IDPs fold (or partially fold) upon binding with an ordered partner, while others form

“fuzzy” complex that remains disordered. Their advantages over folded proteins may include their plasticity, which enables them to bind many different binding partners. Multivalency, either as one-to-many or many-to-one binding, may also play a role. They may act as hubs that bring together larger complexes. Similarly, IDPs are often known for having high specificity at relatively weak binding strengths [?].

While the normal functioning of IDPs is very important to the cell, IDPs are also prone to aggregation and are at the root of pathologies such as Alzheimer’s disease, Parkinsons, and prion diseases. Often, normally-disordered proteins aggregate into amyloid fibrils, a stable structure based on parallel beta-sheets.

IDPs are commonly involved in cell signaling and regulation [?]. Their disordered nature makes them useful as hubs that bring together many other proteins, and as scaffolds that many proteins can bind to at once. IDPs appear to be prevalent in transcriptional regulation, and they are playing increasingly apparent roles in liquid-liquid phase separation within cells. One of the most fascinating examples of IDP function is in the nuclear pore complex (NPC), a unique selective barrier that regulates all transport between the nucleus and the cytoplasm. The link between disorder and selectivity is not well understood in this case.

1.2 Major components of nucleocytoplasmic transport

The nuclear pore complex (NPC) resides in the nuclear envelope of eukaryotes and regulates all macromolecular traffic between the nucleus and cytoplasm. The NPC is one of the largest protein complexes in the cell, at about 60 MDa in yeast and 120 MDa in humans [1]. As the regulator of nucleocytoplasmic transport, the NPC must rapidly and specifically pass a wide array of macromolecules: transcription factors into the nucleus, and RNA into the cytoplasm. Moreover, it must be robust to problems and able to accomodate mechanical strain as the nuclear envelope changes shape, and to passage large cargo.

A typical yeast cell has xx nuclear pores, each with a dimension of xx. Human cells have about xx pores with xx dimensions.

There are about 30 different types of Nups, all present in multiple copy numbers.

These functions are accomplished through a structure with two main parts, both made of proteins known as nucleoporins, or Nups: the scaffold Nups, which form a ringlike complex, and the FG Nups, which are disordered and fill the central channel created by the scaffold Nups. Aside from the NPC itself, transport factors (TFs) are a class of proteins essential for selective transport. The energetic cost of selectivity is captured in the Ran GTP/GDP cycle.

1.2.1 Scaffold nucleoporins are ordered and form ringlike complexes.

The nuclear pore itself is formed of scaffold Nups, which are ordered proteins that form ringlike complexes with eightfold symmetry [1]. There is an inner ring and two outer rings, the nuclear and cytoplasmic rings. The outer rings are slightly larger. The nuclear ring is on the side of the nucleus and includes the nuclear basket. The cytoplasmic ring includes the cytoplasmic filaments, which are (probably?) disordered proteins extending out into the cytoplasm.

The eightfold symmetry of the pore arises from its modular nature. Scaffold Nups form various stable subcomplexes, of which one of the most important is the Y-complex. The Y-complex forms the inner ring; there are 32 copies of the complex per pore [1]. The rings themselves are relatively flexible, as they need to be in order to accommodate deformations of the nuclear envelope. This flexibility is achieved in part by through short linear motifs (SLMs) which connect the subcomplexes to each other.

Recent cryo-EM studies have achieved unprecedented resolution of the scaffold Nups [?, ?].

1.2.2 FG nucleoporins are disordered and fill the central channel of the pore.

The central channel of the pore is filled with disordered FG nucleoporins (FG Nups). FG Nups typically consist of an ordered domain that anchors them to the wall of the channel, and an entirely disordered domain that extends into the channel. As with all Nups, FG Nups have eightfold symmetry in the pore, and some of them are present in much higher copy number.

The disordered portion of every FG Nup contains phenylalanine- glycine (FG) motifs which

bind to the hydrophobic binding pockets of transport factors. While there are multiple binding motifs, all are short sequences which incorporate an FG repeat; for instance, FSFG, GLFG, and others. [?]. Each FG Nup contains x-x FG repeats, leading to an extremely high density of FG repeats within the pore.

Since the FG Nups are disordered, most conventional visualization techniques do not work. When imaged over time or when several pores are imaged, the averaged results do not show the disordered portion of the FG Nups. Cryo-EM and x-ray crystallography don't work. Techniques such as NMR and very fast AFM can help gain insight into their conformational ensembles [?, ?]. Early research suggested that the FG Nups formed a central plug or "transporter", but more recent work suggests that there is no central structure, just disordered proteins (the AFM study from Lim or Lemke group). There is some evidence from simulations that the density of the FG Nups, as well as their charge density and hydrophobic properties, are not uniform along either the radial or axial directions [?, ?]. This may contribute to selective transport, although the pore still functioned with all of the asymmetric FG Nups removed. Indeed, the NPC is remarkably robust to FG Nup deletion. Over half of the mass of FG Nups can be removed without eliminating the selectivity barrier [1].

1.2.3 Energy for selective transport is provided by the Ran cycle.

Selective transport requires an energy source, which in the case of the NPC is provided by the Ran cycle. When a TF-cargo complex passes from the cytoplasm into the nucleus (nuclear import), it encounters a RanGTP on the nuclear side which binds to the TF and displaces the cargo. Then the TF-RanGTP complex can collect a cargo destined for nuclear export, and this ternary complex can diffuse back through the NPC to the cytoplasm. The protein RanGAP then hydrolyzes the RanGTP to RanGDP, disrupting the complex into its three original pieces. Ultimately, the energy source for selective nuclear transport comes from the RanGTP-RanGDP gradient from the cytoplasm to the nucleus, a gradient which is maintained partially by NTF2, which carries RanGDP through the pore [2].

From the perspective of transport, this means that the process of passing through the pore is itself passive and does not consume energy. The selectivity arises from concentration gradients maintained by the Ran cycle.

1.2.4 Transport factors

Transport factors (TFs) are ordered proteins that carry cargo through the NPC. While there are various types, they share several features in common, most notably the fact that all known transport factors have more than one hydrophobic binding pocket which binds to FG repeats. In fact, many TFs have several binding pockets. Likewise, the binding affinity between TFs and FG Nups remains unknown for most TFs. Estimates of dissociation constant K_D vary from nanomolar to millimolar, depending on the environment (cellular, buffer, etc.) in which the measurement is made [?]. There are many types of TF, of which some of the most important are the importins and exportins (karyopherins), NTF2, (and mRNA exporters? CRM? mex67?).

The karyopherins (Kaps) are the most-studied family of TFs. They are also known (in human cells?) as importins and exportins, or collectively as the importin β superfamily [3]. The twenty or so different Kaps are responsible for most nucleocytoplasmic transport [4]. Kaps typically consist of multiple HEAT repeats, a helical motif which conveys structural flexibility [5]. Most Kaps bind their cargo directly via a nuclear localization signal (NLS, for nuclear import) or nuclear export signal (NES, for nuclear export). NLS and NES are 5-7 amino acid tags found on cargo []. However, Kap95? (importin β) uses the adaptor protein Kap60? (importin α) to bind its cargo. In general, Kaps are on the order of 100 kDa in size, well above the passive permeability limit []. Kaps may contribute to the selectivity barrier.

Unlike the karyopherins, nuclear transport factor 2 (NTF2) does not transport a wide variety of cargo across the NPC. Instead, NFT2 is focused on maintaining the Ran gradient needed for transport. It transports RanGDP across the pore - why does this help maintain a gradient? If it transports in both directions, wouldn't it help wash out the gradient? NTF2 is a homodimer whose components are 14 kDa and have one FG binding site. Although its small size of 28 kDa is near

the 30 kDa cutoff for passive transit through the pore, its flux through the pore is still 30-150 that of similarly-sized proteins that do not bind to FG Nups.

There are other TFs such as Mex67 and CRM, but I don't really know what they do. Is RNA exported using Kaps or are there other TFs for that?

1.3 Observed features of nucleocytoplasmic transport

The nuclear pore has been the subject of investigation since the 1950s [?]. During that time, many different experimental techniques have been used, from in vivo studies to single molecule fluorescencence to SPR to NMR. Likewise, simulations have attempted to explain the selectivity properties of the NPC using a broad array of techniques, such as more or less coarse-grained molecular dynamics simulations. These studies together shed light on the mechanisms of selective transport, but are also all hindered by the small size and rapid timescale of transport. Many of the studies produce results that seem, at least at first glance, to contradict those of other studies. A comprehensive picture of the facts of nuclear transport has yet to emerge, although there are some universally accepted features.

1.3.1 Flux through the NPC is very high.

The high macromolecular traffic between nucleus and cytoplasm requires high flux through each NPC. Experiments with permeabilized cells estimate that the total molecular flow through the NPC could be as high as 10-20 MDa per pore per second, corresponding to roughly 1000 transport events per pore per second [6]. Experiments focusing particularly on NTF2 report fluxes between 50 and 250 molecules per pore per second [6-8]. Fluxes this high mean a continuously high occupancy of the NPC, estimated at around 100 karyopherins at once [9]. It is unclear whether the effect of crowding with TFs in the pore has an impact on selectivity.

1.3.2 **TFs show millisecond dwell times.**

One reason that individual NPCs can accommodate such high flux is the rapidity with which molecules transit the pore. A wide range of molecules, such as NTF2, Importin β , and GFP-NLS cargoes, have a dwell time of less than 10 ms in the pore [?, 3, 10, 11]. Typically, this is determined using single-molecule tracking with superresolution microscopy [3]. There is some evidence that a subpopulation of karyopherins resides in the pore over long timescales, potentially contributing to the selectivity barrier [4].

The flux through an NPC is determined not only by the transit time, but also by the success rate of transit attempts. Single-molecule microscopy suggests that the nuclear import efficiency of Importin β ranges from 50% to 80%, depending on concentration [?]. Modeling supports these numbers [12].

1.3.3 **TF-FG Nup binding kinetics are ultrafast.**

The short dwell time of transport factors and cargo at the pore contributes to a source of confusion in the NPC community: the binding kinetics of TFs and FG Nups. Measurements of dissociation constant K_D and its components k_{on} and k_{off} ($K_D = k_{\text{off}}/k_{\text{on}}$) span several orders of magnitude, depending on the measurement conditions. Original in vitro measurements, performed in buffer, show low K_D values in the nanomolar range, indicating tight binding between TFs and FG Nups. However, these values were not compatible with a transit time around 10 ms, as a typical binding event as calculated from the off-rate would last much longer than 10 ms.

More recent measurements are converging on a consensus that TF-FG Nup binding kinetics are in fact much faster than previously estimated. Diffusion-limited on-rates and K_D values around 1 mM would permit rapid transit through the pore.

1.3.4 **Passive permeability barrier**

There is a cutoff around 30 kDa where molecules stop being able to passively transit the pore at any appreciable rate. Work from the Timney lab suggests that the passive permeability barrier

is not a sharp cutoff, but broad.

Dwell times for various TFs and TF-cargo complexes has been studied in many cases, giving a typical dwell time of 5-10 ms, with a small minority of complexes spending much longer in the pore [3].

1.3.5 Effect of transport factors

The presence of transport factors may make the selectivity barrier more robust. SPR measurements as discussed above give estimates of layer compaction or extension, and populations of tight- or weak-binding TFs. Other studies (?) suggest that crowding with TFs might help reduce non-specific interactions and increase the selectivity of transport.

1.3.6 Permeability barrier/flux studies

People have measured the flux through the pore in vitro and in vivo in various ways. One group developed OSTR, where they seal an NPC to the pore of a membrane and measure fluorescence flux of TFs through that pore. The Gorlich group (Ribbeck) have permeabilized cells and injected fluorescent transport factors and watched how long it took them to localize to the nucleus. These measurements show selectivities of 20-150 (ish) fold flux of TFs as compared to inert proteins.

1.4 Theoretical models of the NPC

Many theoretical models exist, both qualitative and quantitative.

1.4.1 Entropic barrier model

The entropic barrier model postulates that Nups remain disordered within the pore (should talk about experimental evidence for and against). In this model, inert proteins are kept out of the pore through an entropic barrier, because their entry into the pore would restrict the possible conformations of the disordered Nups. TFs can get into the pore, in contrast, because the binding

energy offsets the entropic penalty. This is one of the two main qualitative models of the pore, the other being the hydrogel or selective phase model. The Rout lab supports this model. I think most labs other than the Gorlich lab are beginning to support this model, but I'm not sure.

1.4.2 Hydrogel model

The hydrogel model is the other main qualitative NPC model. The Gorlich group supports this model. This model postulates that the Nups interact via their FG motifs (discuss evidence in previous section, maybe?) and form a hydrogel. A dynamic hydrogel. Inert proteins are kept from passing through because they can't get through the gel mesh, but transport factors disrupt the crosslinks by binding to FGs and "melt" through.

1.4.3 Forest/intermediate models

This model proposes that a mix of the entropic barrier model and selective phase model are at play.

1.4.4 Effect of crowding

Some people (Zilman paper, etc) have modeled the effect of crowding on the selectivity barrier. A lot of overlap with effect of transport factors.

1.4.5 Effect of transport factors

Same as previous section sort of. Kap-centric models of the NPC (short for karyopherin-centric, for the class of TFs called karyopherins) propose that a permanent population of Kaps lives within the NPC. This strengthens the selectivity barrier.

1.4.6 Energy landscape models

Most quantitative models of the nuclear pore are energy landscape models. These are typically computational studies that require a fair amount of detail and assumptions about the pore. They

incorporate effects of charge, hydrophobicity, specific binding interactions, etc. Generally the result is a picture of the free energy landscape encountered by TFs and by inert proteins as they travel along the axis of the pore.

1.5 Synthetic NPCs have seen limited success.

Many different groups have attempted to make synthetic nuclear pore complexes, but they are generally not very successful.

1.5.1 Gold nanopores (Rout group)

One of Loren's colleagues in New York grafted FG Nups onto a gold-coated nanopore and monitored flux through the pore. She saw low (less than 10-fold) selectivity. I'm not sure whether other nanopore-based approaches have been tried.

1.5.2 Hydrogels (Gorlich)

The Gorlich group keeps making hydrogels out of Nups and testing the entry of various proteins. They take Nsp1 or fragments of it or other Nups that spontaneously form hydrogels in buffer, and let them form a gel. Then they introduce fluorescently-tagged TFs and inert proteins and monitor the progression of the fluorescent front into the gel. They see very high (100 or more) partition coefficients, indicating that the TFs really bind very strongly to the gel. They do not see rapid exit from the gel as would be required for rapid transport.

1.5.3 Other models (peptide hydrogels, DNA origami, etc)

There are a grab-bag of other models that I need to learn more about. Some groups have done similar things to what we want to do, making hydrogels out of non-aggregating Nup peptides and a pentameric crosslinking domain. There was a group that made an NPC ring out of DNA origami and attached Nups at particular points, though I'm not sure how that can be used to test selectivity because I can't see how to anchor the rings into a membrane.

1.6 Conclusions of introduction?

NPCs are interesting and important.

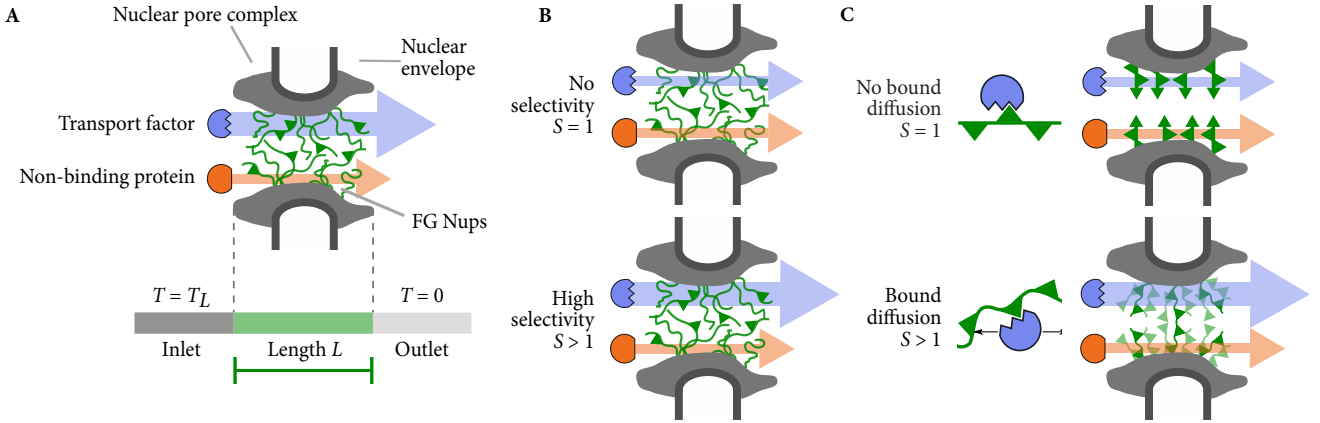


Figure 2.1: Schematics of the nuclear-pore complex and model. (A) The nuclear pore complex (gray) is filled with FG Nups (green polymers) that selectively pass transport factors that bind to FG Nups (blue) while blocking non-binding proteins (red). The central channel of the pore has length L . Protein concentration is high on the left (inlet) and low on the right (outlet). (B) Selectivity quantifies the degree of selective transport through the pore. A non-selective pore with $S = 1$ has the same flux for a transport factor as for a non-binding protein (top). A selective pore with $S > 1$ has a larger flux for a transport factor than a non-binding protein (lower). (C) The bound diffusion coefficient quantifies the mobility of a bound transport factor. A transport factor may be immobile (top) or mobile (lower) when bound.

Chapter 2

Modeling

Models of the NPC selective barrier have proposed that the FG Nups may form an entropic brush [13], a dynamic hydrogel [6,14], an intermediate state between a brush and gel [15], or liquid droplets [16]. These mechanisms may be modulated by spatial organization [?,17] and binding of TFs to multiple FG repeats [18,19]. Attempts to distinguish these models have been hindered by the pore's small size, the redundancy and multiple copies of FG Nups, and contradictory experimental results on FG Nups and TF binding [15]. Some FG Nup fragments form less-dynamic hydrogels *in vitro* [14], but remain highly dynamic within cells [20]. Molecular dynamics simulations find

highly dynamic FG Nups, though the degree and extent of motion depends on the affinity of FG repeats for each other and for TFs [15, 21]. Crowding and competition modulate affinity [?] and may contribute to selective transport [12]. However, the connection between the amino-acid level behavior of the FG-TF interaction and macroscopic transport selectivity remains unclear. Here we address the central contradiction of selective transport through the NPC: how does binding of TFs to FG Nups within the pore increase the flux rather than decreasing it [22, 23]?

Using a biophysical model, we demonstrate that TF diffusion and binding are sufficient for selective transport, as long as binding only partially immobilizes TFs. Binding increases the local concentration, and these molecules contribute to the flux if mobile. Thermally-driven diffusion of TFs bound to flexible tethers gives sufficient particle mobility to produce selectivity similar to experimental measurements. Tether flexibility also allows bound TFs to hop between tethers, further enhancing selectivity.

2.1 Biophysical model of transport through the NPC

We consider a minimal model of the central channel of the NPC containing FG Nups homogeneously anchored Figure 2.1. This model is sufficiently general to describe the common features of a range of biopolymer filters. The NPC, unlike most other biopolymer filters, has a wide capture area that may increase transport rates [24]. In order to focus on basic principles of transport, we neglect this effect. A varying free energy landscape along the axis of the NPC may play a role in selective transport [12, 25–27]. However, the NPC is robust to deletion of all asymmetric Nups and many Nup combinations, indicating that spatial variation in pore properties is not necessary [?, ?]. Experiments *in vitro* with simplified, homogeneous Nup composition produced selective transport [?, ?].

Rapid transport requires TF-FG Nup binding, while a protein similar to a TF but unable to bind FGs is excluded. Therefore, in our model we compare two proteins that are identical, except that one binds FG Nups and the other does not. As a model TF, we consider nuclear transport factor 2 (NTF2) [?]. NTF2 is small (~ 5 nm) relative to the diameter (~ 50 nm) and length of the pore

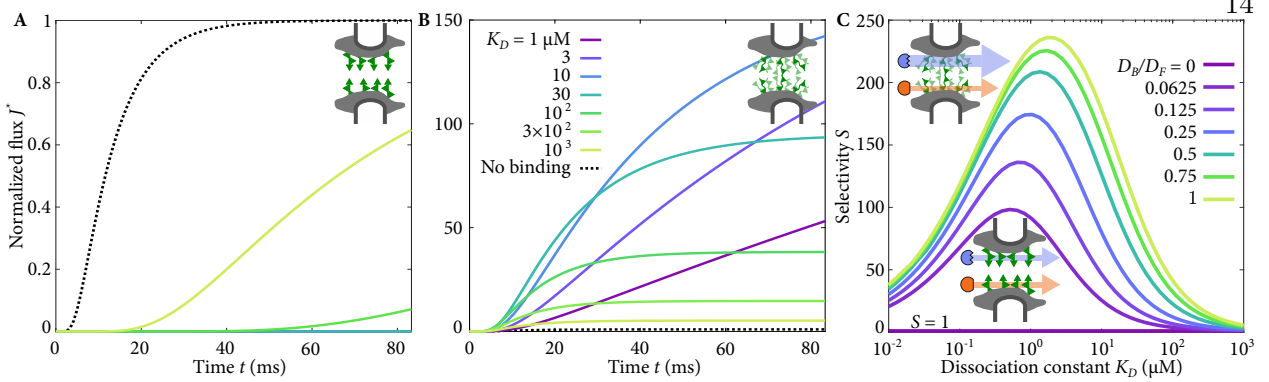


Figure 2.2: Flux through the pore and selectivity for TFs with varying bound mobility. (A) Flux as a function of time when TFs are immobile while bound, with varying binding affinity as in (B). (B) Flux as a function of time when TFs are mobile while bound with $D_B = D_F$, with varying binding affinity. (C) Selectivity as a function of dissociation constant with varying bound diffusion coefficient.

(~ 100 nm), suggesting that passage of NTF2 does not require large-scale molecular rearrangements that have been proposed for larger molecules [?, 18]. Because of the small size of NTF2 we neglect effects of steric crowding, which can enhance selectivity in a transport model [12]. NTF2 appears not to be actively released from the pore, suggesting that selective transport is an intrinsic property of the NPC [12, 28], and in contrast to actively released karyopherins [?, 18, 28, 29].

Transport through the NPC requires entry into the pore, passage, and exit. In single-molecule measurements, most of the transport time is spent in a random walk within the central channel [?, 26]. We therefore assume that entry and exit rates are determined by binding kinetics (see Supporting Information, section ?? for the model when entry and exit are rate-limiting.) The directional bias in TF transport is controlled outside the NPC through a concentration difference between the nucleus and cytoplasm generated by the Ran-GTP system [?]. In our model, we impose a fixed concentration difference across the pore.

We consider a channel of length L filled homogeneously with Nups that separates two reservoirs Figure 2.1A. Within the channel are free transport factor (concentration T), free FG Nups (N), and bound TF-FG complex (C), with total Nup concentration $N_t = N + C$. TF diffusion

within the channel ($0 < x < L$) is described by the reaction-diffusion equations

$$\frac{\partial T}{\partial t} = -k_{\text{on}}TN + k_{\text{off}}C + D_F \frac{\partial^2 T}{\partial x^2}, \quad (2.1)$$

$$\frac{\partial C}{\partial t} = k_{\text{on}}TN - k_{\text{off}}C + D_B \frac{\partial^2 C}{\partial x^2}. \quad (2.2)$$

TF-FG interaction has on-rate constant k_{on} , off-rate k_{off} , and dissociation constant $K_D = k_{\text{off}}/k_{\text{on}}$. We include competition between TFs for FG binding sites [27]. The diffusion constants of free (D_F) and bound (D_B) TFs are spatially constant. The fixed reservoir TF concentrations are T_L (inlet, left) and 0 (outlet, right).

The flux of transport factor out of the pore $J = -D_F \partial T / \partial x|_{x=L}$. We numerically integrated the full equations. Because flux measured in experiments is typically linearly proportional to TF concentration [16, 30], TF concentration likely remains below binding saturation in the NPC. Therefore, we also solved eqns. (2.1, 2.2) analytically in the low binding limit. We define the transport selectivity S as the ratio of steady-state flux of a binding versus a non-binding species

Figure 2.1B

$$S = \frac{J_{\text{binding}}(t \rightarrow \infty)}{J_{\text{non-binding}}(t \rightarrow \infty)}. \quad (2.3)$$

2.1.1 No selective transport occurs if bound TFs are immobile

If TF-FG Nup binding immobilizes the TF, the bound-state diffusion coefficient $D_B = 0$. For immobile bound TFs, transport is not selective: the steady-state flux $J = D_F T_L / L$ for both binding and non-binding proteins, so $S = 1$ (figs. 2.2, ??). The binding TF accumulates within the pore, but its immobility means it does not enhance transport compared to the non-binding case. Notably, this effect is independent of binding kinetics. Prior to steady state, binding slows transport Figure 2.2A. In systems such as airway mucus, immobilization may increase the time available for degradation or active clearance, consistent with the observation that binding tends to inhibit selective transport in those systems [?, ?, ?]. This effect is related to the binding-site barrier seen in antibody delivery to tumors [?], and observations that non-binding nanoparticles are often more effective in drug delivery to tumors than binding particles [23].

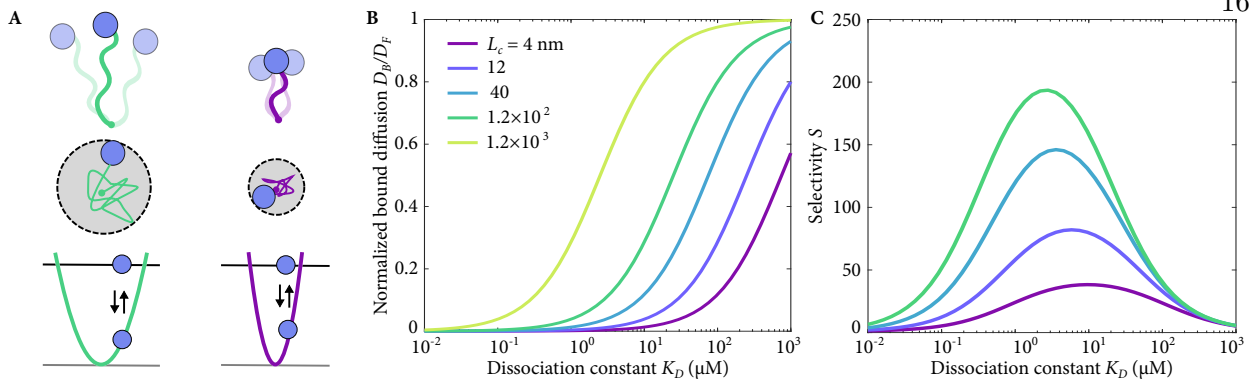


Figure 2.3: (A) Schematic of the flexible tether model of bound-state diffusion. FG Nups are treated as entropic springs that constrain the motion of TFs more (top and center left, longer FG Nup) or less (top and center right, shorter Nup), which corresponds to changing width of the harmonic potential well (lower). (B) Ratio of bound to free diffusion coefficient as a function of dissociation constant, with varying polymer length in the tethered-diffusion model. (C) Selectivity as a function of K_D , with varying polymer length in the tethered-diffusion model.

Our model is related to the classic problem of molecular transport through an oil membrane separating two aqueous reservoirs [?]. The relative concentration of a species just inside the oil barrier to the concentration in water is called the partition coefficient. The steady-state flux through the membrane is directly proportional to the partition coefficient (Supporting Information, section ??, fig. ??). By analogy, one might expect the TF-FG binding affinity to determine the flux across the pore. However, binding is different from partitioning. In systems where the increase in intra-pore concentration arises from binding, the effective diffusion coefficient is typically inversely proportional to the partition coefficient, making the flux independent of binding affinity [22]. This result led us to consider whether TFs may be mobile while bound to FG Nups.

2.1.2 Bound-state diffusion allows selective transport

When bound TFs are mobile, selective transport occurs with a selectivity up to 240 for a conservative set of parameters (figs. 2.2B,C, ??, Supporting Information, section ??). Remarkably, this selectivity is comparable to experimental measurements of NTF2 versus GFP flux (Table 2.1). The interplay between binding kinetics and diffusion leads to an optimal dissociation constant $\sim 1 \mu\text{M}$ for maximum selectivity Figure 2.2C. Selectivity decreases for high K_D because binding is too

weak to significantly increase TF concentration in the pore. For low K_D , tight binding causes the concentration of bound complexes to become approximately constant across the pore. Because diffusive flux is driven by a concentration gradient, this washing out of the gradient by tight binding decreases flux and selectivity.

Our model predicts that selectivity is increased by increasing binding on-rate constant k_{on} Figure ???. Consistent with this, the on-rate constants of TF-FG Nup interactions have been measured to be diffusion limited [20, 31]. Large k_{on} makes transport more selective because fast binding kinetics relative to diffusive motion are necessary to maintain steep concentration gradients within the pore. High FG Nup concentration (as measured experimentally) leads to large N_t and low D_F , both of which increase selectivity. Decreasing D_F or increasing the length of the pore both reduce the magnitude of the flux and increase selectivity (figs. ??, ??). Therefore, varying TF free diffusion coefficient and pore length involves a trade-off between transit time and selectivity.

2.2 Mechanisms of bound transport factor mobility

Our result that bound-state diffusion is required for selective transport raises a mechanistic question: how can TFs move while bound to FG Nups? Here we consider two experimentally based mechanisms: movement of the bound TF due to the intrinsic flexibility of the FG Nups [?] and

Table 2.1: Comparison between experimental results for NTF2 and GFP (a similarly-sized non-binding protein) and model predictions. Flux measured in units of molecules per pore per second.

Method	Cell type	Species	Flux	Selectivity	Notes
OSTR	<i>Xenopus</i>	NTF2	91–123	24–37	[7]
		GFP	3.3–3.8		
OSTR	<i>Xenopus</i>	NTF2	47.3	43	[8]
		GFP	1.1		
Permeabilized cells	HeLa	NTF2	250	125	[6]
		GFP	2		
Model	–	Binding	2–480	1–240	This work
		Non-binding	2		

multivalent binding that allows hopping of TFs between neighboring Nups [32].

2.2.1 FG Nup flexibility allows tethered diffusion

Previous measurements have found that FG Nups are flexible and dynamic [20, 33, 34]. One end of an FG Nup is attached to the inner ring of the NPC scaffold. However, the Nup's flexibility means that a TF which binds far from the scaffold-attachment point is mobile. Tethered diffusion therefore provides a mechanism of bound-state diffusion and selectivity.

2.2.1.1 Bound-state diffusion depends on polymer and kinetic properties.

Flexible polymers behave as entropic springs [35] if they are not highly stretched. Therefore, a bound TF diffuses while attached to a spring-like tether, which can be represented as diffusion in a harmonic potential well Figure 2.3A. The width of the harmonic well is related to the length of the flexible domain. The effective length is the full FG Nup length if the FG Nups are not crosslinked, while the effective length is reduced if they are crosslinked or entangled [6].

In order to calculate the bound diffusion coefficient of the TFs, an averaging procedure is followed. First, the diffusion is assumed to be Fickian, which is a reasonably good though not perfect assumption (see section on Fickian diffusion). In the Fickian diffusion case, the diffusion coefficient is proportional to a mean-squared displacement (MSD) divided by time. We calculate the mean binding lifetime τ and the MSD corresponding to this “typical” binding event and divide them.

To begin, note that the duration of a binding event follows the exponential distribution

$$\rho(t) = \exp(-t/\tau)/\tau, \quad (2.4)$$

where $\tau = 1/k_{\text{off}}$ is the mean binding lifetime.

Next, the positional probability density of a bound TF is

$$P(x,t) = e^{-\frac{x^2}{2\alpha(t)}} / \sqrt{2\pi\alpha(t)}, \quad (2.5)$$

$$\alpha(t) = (1 - e^{-2kD_F\beta t})/(k\beta) \quad (2.6)$$

where k is the spring constant of FG Nup tethering and $1/\beta = k_B T$ is the thermal energy [?]. The center of the well is set at $x = 0$.

The mean-squared displacement (MSD) of the TF as a function of time is calculated, as any expected value, with the integral

$$\langle x^2(t) \rangle = \int_{-\infty}^{\infty} P(x, t) x^2 dx = \alpha(t). \quad (2.7)$$

Finally, the typical TF MSD during a binding event can be determined by evaluating

$$\overline{\langle x^2 \rangle} = \int_0^{\infty} \rho(t') \langle x^2(t') \rangle dt' = \frac{2D_F L_c \ell_p}{L_c \ell_p k_{\text{off}} + 3D_F}. \quad (2.8)$$

Here we assume that the spring constant is that of a worm-like chain polymer $k = 3/(2\beta L_c \ell_p)$, where L_c is the contour length and ℓ_p the persistence length [35].

Combining these results, the one-dimensional bound diffusion coefficient is

$$D_B \approx \frac{\overline{\langle x^2 \rangle}}{2\tau} = \frac{D_F L_c \ell_p k_{\text{off}}}{L_c \ell_p k_{\text{off}} + 3D_F} = \frac{D_F}{1 + 3\frac{D_F}{D_P}}. \quad (2.9)$$

Here $D_P = L_c \ell_p k_{\text{off}}$ controls the bound-state diffusion coefficient: higher D_P corresponds to a lower constraint of the TF by the tether and greater bound mobility. Bound mobility increases with increasing chain length and persistence length, or decreasing binding lifetime. When D_P is large ($D_F/D_P \ll 1$), D_B approaches D_F , since the long chains barely affect TF motion during the short binding event. For small D_P ($D_F/D_P \gg 1$), TF motion is inhibited by a short tether, giving $D_B \approx D_P/3 \ll D_F$. This result highlights that the kinetics of TF-FG Nup interaction are a primary determinant of the bound mobility: the faster the binding kinetics, the higher the bound diffusion constant.

Flexible disordered proteins typically have low persistence lengths [36], so we estimate $\ell_p \approx 1$ nm. If the on-rate constant is diffusion limited, $k_{\text{on}} = 10^{-3} \mu\text{M}^{-1} \mu\text{s}^{-1}$ [20,31], the binding affinity determines the off rate. Disordered FG Nups have $L_c \approx 100\text{--}280$ nm (250–700 amino acids long [?] with a contour length per amino acid ≈ 0.4 nm). For our conservative parameters, tethered diffusion alone predicts selectivity $S \approx 200$, a large flux enhancement for TFs over nonbinding proteins.

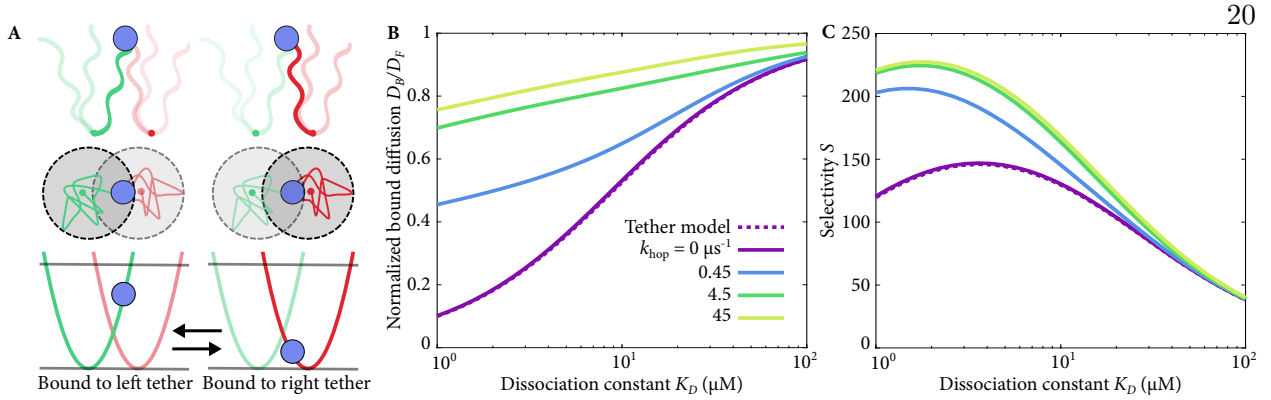


Figure 2.4: (A) Schematic of the inter-chain hopping model of bound-state diffusion. FG Nups are treated as entropic springs that constrain the motion of TFs, and inter-chain hopping allows a TF to move from one FG Nup (top and center left, green Nup) to another (top and center right, red Nup) without unbinding, which corresponds to switching from one harmonic potential well to another (lower). (B) Ratio of bound to free diffusion coefficient as a function of dissociation constant, with varying hopping rate in the inter-chain hopping model. (C) Selectivity as a function of K_D with varying hopping rate. FG Nup contour length $L_c = 40 \text{ nm}$ in (B, C).

2.2.2 Inter-chain hopping increases selectivity

The tethered diffusion mechanism is constrained by a trade-off: tighter binding increases the TF concentration in the pore, but hinders motion. Multivalent TF-FG interactions can relax this constraint, because a TF can bind simultaneously to more than one FG Nup, moving hand-over-hand while remaining bound [37]. Consistent with this, TFs may slide between nearby FG sites rather than fully unbinding and re-binding [32]. If the newly-bound FG repeat is on a neighboring chain, the FG tether site that constrains TF motion moves while the TF remains bound. We model inter-chain hopping with a TF that undergoes tethered diffusion when bound to an FG Nup and hops between neighboring, randomly distributed tethers Figure 2.4. Numerical simulations of this model determined the bound diffusion coefficient (fig. 2.5, Supporting Information, section ??). We note that intra-chain hopping does not change the flux, since the anchor point of the tethering chain is not changed; therefore we neglect it.

2.2.3 Detailed explanation of hopping simulation

In our simulation of TF motion with hopping between FG Nups while bound, we represented each FG Nup as an entropic spring (i.e. as a harmonic potential well). Well positions were randomly chosen from a uniform distribution, with the exception that we always placed one well at the starting position of the TF. The particle (the TF) started the simulation bound to this FG Nup, and remained bound throughout the simulation. While bound to one FG Nup, the TF diffused within the harmonic well representing that FG Nup. We recorded the position and mean-squared displacement of the TF from its starting location, which we then used to determine a bound diffusion coefficient, as described in more detail below. The TF could hop between tethers by changing which well it moved in.

2.2.3.1 Diffusion in a potential well

The TF moved in the harmonic potential of the FG Nup according to Brownian dynamics. At each timestep, the TF position was updated using a force-dependent diffusive step [38].

$$x(t + \delta t) = x(t) + \frac{F}{\Gamma} \delta t + \delta x, \quad (2.10)$$

where F is the force acting on the particle, Γ is the drag coefficient, δt is the timestep, and δx is a random Brownian step drawn from a Gaussian distribution with variance $\sigma^2 = 2D\delta t$. The drag coefficient of a spherical particle at low Reynolds number is given by Stokes' Law as $\Gamma = 6\pi\eta r$, where η is the fluid's viscosity and r is the sphere's radius. This result can be combined with the Einstein relation $D = k_B T / (6\pi\eta r)$ to give

$$\Gamma = \frac{k_B T}{D}. \quad (2.11)$$

The force $F = -k\Delta x$, where k is the spring constant of the FG Nup and Δx is the displacement of the particle from the Nup attachment point. We model the FG Nup as a worm-like-chain at small extension, so that $k = 3k_B T / (2\ell_p L_c)$, where ℓ_p is the tether persistence length and L_c is

the contour length. Then

$$x(t + \delta t) = x(t) - \frac{3D\Delta x\delta t}{2\ell_p L_c} + \delta x = x(t) - DK\Delta x\delta t + \delta x, \quad (2.12)$$

where K is the normalized spring constant $K = k/k_B T = 3/(2\ell_p L_c)$.

2.2.3.2 Hopping probability

We designed the hopping probability P_{hop} in order to satisfy the principle of detailed balance. During every iteration of the simulation, we picked an FG Nup at random from a list of the M Nups near enough to have a reasonable probability of hopping. TF hopping to the new FG Nup was attempted with success probability

$$P_{\text{hop}} = r_{\text{hop}} M \delta t e^{-\Delta G/2}. \quad (2.13)$$

Here the base hopping rate r_{hop} is a dimensionless input parameter, and the change in free energy (in units of $k_B T$) between the current Nup and the proposed new Nup is

$$\Delta G = \frac{1}{2} K(x - x_{\text{new}})^2 - \frac{1}{2} K(x - x_{\text{cur}})^2, \quad (2.14)$$

where K is the normalized spring constant, x is the particle's current position, x_{cur} is the anchor location of the Nup to which the particle is currently bound, and x_{new} is the anchor location of the proposed new Nup. Note that when a hop succeeds, the energy landscape changes to that of the new Nup, but the TF's position does not change during the hop. There is no upper bound on P_{hop} , but we adjusted the timestep to ensure that P_{hop} was greater than unity no more than 0.5% of the time that a hop was attempted.

2.2.3.3 Mean-squared displacement and diffusion coefficient calculation

We ran each simulation for 10^7 time steps with $\delta t = 0.01 \mu\text{s}$, and recorded the particle's position every 100 time steps. We calculated the mean-squared displacement $\langle x^2 \rangle$ (MSD) of the TF and averaged it over 100 runs Figure 2.5A. We then computed

$$\rho_{\text{MSD}}(t) = \langle x^2(t) \rangle \rho(k_{\text{off}}, t) = k_{\text{off}} \langle x^2(t) \rangle e^{-k_{\text{off}} t}, \quad (2.15)$$

as shown in fig. 2.5B, and numerically integrated the distribution in time. We determined the bound diffusion coefficient from the typical MSD-per-binding-event $\overline{\langle x^2 \rangle}$ using

$$D_B = \frac{k_{\text{off}} \overline{\langle x^2 \rangle}}{2}. \quad (2.16)$$

Here, the factor of 1/2 is appropriate because we consider a one-dimensional random walk.

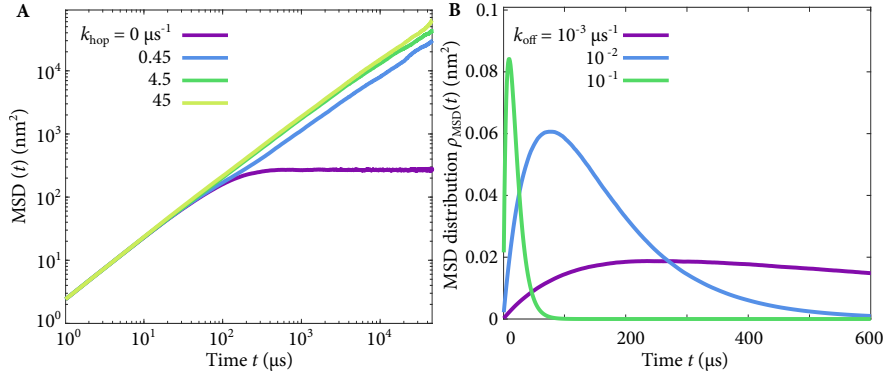


Figure 2.5: (A) Examples of mean-squared displacement (MSD) of a simulated TF in the inter-chain hopping model, with varying hopping rate. (B) Examples of MSD distributions $\rho_{\text{MSD}}(t)$ used in estimating the diffusion coefficient, with varying unbinding rate. Tethers have 40 nm contour length; other parameters are as discussed in the text.

2.2.4 Hopping simulation results

Inter-chain hopping increases selectivity most for tight binding and short chains, the parameter regime where tethered diffusion gives limited selectivity (figs. 2.4, 2.6, 2.7). Hopping may therefore be important for FGs that form transient crosslinks: if FG Nups are highly crosslinked, our model suggests that inter-chain hopping is the key mechanism of TF movement. For weaker binding and longer chains, inter-chain hopping leads to a modest increase in selectivity.

2.2.5 Fickian diffusion

Talk about how diffusion is almost but not quite Fickian, and show the anomalous diffusion plots (made with Mike's script) for various parameters. Talk about timescales and how this might affect the results.

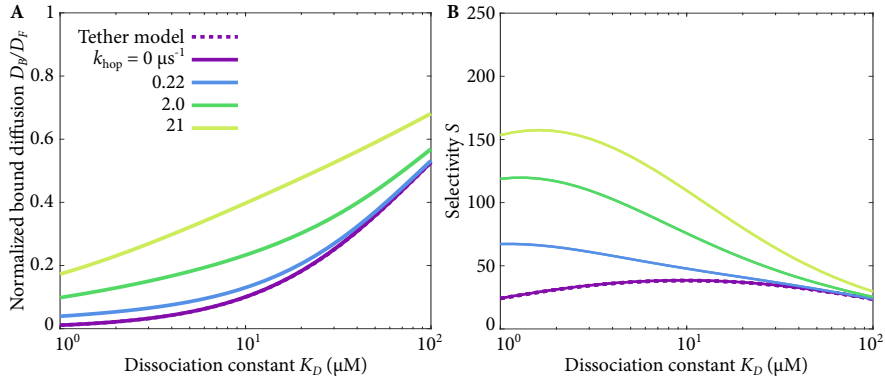


Figure 2.6: Bound diffusion and selectivity as a function of dissociation constant, with varying hopping rate for FG Nups with $L_c = 4$ nm.

2.3 Discussion

A key puzzle of the NPC is how transport-factor binding allows rapid transport through the pore. Binding typically immobilizes the bound particle, and so the increase in concentration resulting from binding does not, in general, result in increased flux. The biophysical theory we developed includes diffusion of TFs due to thermal fluctuations, binding to polymeric tethers, and the hopping of bound species between these tethers. Thus we identified principles of selective transport resulting from binding Figure 2.1, emphasizing that bound-state mobility is essential for selective transport Figure 2.2. Binding increases the local concentration, and any bound mobility increases the flux. We characterized two mechanisms to obtain bound-state mobility and found that thermally-driven diffusion of TFs bound to flexible tethers and rapid binding kinetics [20,31] allow TF mobility, leading to selectivity similar to that observed experimentally Figure 2.3. In addition, tether flexibility enables multivalent bound particles to hop between binding regions Figure 2.4 [18,19], further enhancing selectivity. Mobility of bound or partitioned molecules occurs in many biological contexts, suggesting that the mechanisms we study here may be broadly applicable [?,39].

Our model for selective transport by tethered diffusion generalizes to a range of FG-FG interactions [15], if we decrease the effective chain length L_c for cohesive FG Nups. For short chains the selectivity simply due to chain flexibility is modest, suggesting that other mechanisms, like hopping, may be important. Our model suggests that transient cross-linking of FG repeats

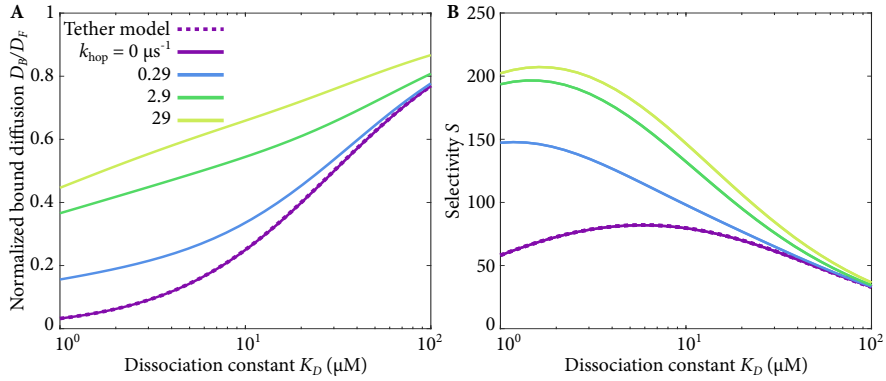


Figure 2.7: Bound diffusion and selectivity as a function of dissociation constant, with varying hopping rate for FG Nups with $L_c = 12$ nm.

proposed to occur within the pore may serve to increase the viscosity and therefore the selectivity.

Crosslinks need not be actively melted by TFs to enhance selectivity Figure ??.

Our model provides a quantitative tool to evaluate selective transport. Materials formed *in vitro* by spontaneous self-assembly of FG Nups [14] or transient crosslinking by alpha-helical peptides [40] show strong selective *entry*. Using published data, we predicted whether these gels also showed selective *transport* (table ??). Most synthetic gels are predicted to have $S < 10$, less than the selectivity of NTF2 in cells (table 2.1). The predicted selectivity of one hydrogel is $S \approx 200$, apparently the most selective synthetic gel to date [14].

2.3.1 Overcoming the limitations of binding

Binding, even in the presence of bound-state motion, limits selectivity. Biological systems appear to have developed strategies to avoid this, for example, by using true partitioning. Lipid domains in complex membranes partition proteins [?]. Membraneless organelles spontaneously assembled from low-complexity proteins and nucleic acids can localize a molecule without immobilizing it [?]. Because membraneless organelles are fluid, the constraints imposed in our NPC model by binding are released. Our work thereby suggests a benefit of phase-separated droplets to cells: they provide significantly higher selectivity than can occur with immobilizing binding. This may be especially important for spatially complex assemblies [?].

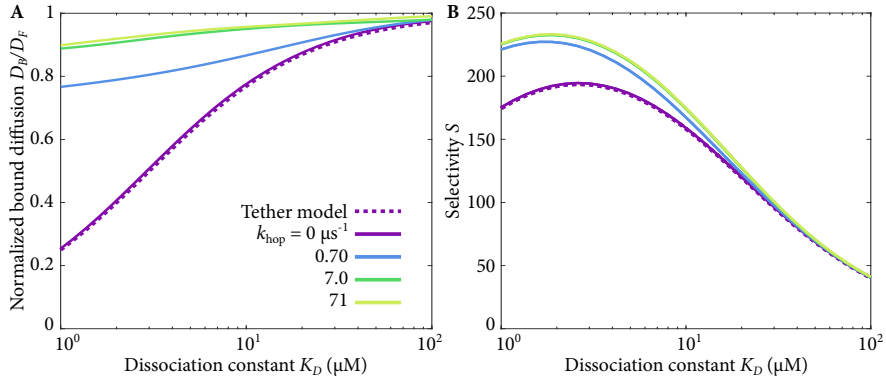


Figure 2.8: Bound diffusion and selectivity as a function of dissociation constant, with varying hopping rate for FG Nups with $L_c = 120$ nm.

Though we show it is not necessary, the active dissolution of polymeric biomaterials has been proposed to occur in the NPC [6]. This strategy is used by *Helicobacter pylori* to penetrate the gastric mucus [?]. Because the particularly dense extracellular matrix of solid tumors blocks the motion of particles, especially larger nanoparticles, ECM dissolution has been used to enhance drug delivery [?]. Unfortunately, this approach may not be universally applicable: breaking down the ECM surrounding tumors may promote cancer metastasis [?].

2.3.2 Design principles of selective transport by binding

Filtering by polymeric biomaterials occurs in many systems for particles of different sizes: for example, nutrients reach our intestinal walls while larger molecules are excluded. However, controlling the selective transport of similarly-sized molecules by tuning specific interactions has proven elusive. In drug delivery applications, inert nanoparticles are typically more effective at penetrating extracellular spaces and reaching their cellular targets [23]. Because biopolymer filters are the first point of contact of nanoparticles used for drug delivery, specific targeting of transport through mucus may enhance the effectiveness of drug delivery. If NPC-like bound mobility as described in our model could be achieved in these systems, it would increase the rates of transport and drug delivery.

Chapter 3

Hydrogel design for protein separation

In order to test the predictions of our bound-state diffusion model of selectivity, we needed to develop a biomaterial that could support bound diffusion and be used to test selectivity. There are several biological examples which show selectivity that could be explained by bound-state diffusion, including nucleocytoplasmic transport, liquid-liquid phase separated droplets, diffusion of DNA-damage-repair proteins in the nucleus, and passage through mucus. We decided to focus on making a material that mimics the nuclear pore.

One of the attractions of the bound-state diffusion model is that it does not rely on the geometry of the selective material. As long as the dimensions of the material are significantly larger than the protein diffusing through it, there is no practical difference between a nanoscale cylindrical pore and a macroscale bulk material. For ease of fabrication and testing, as well as in the hopes that it would scale up well, we opted to design a bulk material for protein separation.

A hydrogel substrate was chosen as the basis of the nuclear pore mimic and protein fragments taken from FG Nups anchored into it. Hydrogels are versatile materials, many of which are biocompatible, whose properties can often be easily tuned. We used a hydrogel substrate to provide an inert scaffold to which fragments of FG Nups were conjugated. These Nups were conjugated to the hydrogel at one end and free at the other, mimicking the arrangement found in the nuclear pore and providing a mechanism of tethered bound diffusion. The properties of these Nups, such as their length, number of transport factor binding motifs, and propensity towards aggregation, can be easily varied in order to test how these properties impact bound-state diffusion and thus

protein selectivity.

This hydrogel model is therefore the simplest way we could think of to make a material to explore the effects of bound diffusion on protein separation. It's inspired by the nuclear pore but does not attempt to reproduce its mechanism of selectivity exactly. Instead, we hoped to show that bound-state diffusion was measurable and controllable in a biomaterial, paving the way for molecular filters that might make use of this principle.

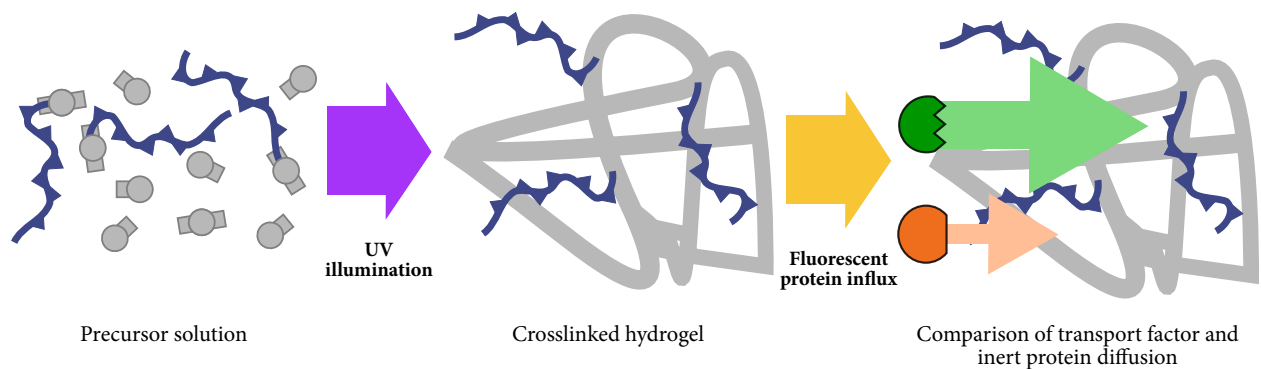
Over the course of making these materials, we ran into several significant roadblocks. Although hydrogels with a wide range of properties have been well-studied, gels suitable for protein separation are harder to come by. They require an intermediate pore size, large enough that the diffusion of a protein is not significantly hindered by the presence of the hydrogel meshwork, but small enough that the Nup peptides can easily reach the protein as it diffuses. This average pore size of 5-20 nm is difficult to find, though much smaller and much larger pores are easy to make. The swelling of the gels is also a problem, since we need them to be confined so that they pose an actual barrier to the proteins we are trying to separate. The creation of a hydrogel for selective protein separation poses many stringent requirements, often in competition with each other. This chapter describes the setbacks we faced and the progress we have made towards creating a hydrogel-based biomaterial suitable for selective separation of proteins.

3.1 Hydrogel fabrication

A wide range of hydrogels systems have been well-studied. Many are not suitable for the addition of proteins, but both PEG and acrylamide hydrogels, among others, can be crosslinked in an aqueous solution that does not harm proteins. We used both PEG and acrylamide hydrogels in our diffusion experiments. Thanks to Stephanie Bryant, Sadhana Sharma, Christopher Bowman, Danielle Konetski, and Benjamin Fairbanks for their help as we learned to make these hydrogels.

Whether using PEG or acrylamide, the basic hydrogel fabrication procedure was the same (Fig. 3.1). First, a precursor solution was mixed, which contained the hydrogel monomer, a crosslinker, a radical generator, and the Nup fragment, labeled with a reactive group at one end

Figure 3.1: Overview of hydrogel fabrication and fluorescent protein influx. A precursor solution is mixed, containing hydrogel monomers, crosslinkers, a photoinitiator, and the Nup fragment. Upon exposure to UV light, the precursor solution crosslinks, and one end of each Nup is conjugated to the hydrogel. The diffusion of a fluorescently-tagged transport factor can then be compared to that of a similarly-sized inert fluorescent protein.



that would conjugate it to the hydrogel. The radical generator was almost always a photoinitiator, which caused the precursor solution to crosslink when exposed to UV illumination. In a few cases, a chemical initiator was used, in which case the precursor solution crosslinked 10-30 minutes after mixing. By the end of the crosslinking process, the hydrogel contained Nup fragments tethered to the gel at one end, mimicking the arrangement of Nups in the nuclear pore and providing a mechanism of tethered bound diffusion for transport factors but not for non-binding inert proteins. The diffusion of both types of protein within the hydrogel could then be quantified using fluorescence microscopy.

There were four major components to the precursor solution: monomers, crosslinkers, initiators, and Nup fragments. To an extent, these components can be chosen independently of each other. Bisacrylamide or PEG-diacrylate crosslinkers must be used with acrylamide monomers, and PEG-dithiol crosslinkers with PEG-norbornene monomers, but the initiators and Nup fragments can be varied. There are many variations on crosslinker length as well, leading to a wide variety of possible hydrogels even using a relatively small set of components.

The PEG hydrogels made use of 20-kD 8-armed PEG-norbornene monomers (synthesized by the Bryant lab and Nathan Crossette) and either a 1-kD or 8-kD PEG-dithiol crosslinker (Sigma) (Fig. 3.2). To conjugate the Nup fragment to the PEG hydrogels, a cysteine was engineered at one end (lookup: which end?). Both the crosslinker and Nup fragment made use of Michael-thiol “click” chemistry [41] [42].

The acrylamide hydrogels used an acrylamide monomer and bisacrylamide crosslinker (Bio-Rad) (Fig. 3.2). An additional step was needed to prepare the Nup fragment for tethering to the hydrogel: either bisacrylamide or 700-Da PEG-diacrylate (lookup: Sigma) was conjugated to the terminal cysteine (see Sec. ??)

Regardless of the monomers and crosslinkers used, a radical generator is needed to initiate polymerization. We used either a photoinitiator, activated by UV light, or a chemical initiator system which began polymerization upon its addition to the precursor solution. Both systems have advantages: Photoinitiators are useful for patterned polymerization using photomasks and allow

Figure 3.2: Chemical structures of monomers and crosslinkers for PEG and acrylamide hydrogels. The total molecular weight of the 8-armed PEG-norbornene was 20 kD, and either a 1-kD or 8-kD PEG dithiol crosslinker was used. Structures from Sigma and CreativePEGWorks.

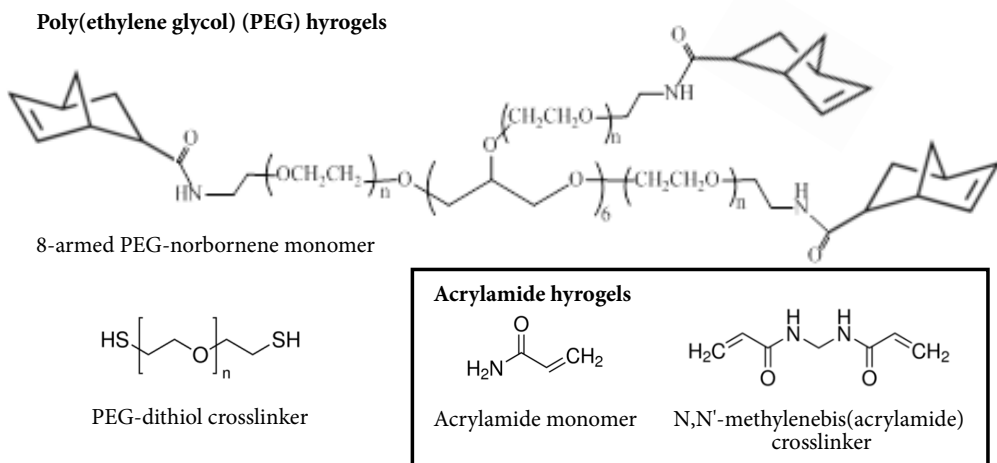
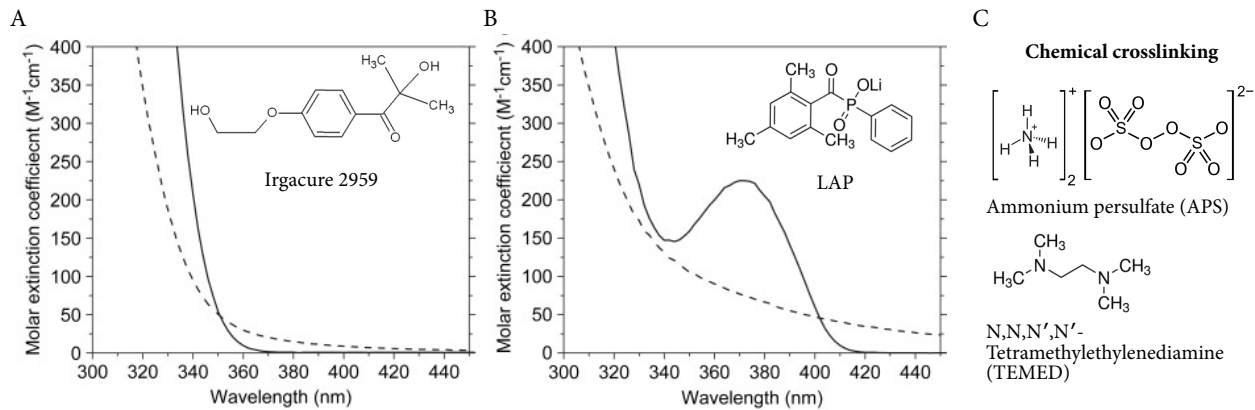


Figure 3.3: Absorption spectra of (A) Irgacure 2959 and (B) LAP (solid lines) and with that of their cleavage products (dotted lines) [43]. (C) Chemical structures of the APS/TEMED crosslinking system. Structures from Sigma.



the precursor to be mixed prior to polymerization, while chemical crosslinkers do not require careful protection from light. We nearly always used a photoinitiator.

Two photoinitiators were tested: 1-[4-(2-hydroxyethoxy)-phenyl]-2-hydroxy-2-methyl-1-propane-one (commercially known as Irgacure 2959) and lithium phenyl-2,4,6-trimethylbenzoylphosphinate (LAP). Figure 3.3 (A) and (B) shows the absorption spectra of each photoinitiator and that of its cleavage products [43]. LAP has an absorbance peak in the near-IR / violet range, is highly water-soluble, and is more effective at crosslinking, so it was used most of the time. However, due to its absorbance into the visible range, care must be taken to protect solutions containing LAP from ambient light wherever possible. Our LAP was synthesized by the Bryant lab, but it is now commercially available from Sigma as well.

An APS/TEMED chemical crosslinking system was occasionally used in place of the photoinitiator. Large numbers of hydrogels can be polymerized at once in this way, without the need for a large area of uniform UV illumination. Figure 3.3 (C) gives the chemical structure of ammonium persulfate (APS) and N,N,N,N-tetramethylethylenediamine (TEMED). APS is the radical generator, and TEMED accelerates the radical formation. The time to polymerize can be controlled by adjusting the concentration of both components (lookup: put this info in an appendix?).

It should be noted that the presence of oxygen inhibits all the initiators discussed above.

Precursor solutions were degassed for 10 minutes before use in a vacuum desiccator and polymerized no more than 10 minutes after degassing.

When a photoinitiator was used, the hydrogels were polymerized using UV illumination at either (lookup: LED wavelength) (lookup: Thorlabs LED model) or 405 nm (laser on A1R confocal microscope) inside flow chambers as described in Sec. 3.2. The typical intensity of the LED was (lookup) and the typical crosslinking time 30 s. Depending on the situation, photomasks were used to selectively expose regions of precursor to UV, or entire droplets of precursor solution were polymerized in an otherwise-empty chamber (Fig. 3.4). After crosslinking, hydrogels were rinsed with 10-100 times their volume with buffer and allowed to soak in fresh buffer solution overnight at 4°C in order to approach swelling equilibrium and remove any remaining precursor solution.

Following the buffer soak, typically a fluorescent solution of proteins was added to the gels. Usually this consisted of a transport factor (typically NTF2) and a similarly-sized inert protein (typically the red fluorescent protein mCherry). A typical experiment consisted of a video at 4x or 10x magnification of the hydrogel, reservoir chamber, and (if applicable) an outlet/inner reservoir which slowly accumulated protein as it passed through the gel. Experiments ranged from 1-24 hours, with 2 hours being the most common. Typical data produced was a plot of accumulation in the inner reservoir or hydrogel over the course of the experiment, as well as a concentration profile through the gel and inner reservoir. Experiments are described in greater detail in Chapter 4.

3.2 Flow chamber fabrication

The hydrogels were usually crosslinked in microfluidic flow chambers as shown in Fig. 3.5 (A). The thin chambers ensured that the top and bottom of the gel were sealed, so that transport factors and inert proteins could enter the gel only by diffusing into it. The small chamber size also reduced the quantity of transport factor and inert protein solution needed. Finally, the chambers were designed to be easily mounted on a microscope stage for recording experiments.

The basic flow chamber design consisted of an acrylic slide, patterned spacer or gasket, and coverslip, stacked and sealed together. Ports were almost always drilled in the plastic slide before

Figure 3.4: Procedure for photopolymerization with (A) or without (B) a photomask. (A) A flow chamber is filled with precursor solution. The photomask is placed to hide all areas that should not be crosslinked, and the chamber is exposed to UV illumination. Excess precursor solution is removed with a buffer rinse. (B) Microliter droplets of precursor solution are pipetted onto the slide surface before the chamber is assembled. After assembly, the chamber is exposed to UV illumination. The chamber is then filled with buffer.

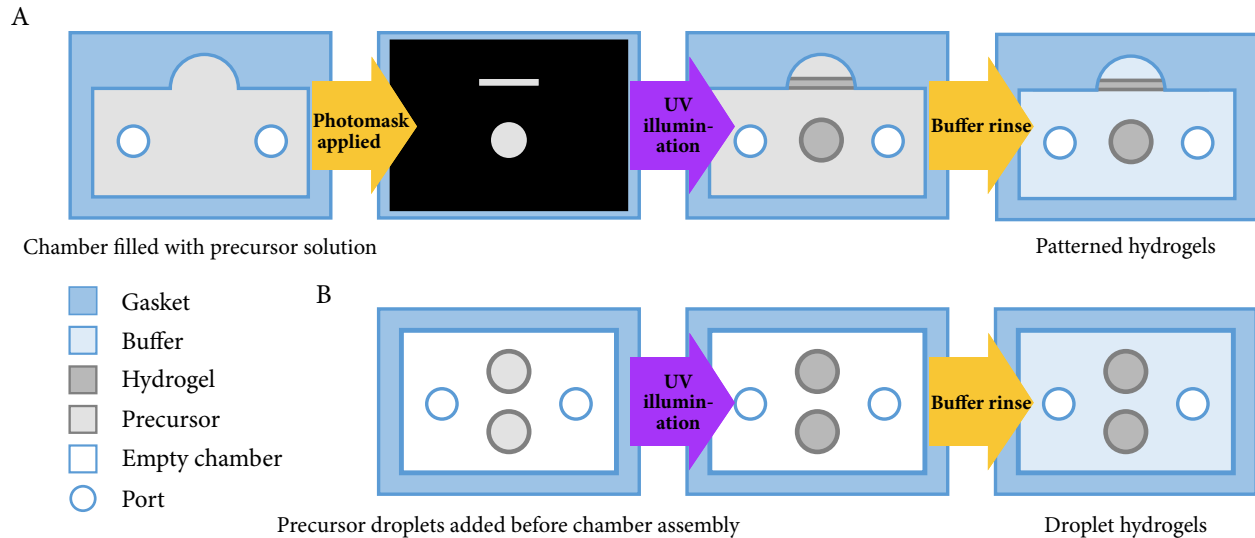
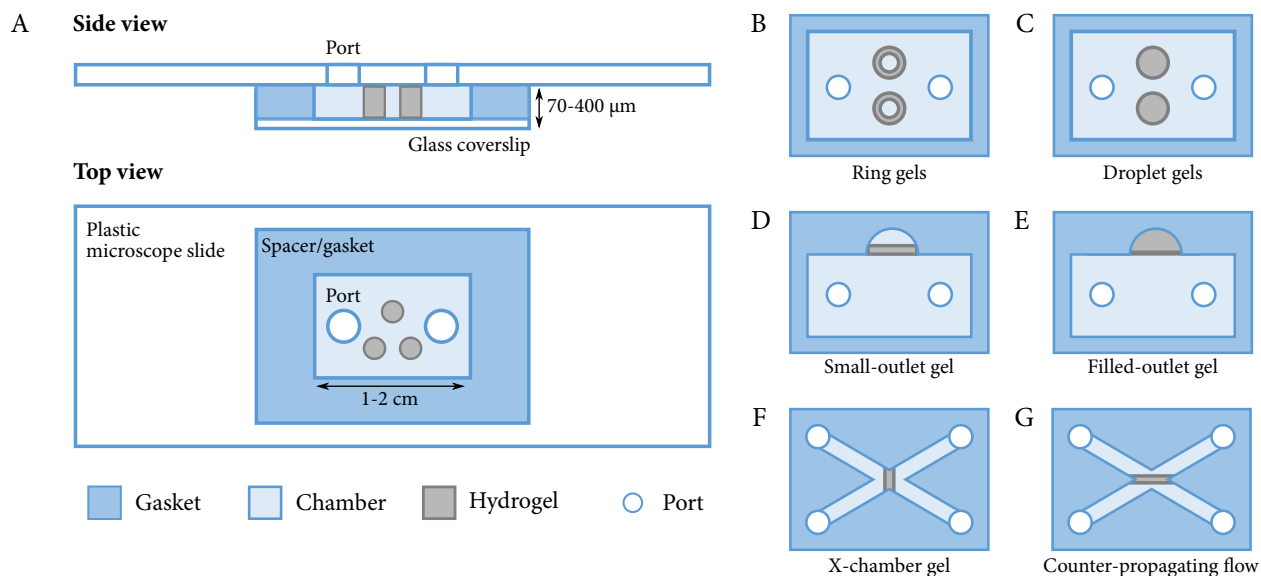


Figure 3.5: Flow chamber design and geometries. (A) Schematic of the most common flow chamber, showing slide, coverslip, gasket, ports, and hydrogels. (B)-(F) Common hydrogel geometries. Those in the left-hand column are suitable for selectivity measurements as well as diffusion measurements, while the right-hand column cannot be used to measure selectivity.



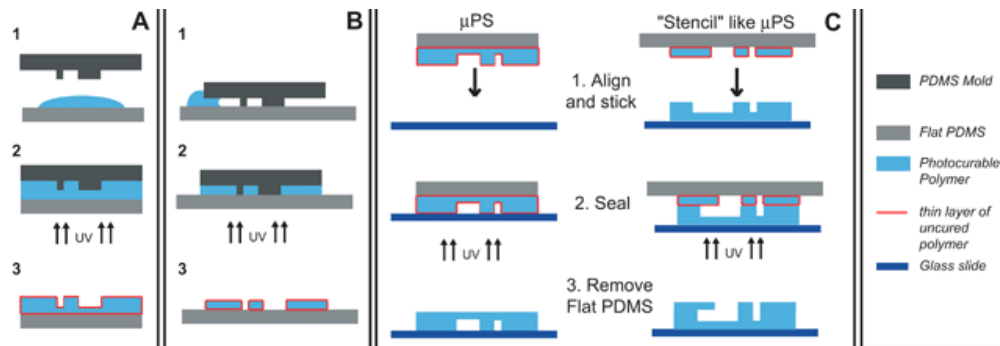
chamber assembly, in order to allow the chamber to be filled and emptied. Several methods of fabricating the gaskets and ports were tested in order to optimize the watertightness and longevity of the chambers as well as the ease of fabrication and re-use.

In particular, several materials were attempted for the gasket that determined the height and shape of the chamber. The simplest was double-stick tape, which could be used as a single width or cut into shape with a razor. The double-stick tape chambers were thin ($70\ \mu\text{m}$ per tape layer), of reliable thickness, and quick to make. However, they often leaked or dried over the course of several hours. Since many experiments take several days from preparation to finish, double-stick tape chambers were not usually sufficient.

Norland Optical Adhesive (NOA), a liquid adhesive which cures upon exposure to UV, was used in another style of flow chamber. Thin semi-cured NOA layers can be molded and used as “stickers” to build flow chambers [44, 45]. This procedure is outlined in Fig. 3.6 and relies on the inhibition of curing by oxygen. A droplet of NOA is sandwiched between a glass coverslip and a PDMS mold, which is permeable to oxygen. The NOA is briefly (approximately 3 seconds at lookup: intensity) cured, though a thin layer remains uncured due to the presence of oxygen at the adhesive’s surface. The PDMS mold is carefully peeled away, and the coverslip with NOA sticker is attached to the slide and sealed. The NOA is then fully cured and the chamber rinsed with ethanol to remove any uncured NOA remaining. Rather than applying NOA directly to the mold, as shown in Fig. 3.6 (A), it is also possible to seal the mold to the coverslip and wick NOA into the hollows (Fig. 3.6 (B)). This method is more error-prone and time-consuming but results in a flow chamber with glass on the top surface instead of NOA. Proteins are often less inclined to stick to the glass surface than to NOA.

PDMS molds for the NOA stickers were made cheaply with (lookup) 0.5-mm resolution using a Silhouette craft cutter (lookup brand exactly). After creating a template with the craft cutter’s software, the design was cut into a layer of packing tape that had been carefully applied to a large glass slide. The unwanted tape was peeled away using a razor and tweezers, leaving a depression where the chamber would eventually sit, and the slide used as the reverse-mold for a PDMS mold.

Figure 3.6: Microfluidic sticker fabrication from [44]. (A) A PDMS mold is used to shape an NOA droplet on a flat slide. The NOA is briefly cured but retains a sticky surface. (B) NOA can also be wicked into a PDMS mold. (C) The NOA sticker is placed onto a permanent surface, sealed, and cured entirely.



NOA-chambers are much more resistant to drying than double-stick-tape chambers, and can withstand the largest pressure and most rapid flow. On the other hand, they are significantly more difficult to make and cannot be re-used. For most experiments, where rapid flow is not necessary, PDMS gaskets were the most useful. Chambers made with PDMS gaskets are thicker (100-400 μm) than the other varieties and their thickness is not as reproducible, but they are easy to reuse, often can last several days without drying out, and are quick to assemble.

PDMS gaskets were made by preparing the volume of PDMS mixture needed to create a layer of a given thickness in a standard Petri dish. Once the PDMS had been thoroughly mixed, degassed, and spread evenly across the dish, it was cured for an hour at 70° and cut into shape with a razor. Measurement with a micrometer indicated that the nominally 400- μm -thick PDMS film had an error of no more than 10%. This thickness proved to be optimal for sealing to both the acrylic slide and glass coverslip, as well as easily re-usable after thorough cleaning with ethanol.

While plasma-bonding the PDMS to the glass was tested, it proved unreliable. As long as the chamber was not subjected to high pressures, an adequate seal formed without additional treatment if all materials were cleaned with ethanol and dried with house air before use. Likewise, silanation of the glass was attempted, in order to bond the hydrogel more securely to the top and bottom chamber surfaces, but it was not needed. The gels sealed well to the chamber as long as they were in contact with the surfaces while crosslinking. However, crosslinking the hydrogels on

PDMS and then transferring them to the chamber resulted in a poor seal. In consequence, almost all experiments were run using gels that had been crosslinked inside a chamber.

The ports were another point of concern for the watertightness of the chambers. If liquid needed to be flowed through a chamber at an appreciable speed, short lengths of PEEK tubing were superglued into the ports and fitted with Tygon tubing, which was then attached to a blunt-tipped syringe. For sufficiently gentle flows, however, ports were left simply as holes in the plastic slide and the chamber filled by pipette. After the chamber was filled, PEEK tubing ports were sealed with parafilm, and holes were sealed with a flat slab of clean PDMS.

Finally, portless thin chambers were used occasionally, such as for attempting fluorescence recovery after photobleaching (FRAP) using a confocal microscope. To make these chambers, microliter or smaller droplets of precursor solution containing 6- μm glass spacer beads were placed on glass slides and covered with a coverslip. The hydrogel was crosslinked and fluorescent protein solution wicked into the chamber. The chamber was sealed with valap (a 1:1:1 ratio of vaseline, lanolin, and paraffin which easily melts over a burner and re-solidifies rapidly). Such chambers last several hours on the microscope without drying but should not be used for longer experiments.

3.3 Hydrogel geometries

Our ultimate goal was testing protein separation by monitoring their passage into and through a selective material. In order to truly measure selectivity, the accumulation of proteins in an outlet reservoir beyond the test material must be measured, not just influx into the material. Many hydrogel and flow chamber geometries were tested in search of a setup that would allow selectivity, as well as free and bound diffusion, to be directly observed.

The limiting factors were the resolution of patterned hydrogel features, the size and accessibility of the outlets, and the equilibrium swelling of the hydrogels. Attempts to improve one of these factors typically led to worse outcomes for the others. Two major classes of hydrogel geometry emerged: those with an outlet reservoir, and those without. The hydrogels without an outlet reservoir cannot be used to directly measure the gels' selectivity, but diffusion constants for

the inert protein and transport factors can still be determined. Chapter 4 details the results of bound-state-diffusion experiments using no-outlet hydrogels.

The hydrogel geometries that contained an outlet reservoir are shown in Fig. 3.5 (B), (D), and (F). Ring-shaped gels (B) provide a small outlet reservoir, which is quick to equilibrate. They were fabricated using a confocal microscope (Sec. 3.7) or using PDMS molds 1-5 mm in diameter. While these rings would have been ideal for selectivity measurements, we were never able to work out a procedure that would result in artifact-free, well-sealed rings.

Fig. 3.5 (D) features a portless outlet reservoir which is much smaller than the inlet. As with the ring gels, these outlets are quick to equilibrate and their precise volume can be calculated, as the entire outlet is in the field of view of a 4x objective. A thin hydrogel bar was polymerized using a photomask, separating the inlet and outlet reservoirs. Without ports in the outlet, the chamber was soaked in buffer for 24 hours to remove the remaining precursor solution from the outlet. The inlet could then be filled with a fluorescent protein solution and accumulation in the outlet measured over time. Unfortunately, it's likely that the outlet itself was lightly crosslinked, no matter how carefully we used the photomask. See Sec. 3.7 for more evidence of stray crosslinking. Additionally, the hydrogel bars were of irreproducible thickness (50-200 μm) and swelled or buckled unpredictably. Ultimately, the lack of reproducibility between replicates made this geometry unusable.

Finally, Fig. 3.5 (F) shows an x-shaped chamber with four ports. A thin bar of hydrogel was polymerized at the junction of the arms using a photomask. The inlet and outlet reservoirs are approximately the same size, leading to slow equilibration in the outlet. The precise volume of the outlet is impossible to determine, as the arms are usually partly filled. Additionally, these chambers must be made using NOA stickers, which are difficult to use, and they tend to dry rapidly. The x-chamber geometry is therefore not useful except in specialized situations. A slightly more helpful version is the counter-propagating flow chamber shown in Fig. 3.5 (G). In this version, the hydrogel bar is as long as possible, creating a "hydrogel window" that separates the two arms of the chamber. While this setup was never used to test protein selectivity, in principle a counter-propagating flow can be established using syringe pumps in order to simulate constant concentration in infinite inlet

and outlet reservoirs while using a limited amount of material. A similar setup is demonstrated in [45].

The no-outlet hydrogel geometries shown in Fig 3.5 (C) and (E) are much simpler to make but do not allow for measurement of protein selectivity. Panel (E) shows a variation on the small-outlet chamber in which the outlet is filled with hydrogel and crosslinked using a photomask. Finally, the droplet gels in panel (C) were added to the chamber before assembly and crosslinked without a mask (Fig. 3.4 (B)). These are the only hydrogels which were made without a mask, which greatly reduced the irreproducible edge effects (also seen in Sec. 3.7). Droplet gels have volumes of 0.5-2 μL and equilibrate 30-kDa proteins in 24-48 hours. While these gels cannot be used to monitor selective transport through and exit from the gel, we can use them to measure the diffusion constants of proteins within the gel and the selective influx of transport factors. Chapter 4 focuses entirely on droplet hydrogels made in 400- μm -thick PDMS gasket chambers with two PEEK-less ports.

3.4 FSFG

3.5 Pore size

One of the biggest problems we faced was that of pore size. Although there is a range of pore sizes in any hydrogel, and it's not actually always obvious how to define it, we wanted an average pore size large enough that we could be confident that any differences in the behavior of transport factor and inert protein were due to their interactions with the Nups, not slight differences in size or interactions with the hydrogel. At the same time, we wanted the anchored Nups to fill a significant portion of the pore. This meant that we wanted a hydrogel with pores somewhere between 10 and 20 nm on average. It turns out that this is a difficult regime for hydrogels. It's easy to get pores significantly smaller using acrylamide or PEG systems, or significantly larger using systems like collagen, but the intermediate regime is difficult. We tried many methods of increasing the pore size of our PEG and acrylamide hydrogels, including changing the composition and crosslinker, as well as adding porogens. Finally, we settled on 6% acrylamide hydrogels as being reasonably good

for NTF2 and mCherry comparisons (both proteins are about 30 kD and we probably couldn't have used any larger ones in these gels). This remained a source of frustration throughout the experiments.

I tried to calculate average pore size using an equation which I will cite here. Most people use the swelling ratio or microrheology to determine pore size, which is difficult for us because the hydrogels are not very reproducible and they are also very small. I used a paper which does not rely on those measurements, but also is probably not very accurate. My estimate was that the average pore size in a 10% wt PEG hydrogel is about 5 nm, which is roughly the same size as NTF2 and mCherry. This means that we were likely seeing a lot of interactions/hindrance by the gel in the PEG gel experiments. We were unable to lower the PEG or crosslinker concentration significantly without going below the gel point and being unable to make gels.

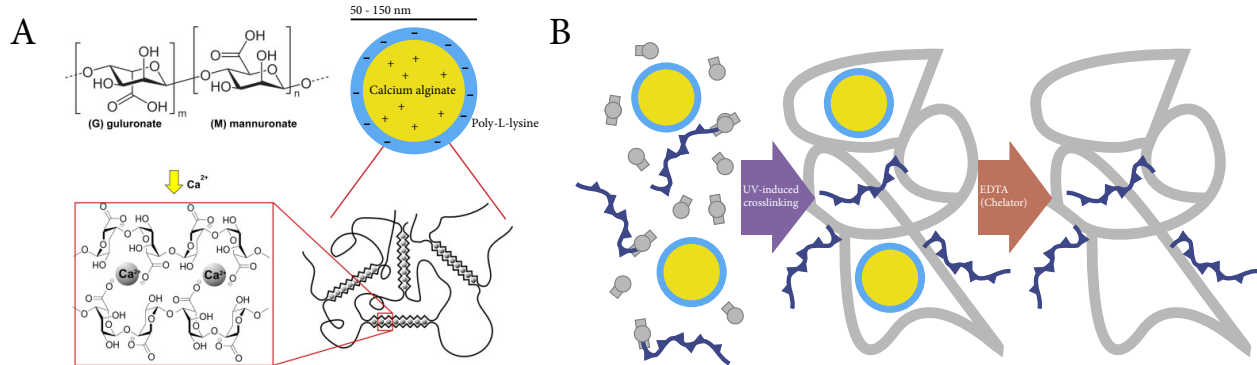
We did attempt to fix the problem with the PEG hydrogels by moving to a longer crosslinker. We switched from a 1 kD to an 8 kD PEG dithiol linker. The longer linker made the hydrogels swell more and be more porous at equilibrium, but it also made the gels softer and less mechanically stable. Overall, the decrease in stability outweighed the improved pore size. We also tried using non-PEG crosslinkers, including a coiled-coil protein (cite here) and DNA. We could never get the coiled-coil protein to express, and the DNA crosslinker didn't form a gel. We also tried putting a cysteine at each end of the Nup and using it as a crosslinker, but that didn't form a gel either.

Finally, we switched to acrylamide gels because the pore size was slightly better and the mechanical properties better. I think acrylamide has a more heterogeneous pore structure than PEG, which we decided was a good thing. Entry into the 6% acrylamide gels was consistent and similar for NTF2 and mCherry. I will put in a figure of some kind here.

3.6 Porogens

I tried to make gels with a larger pore size by using porogens. These are nanoscale particles that can be mixed into the gel precursor solution and then removed/dissolved after crosslinking. The idea is that then they would leave pores of a better size and also make it easier for the gel to swell

Figure 3.7: Alginate crosslinking from [46]. Alginate is composed of alternating guluronate (G) and mannuronate (M) blocks. Addition of calcium ions leads to an “egg-box” crosslinked structure. Add a cartoon of spheres in our gel (with positive poly-L-lysine coating around negative alginate gel) and the spaces they should leave upon depolymerization.



to equilibrium. I tried alginate nanospheres (which could then be removed by chelating the calcium ions) and large molecular-weight dextrans that could be removed by digesting with dextranase. Neither of these options worked out. I couldn’t get the nanospheres to reliably resuspend in the precursor solution. The dextran/dextranase system was more promising, but too much dextran remained in the hydrogels even after dextranase digestion. Also the dextranase chewed up the FSFG.

3.6.1 Alginate nanospheres

Alginate is a monomer that can be made to polymerize by adding calcium ions (or other divalent ions?). Include a picture of the alginate structure with and without calcium. It’s inert (and edible) and the polymerization can be reversed by adding EDTA or another chelating agent to remove the calcium. Alginate salts are available in a number of average molecular weights and viscosities.

A number of protocols exist for creating alginate microspheres, but fewer are appropriate for nanospheres, which is the scale that we would need in order to use them as a porogen. I did make spheres following the method described in [47].

I prepared 10 mL of 0.6 mg/mL alginic acid sodium salt (Sigma, low-viscosity, product

number A0628) in water. Even a small amount of sodium alginate added to water creates a viscous solution that takes a lot of time and stirring to dissolve. I used the Garcea lab sonicator with the microtip at 40% amplitude to sonicate the sodium alginate solution while adding 2 mL of 0.67 mg/mL calcium chloride in water drop-by-drop. I then stirred the solution on a magnetic stir plate for 30 minutes before adding 2 mL of 0.3 mg/mL poly-L-lysine in water. The solution was stirred 30 more minutes before finally being spun down (check spinning conditions in lab book).

I tested several methods of preparing the nanospheres for addition to the hydrogel precursor solution. First, the nanospheres were left in the solution in which they were made. Second, the nanospheres were spun down out of that solution at 14400g for 10 minutes and immediately resuspended in deionized water. (The pellet becomes more difficult to resuspend if it is not immediately resuspended.) Finally, the nanospheres were lyophilized and resuspended in water. The resuspended solution remained cloudy even after several days, and so I didn't pursue lyophilizing the nanospheres.

The radius and diffusion coefficients of the both the non-spun and spun nanospheres were determined using a Titan DynaPro dynamic light scattering (DLS) system. The non-spun nanospheres had an average radius of 170 ± 10 nm, with an estimated diffusion constant of $1.1 \pm 0.1 \mu\text{m}^2/\text{s}$. The nanospheres that had been spun and resuspended had two populations: almost entirely particles of radius 210 ± 10 nm and diffusion constant $1.05 \pm 0.06 \mu\text{m}^2/\text{s}$, and a small number of very large particles. The large particles are probably aggregates from centrifugation.

After measuring the size distribution of the two samples, I added EDTA in an effort to depolymerize the nanospheres. The maximum final EDTA concentration was 25 mM, and the samples were left to sit up to 30 minutes. Re-running the DLS data gave inconclusive results as to the presence or size of remaining particles. The fits did not change much, although the large aggregates appeared to have vanished from the spun sample. It appeared that at least some nanospheres remained.

Next, the nanospheres were added to hydrogel precursor solution, which was then crosslinked. Several nanosphere concentrations were tested before a condition was found in which the nanospheres

appeared by eye to resuspend. An approximately 2 μL nanosphere pellet (spun down from 10 mL of solution) was resuspended in a final concentration of 0.11 mg/mL PEG-ene, 0.09 mg/mL 8K PEG dithiol linker, and 5 mM LAP, all in 50 mM MOPS buffer pH 7.4. The MOPS buffer was chosen because it has no divalent cations (and thus will not interfere with the alginate nanospheres). The isoelectric point of poly-L-lysine is at about pH 5, and the nanospheres should be kept above that pH so their coating remains intact.

However, even these gels were clearly inhomogeneous under 4x magnification. In an attempt to depolymerize the nanospheres, the resulting hydrogels were rinsed with PTB pH 5 (to remove any possible poly-L-lysine coating) and then soaked in 100 mM EDTA for two days. No change was observed under 4x magnification. For comparison, a macroscopic alginate droplet dissolved after 20 minutes in 100 mM EDTA and vortexing. New gels were made and soaked in a pH 5 buffer (to remove any poly-L-lysine coating) and then in a solution containing 100 mM EDTA and 200 mM sodium citrate. Gels remained cloudy and no change was observed.

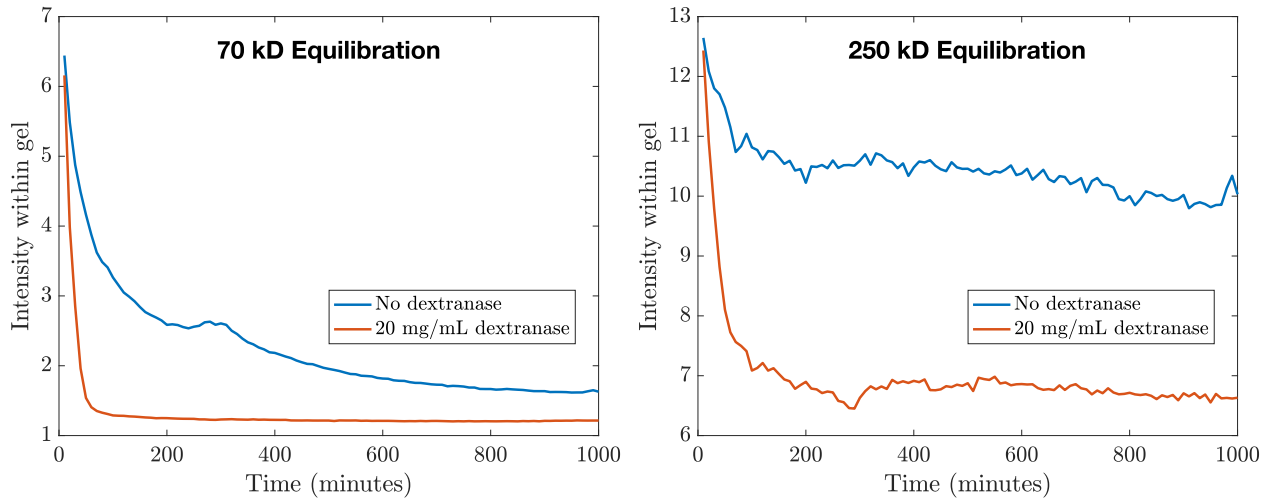
Given the difficulty in resuspending and depolymerizing the alginate nanospheres, our focus shifted to developing a dextran/dextranase porogen system.

3.6.2 Dextran/dextranase porogen system

Following the alginate nanospheres attempt, we tried creating nanopores using high-molecular-weight (high-MW) dextran. Dextran is a branched, inert polymer that is commercially available at molecular weights up to 250 kD. We used two sizes as porogens, 70 kD ($R_H \approx 10 \text{ nm}$) and 250 kD ($R_H \approx 15 \text{ nm}$) [48].

As a proof of concept, I made and crosslinked precursor solutions containing 100 μM 70 kD dextran-rhodamine or 250 kD dextran-fluorescein. The precursor contained 12% acrylamide and 3.3% bisacrylamide in 50 mM sodium acetate (NaOAc) buffer pH 5 as well as 2 mM LAP. The precursor solution was crosslinked as 1- μL hydrogels in a 400- μm tall PDMS gasket chamber for 20 s using the UV LED. After rinsing with NaOAc buffer, the chamber was filled with a freshly-made solution of 20 mg/mL dextranase (Sigma, D5884, dextranase from *Penicillium sp.*) in NaOAc

Figure 3.8: Exit of fluorescent dextran from hydrogels after digestion with dextranase.



buffer. Chamber was immediately placed in the Olympus widefield's environmental chamber, held at 37°C, and imaged overnight. The fluorescence intensity in the dextranase-treated gels decreased significantly more rapidly than that of gels which contained dextran but were not treated with dextranase (Fig. 3.8). In the case of 70 kD dextran, the fluorescence reached a steady value (equilibrated, same as that in the reservoir) in approximately 100 minutes, while the non-treated case wasn't equilibrated after an overnight incubation. For the 250 kD dextran, both the treated and non-treated gels reached an equilibrium in approximately the same amount of time, but the treated gel equilibrated much closer to the reservoir level than the non-treated gel. Both sets of gels indicate that dextranase is able to digest the dextran within the hydrogels, allowing a significant amount of dextran and digest products to leave the gel, as expected.

The next step in attempting this porogen system was recreating the effect in FSFG gels. Unfortunately, it became clear that the dextranase was digesting the FSFG as well as the dextran (Fig. 3.9). At this point, we stopped trying to use the dextran-dextranase porogen system for FSFG gels. However, we did investigate the effect of dextran-dextranase treatment on the pore size in acrylamide hydrogels without anchored proteins. Contrary to expectations, dextran-dextranase treatment did not increase subsequent diffusion of fluorescent proteins into the treated hydrogels.

Figure 3.9: Dextranase digestion of FSFG

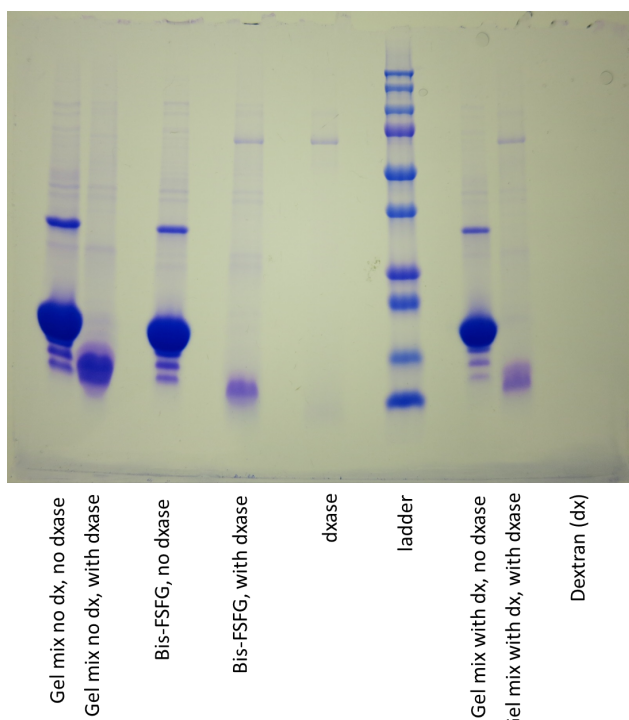
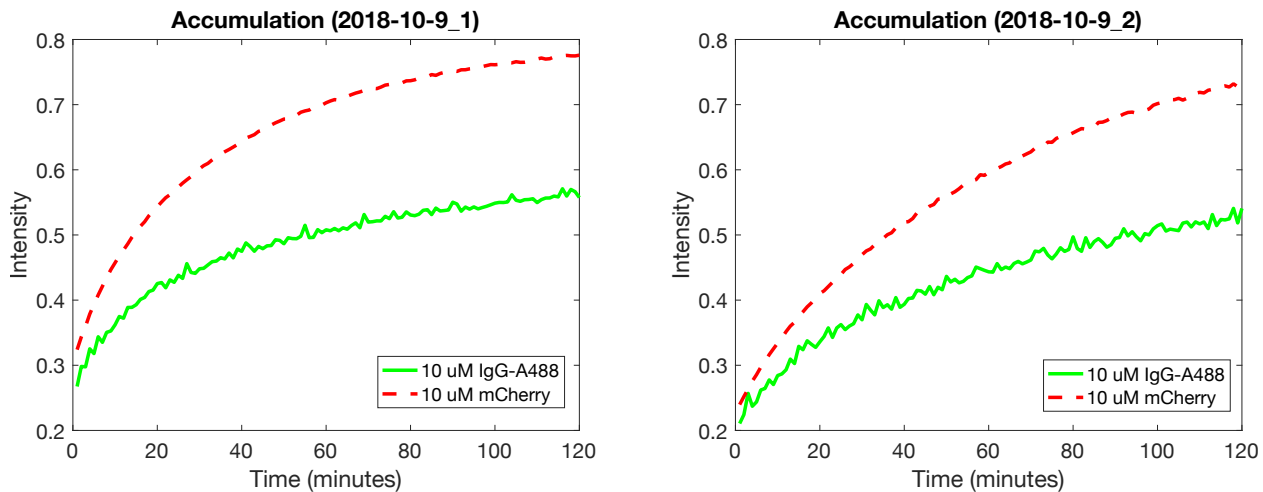
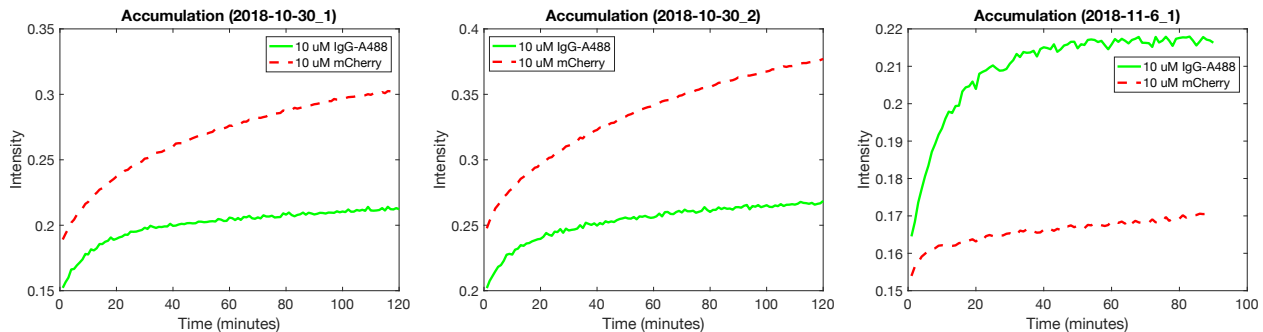


Figure 3.10: Accumulation of fluorescent proteins in gels treated with dextranase.



For these experiments, I used 200 kD non-fluorescent dextran in the acrylamide precursor solution. After the gels (either 12% or 6% final acrylamide concentration) were crosslinked, I treated them with 20 mg/mL dextranase solution in sodium acetate buffer (freshly made solution) for 2 hours at 37°C in an incubator. Then I rinsed the gels with buffer and let them sit in fresh buffer in the fridge overnight. (Check this - sometimes I used a syringe pump to flow 10 mL of PTB through overnight, instead of letting the chamber sit.) The next day, I challenged the gels with a solution containing 10 μ M each IgG-Alexa488 (150 kD) and mCherry (28 kD). I monitored the accumulation of each protein in the gel over time (Fig. 3.10). In both the 12% and 6% acrylamide gels, dextran-dextranase treatment did not improve influx of IgG-Alexa488 over corresponding non-treated gels. In 6% acrylamide gels, the influx of mCherry also remained approximately the same for treated and non-treated gels. This indicates that dextran-dextranase treatment does not significantly increase the pore size in acrylamide hydrogels. This is probably because significant dextran remains in the gel even after dextranase treatment, as suggested by Fig. 3.8. Unusually, the 12% acrylamide gels showed an odd effect with mCherry accumulation. In two separate instances, dextranase treatment appeared to suppress the entry of mCherry into both the dextran-containing hydrogel and the no-dextran control gel in the same chamber (Fig. fig:mCherry-suppression). IgG-

Figure 3.11: Suppression of mCherry in control gels that were in the presence of dextranase, dextran, and dextran digestion products (maltose).



Alexa488 accumulation remained the same as a non-treated gel. Tests of gels without dextran but treated with dextranase did not show this mCherry suppression. I didn't thoroughly investigate this effect. The only thing I can think of that's different between the gels that did and didn't show mCherry suppression is that the gels that suppressed mCherry were in the presence of both dextran and dextranase, and therefore also dextran digestion products (which are mostly maltose, I believe). Maybe the presence of maltose (despite the fact that it should have been thoroughly rinsed away) interfered with the accumulation of mCherry. It's odd. In conclusion, dextranase is capable of digesting a significant fraction of high-MW dextran within an acrylamide hydrogel. However, a significant amount of the dextran still remains in the gel even after an overnight rinse, meaning that dextran-dextranase treatment does not result in noticeably larger pores overall. In addition, the dextranase we used digested the FSFG peptide as well as dextran. Dextran-dextranase treatment is not suitable as a porogen system for our hydrogels.

3.7 Polymerization using confocal microscope

Given the problems that arose using photomasks and a UV LED to make hydrogels, we tested a crosslinking method using a 405 nm laser on the Nikon A1R spinning disc confocal microscope in the JSCBB microscopy facility. Once a region of interest has been defined with the Nikon software, the photobleaching setting can be used to selectively expose regions of the field of view to UV light.

The precursor solution therefore crosslinks in the region of interest only. This method is similar to that used in [45], but the masking is done using the A1R software instead of a physical mask in the back focal plane.

We were able to “draw” hydrogels of arbitrary shapes using the 10x objective on the confocal along with the 405 nm laser at 100% power. Figure 3.12 shows hollow rings with an outer diameter of about 600 μm and an inner diameter of 500 μm , as well as lines with a width of about 50 μm . In order to crosslink the precursor solution, two raster-scans of the laser across the region of interest were needed, with the longest-allowable dwell time per pixel. (In the microscope settings, the shortest dwell time is set as ‘1’ and the longest as ‘1/32’.) The precursor solution contained 0.5 mM LAP, 110 mg/mL 20kD 8-armed PEG-norbornene, 11 mg/mL 1kD PEG-dithiol, and 1 mM TCEP in PTB; it was used to fill 70- μm -thick sticky-tape or NOA flow chambers.

Crosslinking with the confocal has several advantages over LED crosslinking. Significantly smaller features are possible using the confocal. 50- μm features are consistent and reproducible, and features down to approximately 25 μm are possible, in contrast with the effective 100- μm lower limit using the LED and photomasks. Additionally, arbitrary shapes, including shapes with inner cavities, are possible using the confocal. Multiple small hydrogels can be created in the same chamber, including hydrogels of varying composition, created by removing the excess precursor solution and refilling the chamber with a different solution. Finally, the degree of crosslinking can potentially be varied by changing the photobleaching settings.

The most appealing geometry made possible with confocal crosslinking is the hydrogel ring, as shown in Figs. 3.12 and 3.14. Unlike all other hydrogel-chamber geometries, the inner reservoir is small enough to equilibrate in only a few hours (Fig. 3.13). Ideally, the hydrogel rings could have been used to test selective flux through the NPC mimics, a possibility not offered by other hydrogel-chamber geometries, which are optimized for testing influx into the hydrogels only. Long thin lines can also be written with the confocal by repeatedly moving the field of view and re-crosslinking, overlapping the new segment with the previous. This geometry could be useful in creating counter-propagating flow chambers with hydrogel windows.

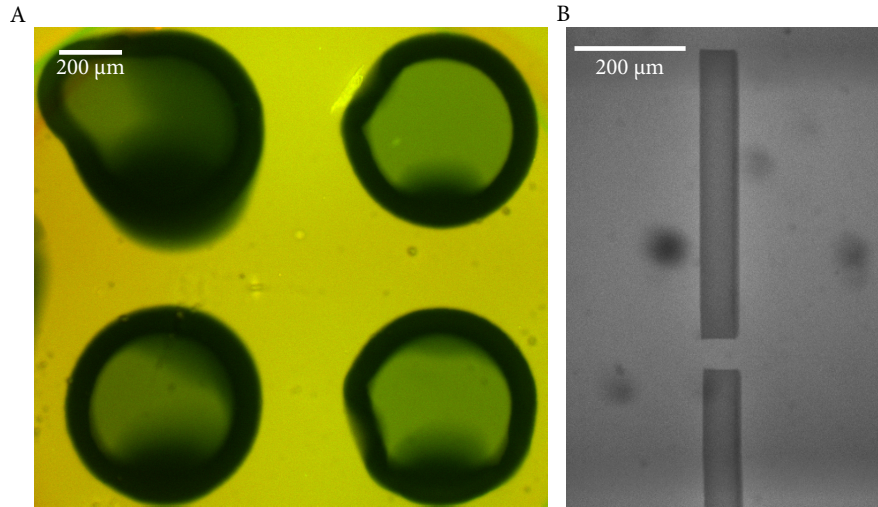


Figure 3.12: Image of laser-written hydrogels. (A) Ring hydrogels containing no Nups. Reservoir contains $20 \mu\text{M}$ NTF2-A488 and mCherry. (B) Line hydrogels containing FSFG-A647. Reservoir contains precursor solution with FSFG-A647. Photobleaching within gel by 405 nm laser is evident.

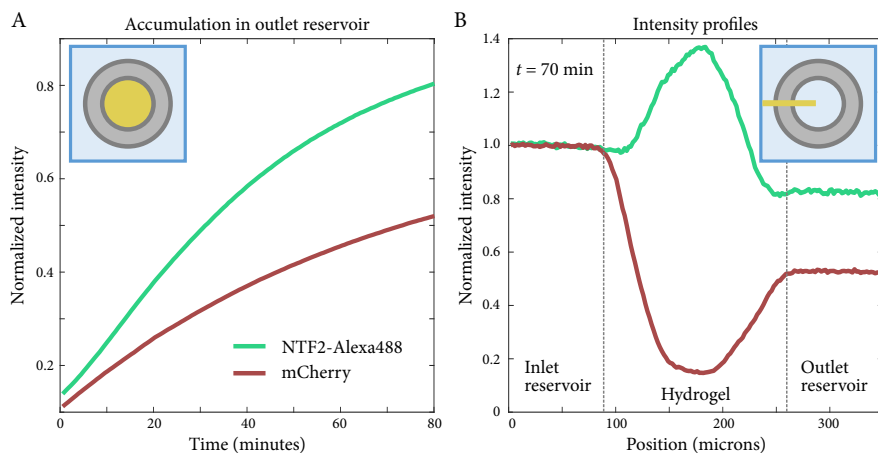
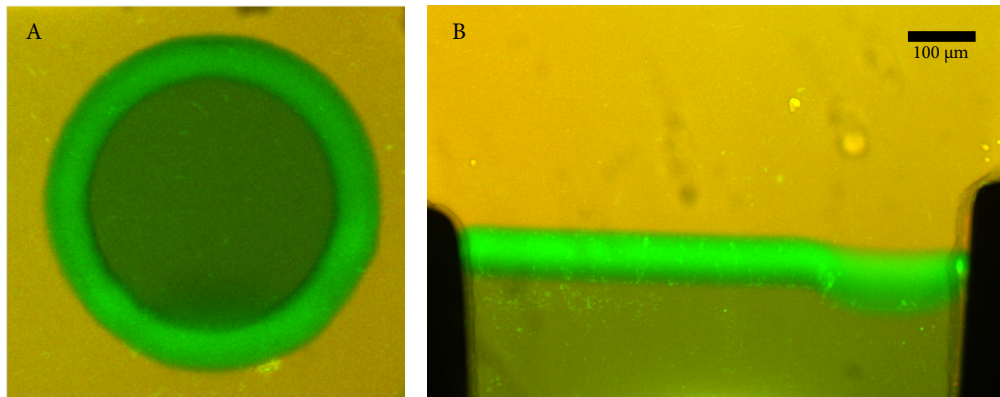


Figure 3.13: Sample (A) accumulation and (B) intensity profile plots for a $50 \mu\text{m}$ thick confocal-crosslinked ring nominally containing 10 mg/mL FSFG. Intensity normalized to inlet reservoir. Inlet contains $25 \mu\text{M}$ NTF2-Alexa488 and mCherry in PTB.

Figure 3.14: Images of laser-written hydrogels nominally containing 10 mg/mL FSFG. Reservoirs contain 20 μ M NTF2-A488 and mCherry. (A) Hydrogel ring, likely with lightly-crosslinked inner reservoir. (B) Hydrogel bar separating large inlet and small outlet.



Confocal crosslinking does not damage FSFG, as demonstrated in Fig. 3.14. Hydrogels were made using the precursor solution described above with the addition of 10 mg/mL FSFG-cys. After soaking in PTB buffer overnight, a mixture of 25 μ m each NTF2-Alexa488 and mCherry was added to the outer reservoir. After two hours of equilibration, the FSFG hydrogels showed a partition coefficient greater than one for NTF2-Alexa488 but smaller than one for mCherry. This indicates that FSFG is anchored into the gel and that NTF2-A488 is able to bind it.

Finally, Norland Optical Adhesive (NOA) can also be crosslinked using this method. Complicated flow chambers can be created, although it is labor-intensive and difficult to remove all of the excess NOA afterwards.

Despite the advantages of confocal crosslinking, several obstacles combined to ultimately make this method unusable for our purposes. The most serious problem was that of stray crosslinking. Areas outside of the defined region of interest were often unpredictably crosslinked, as can be seen in Fig. 3.12. Stray crosslinking outside of the rings is limited by rinsing the gels within 5 minutes of crosslinking, removing any excess precursor solution [45]. However, rinsing the chamber does not remove precursor solution from the ring's inner reservoir. Stray crosslinking in this reservoir is often more difficult to detect and more damaging to the experimental results. Figure 3.14 illustrates the problem: the ring has been equilibrated with NTF2-A488, which has preferentially

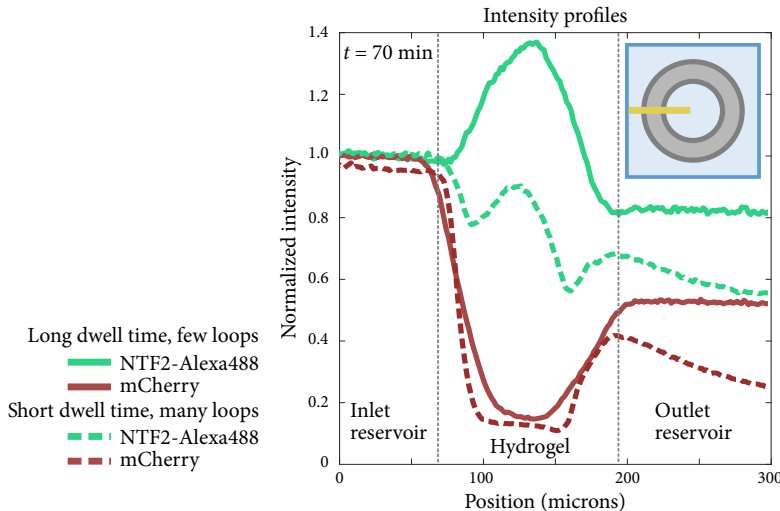


Figure 3.15: Effect of dwell time and loop number on edge-dip effect in equilibrated, confocal-crosslinked ring hydrogels. Nominal FSFG concentration is 10 mg/mL. Reservoirs contain 20 μM NTF2-A488 and mCherry in PTB. Intensity profiles are shown for a hydrogel polymerized with $t_{\text{dwell}} = 1/32$ and two loops (solid lines) and a hydrogel polymerized with $t_{\text{dwell}} = 1$ and 64 loops.

entered the inner reservoir over mCherry. The concentration of NTF2-A488 is, in fact, higher in the inner than the outer reservoir, indicating that there is some low concentration of FSFG available in the inner reservoir for binding to NTF2. As the hydrogel was soaked in buffer overnight after crosslinking, any mobile FSFG remaining from the precursor solution has been removed, meaning that the remaining FSFG is most likely anchored into a lightly-crosslinked hydrogel that fills the inner reservoir. The presence of this gel alters the results of an equilibration experiment by artificially increasing the final NTF2 concentration in the inner reservoir.

With help from Danielle Konetski and Christopher Bowman, we attempted to address the stray crosslinking by adding a photoinhibitor to the precursor solution. The radical inhibitor 2,2,6,6-tetramethylpiperidine 1-oxyl (TEMPO) can be used in aqueous solution to limit crosslinking [41]. We tested the effect of the photoinhibitor using a precursor solution as described above with the addition of 0.5 mM TEMPO. While the edges of the resulting hydrogels became marginally sharper, stray crosslinking was still evident, especially in the inner reservoir.

Another significant problem was swelling and buckling of the hydrogels. Despite the hope that thinner hydrogels would swell and equilibrate more easily, buckling of the rings and lines was pervasive and difficult to predict (Fig. 3.12). Ring hydrogels in particular often developed minor leaks due to buckling. Despite a great many attempts to improve the swelling problem (see various other sections), the rings ultimately could not be used for selective transport experiments.

One interesting feature of confocal crosslinking is the degree of control it affords over the illumination method. In the A1R's photobleaching mode, the 405 nm laser is raster-scanned over each pixel in the field of view. The shutter is toggled in order to illuminate only pixels within the predefined region of interest. The controls permit the laser intensity, dwell time at each pixel, and number of raster scan loops to be varied. The laser intensity was always kept at 100%, but changing the dwell time and loop number had a dramatic effect on the final properties of the hydrogel.

Generally speaking, a longer dwell time at each pixel and a low number of loops gave the best results. (See if I can try to get dwell times in absolute time instead of fold change.) Figure 3.15 shows post-equilibration profiles for two hydrogel rings made with different illumination settings. Each gel received the same total illumination time, but in one case the dwell time was reduced 32-fold and the loop number increased by the same factor. In both cases, the hydrogels were soaked in PTB buffer overnight and then challenged with 25 μ M NTF2-Alexa488 and mCherry. After 70 minutes, sufficient NTF2 had accumulated in the gel to make the differences between gels obvious. The low-dwell-time hydrogel accumulated less NTF2 and displayed noticeable dips in NTF2 accumulation at both its inner and outer edges. The edge-dip is reminiscent of those noted in the gels crosslinked by photomasking and the UV LED. While the cause of the dip is unclear, it may be the result of diffusion of fresh precursor solution into the edge region over the course of the crosslinking process. The fresh precursor then crosslinks, leading to a dense hydrogel edge that excludes NTF2 and mCherry. This hypothesis is consistent with the observation that a longer dwell time and fewer raster loops largely eliminated the edge dip. With fewer raster loops, there is less opportunity for diffusion of uncrosslinked precursor solution into the gel edge. It should also be noted that the edge dip does not form when an entire droplet of precursor solution is crosslinked with the UV LED (i.e. no mask is used), further supporting the diffusion explanation. In any case, long dwell times and low loop numbers are clearly preferable with confocal crosslinking.

In conclusion, confocal crosslinking has a number of advantages over LED crosslinking, and a corresponding number of obstacles. Despite the attraction of testing selective transport using small hydrogel rings, we ultimately chose to use a much simpler hydrogel geometry and crosslinking

method.

3.8 Nup and transport factor constructs

Figures

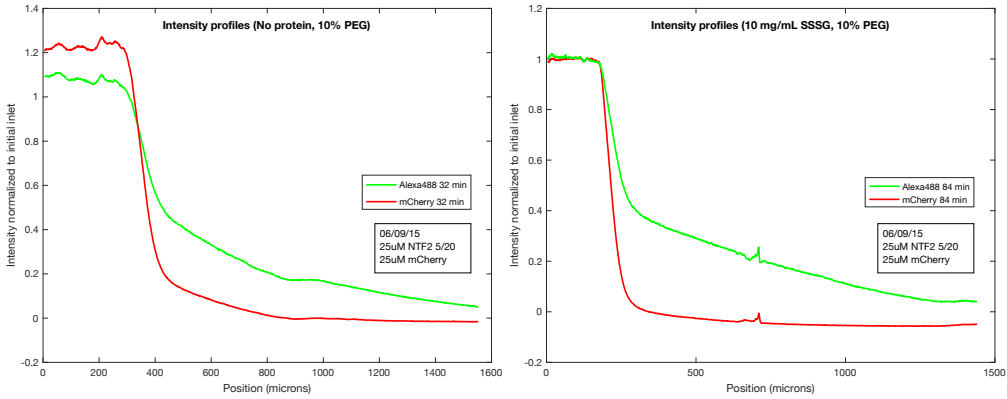
- (1) cartoon of various NTF2 constructs
- (2) table with FSFG variant sequences?
- (3) SDS-PAGE with FSFG cct2?

3.8.1 SSSG negative control

The behavior of NTF2 and mCherry in FSFG hydrogels can be compared to that in hydrogels containing no Nups. However, it is possible that the presence of FSFG in the precursor solution changes the final gel properties such as pore size, or that non-specific interactions between the Nup peptide and test proteins alter the behavior of the test proteins. To account for these possibilities, we designed a negative control peptide which is identical to FSFG except that the phenylalanine residues have been mutated to serine, so that the binding motifs become SSSG. This mutant does not bind NTF2, as demonstrated by the lack of NTF2 accumulation in hydrogels containing SSSG. Figure 3.16 compares the intensity profile of a 10 wt% PEG hydrogel containing a nominal 10 mg/mL SSSG to that of a hydrogel with no nups. There is no dramatic difference between the two profiles, suggesting that the presence of peptide in the hydrogel does not itself alter the diffusion of NTF2 and mCherry. Following the initial tests, SSSG gels were used periodically to confirm that no-Nup gels served well as negative controls, but they were not used regularly as controls.

The SSSG peptide was used in an identical manner to FSFG: SSSG-cys was his-tagged, inserted into pRSF, and expressed in BL21-DE3 Gold cells. It was purified using a cobalt affinity column using the same procedure as FSFG variants and had a high yield. As with FSFG, SSSG is stable and non-aggregating over a wide range of conditions.

Figure 3.16: Comparison of intensity profiles for SSSG and no-nup (control) gels.



3.8.2 Covalently-tethered NTF2 dimer

One recurring problem we observed was that NTF2 moves faster in the hydrogels and equilibrates to a higher level than mCherry, even in SSSG gels or gels with no Nups. This could be because NTF2 is dissociating into two monomers which are smaller and move faster than mCherry. This shouldn't be happening, because the K_D of mammalian NTF2 is about $1 \mu\text{M}$ [49], which should be about the same for our yeast NTF2. However, to avoid this problem, we tried to make a covalently-tethered version of NTF2, consisting of two NTF2 monomers connected by a flexible amino-acid tether. (Look up tether compositions and put in a table.) We tried tethers of several lengths, including 15, 12, and smaller (look this up, it was a mutagenesis accident). Unfortunately, the tether probably messed up the dimerization interface. Look up whether we ever got these expressed and purified. If so, they didn't bind. Maybe show an SDS-PAGE gel for the purification and an accumulation plot/ picture to show they didn't bind. Eric and Scott did most of the cloning work on this project.

10aa – linker :

TSGSGSGSPG

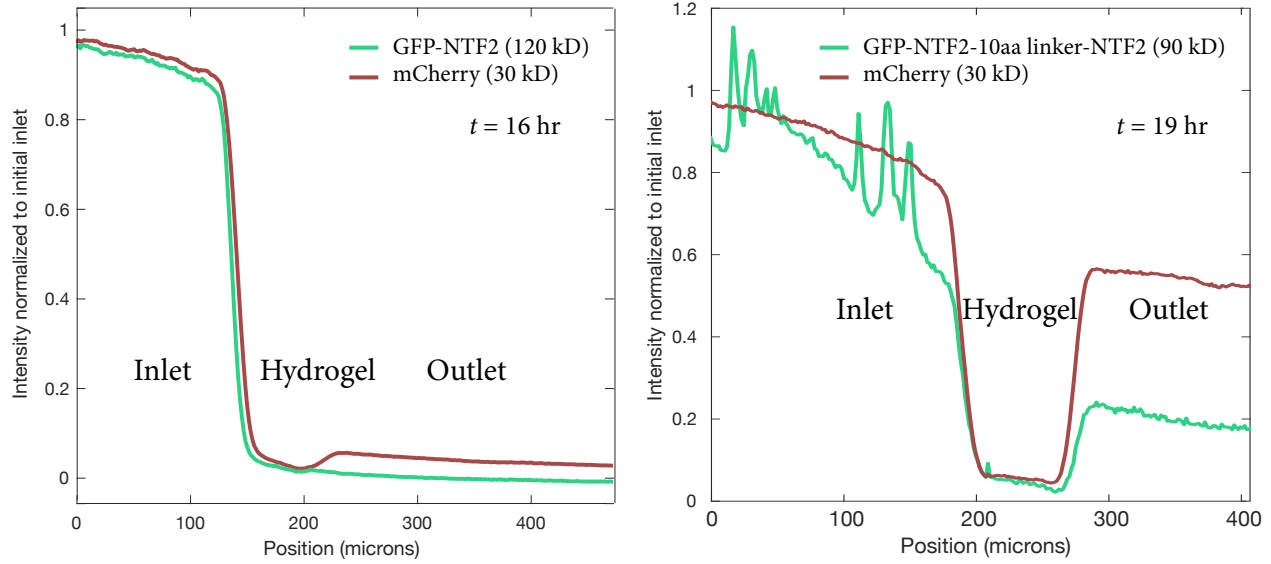
15aa – linker :

TSGS PRGSSGSGSPG

18aa – linker :

TSPGLVSRGSGSGSGSPG

Figure 3.17: Intensity profile for GFP-NTF2 and mCherry showing no binding to FSFG hydrogel.



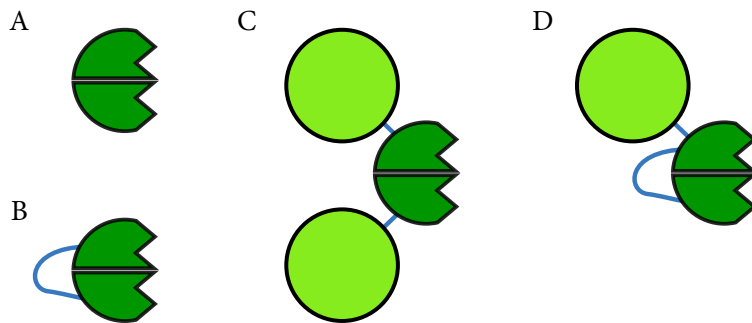
3.8.3 NTF2-GFP

Another recurring problem was free dye in the NTF2 channel. After dye-labeling (see next section), the dye slowly hydrolyzes and leaves the NTF2. In an attempt to fix this problem, Eric Verbeke and I created a version of NTF2 tethered to GFP by a short linker.

This construct is in the pET21 plasmid, his-tagged, and expressed in BL21-DE3 Gold cells. It was purified using a cobalt affinity column in PTB and 1:1000 PIC and eluted with 250 mM imidazole, yielding ample protein with moderate degradation products.

3.8.4 Kap121 and NLS-GFP

The karyopherins (Kaps) are a canonical class of transport factors. They transport proteins tagged with nuclear localization signals (NLS) through the nuclear pore. We were interested in testing Kaps because they are widely studied and much larger than NTF2, so selective transport would be more apparent. Eric Verbeke engineered two GFP-NLS constructs: GFP-Spo12 and GFP-Pho4. These constructs were his-tagged, inserted into pET21b, expressed in BL21-DE3 Gold cells, and purified using a cobalt affinity column. Kap121-GST was expressed and purified following [37]

Figure 3.18: Cartoon of various NTF2 constructs

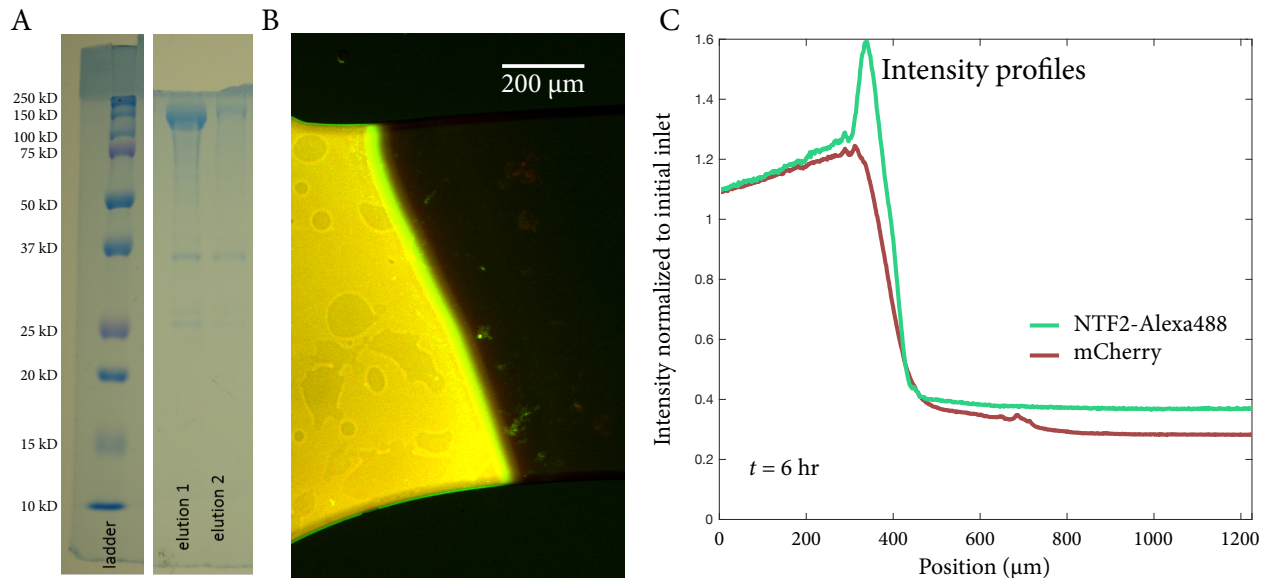
and the GST subsequently cleaved with thrombin resin (Fig. 3.19 a).

Kap121 binding and influx was tested using a hydrogel made from precursor solution containing 0.05 wt% Irgacure2959, 110 mg/mL 20kD 8-armed PEG-norbornene, 11 mg/mL 1kD PEG-dithiol, and 1 mM TCEP in PTB, crosslinked for 2 minutes under the UV LED. After soaking in PTB overnight, 5 μ M Kap121, 10 μ M GFP-Pho4, and 100 μ M mCherry in PTB were added to the inlet reservoir. Selective influx of the Kap121/GFP-Pho4 complex was evident, since the complex accumulated at the edge of the hydrogel (Fig. 3.19 b and c). The bright band demonstrates binding of FSFG to Kap121 as well as of Kap121 to GFP-Pho4. Over the course of several hours, the GFP front remained localized at the edge of the gel, likely indicating that the pore size of the hydrogel was too small to accomodate the Kap121/GFP-Pho4 complex. Given the large size of this complex, the pore size was never increased sufficiently for influx into the hydrogels.

3.8.5 FSFG concat 2 and concat 3

In order to test the effect of Nup length and number of binding sites, we used multiple versions of FSFG. We got these versions from Loren's old lab and didn't really modify them. Eric may have added a cysteine for labeling. FSFG concat 2 is twice as long, and FSFG concat 3 is three times as long. Maybe I should include sequences of all three FSFG variants. Both variants express in principle, but I could only get FSFG concat 2 to express. I purify it using the same method as FSFG concat 1 (the original form, with 124 amino acids and 6 FSFG repeats).

Figure 3.19: SDS-PAGE showing Kap121 purification (purified by Chris Lawton), picture of influx, intensity profiles



3.9 Dye-labeling and free dye

Figures

- (1) Typhoon image of dye, Matlab peaks
- (2) Example of single- and double- exponential fits
- (3) goodness of fit measurements for single- and double- exponential fits

We have to label NTF2 with a fluorescent dye to use it as a test transport factor. For the most part, we've used Alexa Fluor 488 as the dye. (Most recently we switched to fluorescein because it's easier to photobleach.) There are several choices of labeling chemistry. We've used both NHS and SDP esters, which label the exposed lysines of NTF2, of which there are several. We've also tried using Alexa488-maleimide to label the cysteine of an engineered NTF2-cys. Both labeling chemistries result in bonds that eventually hydrolyze, cleaving the dye from the protein. This is a major problem for the experiments, since free dye (about 1kD) diffuses much faster than dye bound to a protein and is experimentally identical. Non-negligible levels of free dye would give the impression that NTF2 is equilibrating significantly faster than it actually is. The maleimide-labeling chemistry is more stable, but in practice not as efficient as the ester-labeling protocol. It also requires using NTF2-cys, which could introduce other issues. Mostly I stuck with the lysine-labeling protocol, which needed significant optimization to minimize free dye issues. Eric did a lot of work in optimizing the cysteine-labeling protocol, and I took his work as a base in optimizing the lysine-labeling protocol.

3.9.1 Labeling NTF2 with fluorescein-NHS

- (1) Resuspend lyophilized fluorescein-NHS at 100 mg/mL in anhydrous DMSO in the dark-room. Discard the remaining DMSO aliquot. Make 100- μ L aliquots of dye solution. Store with desiccant in ultra-low freezer, protected from light.

- (2) Mix NTF2 in PTB pH 7.0 and 100 mg/mL fluorescein-NHS in DMSO with around 15-fold molar excess dye. Several other buffers can be used as well (see Thermo protocol). A typical labeling reaction used 0.5 mL of 16 mg/mL NTF2 and 18.6 μ L dye stock mixed in an Eppendorf with an Eppendorf stir bar.
- (3) Incubate mixture, stirring, protected from light, at room temperature for one hour.
- (4) Equilibrate TALON cobalt resin with PTB in a column that can be spun in a centrifuge. TALON resin has a stated capacity of 5-15 mL protein per mL resin. Using significantly more than needed can lead to nonspecific binding of free dye. A typical reaction required 1.6 mL of the resin slurry. Equilibrate with at least 10 bed volumes PTB.
- (5) Cap column and add reaction mixture. Nutate at 4°C for one hour, protected from light.
- (6) Allow column to drain and wash with approximately 100 bed volumes of PTB, protected from light as best as possible. Occasionally cap column and resuspend resin to remove free dye from column cap and sides. Test flow-through using UV light to ensure that no dye is visible by the end of the wash. Resin should still be bright yellow.
- (7) Spin column 1000 rpm (convert to rpm, spun in 15 mL conical) for one minute to remove remaining wash buffer. Immediately cap and elute with 1 mL of 300 mM imidazole in PTB. Nutate 4°C for half an hour and collect elution. Resin should return to pink.
- (8) Dialyze elution against PTB to remove imidazole. No more than 24 hours after labeling, aliquot and freeze labeled NTF2.
- (9) Run a sample of labeled NTF2 on a native PAGE gel along with a sample of fluorescein-NHS. Use the Typhoon to compare the concentration of free dye to labeled protein in the protein sample.

3.9.2 Labeling NTF2 with Alexa Fluor 488 - SDP

- (1) Resuspend lyophilized Alexa Fluor 488 at 10 mg/mL in anhydrous DMSO in the darkroom. Discard the remaining DMSO aliquot. Make 10- μ L aliquots of dye solution. Store with desiccant in ultra-low freezer, protected from light.
- (2) Mix NTF2 in 0.1 M sodium bicarbonate buffer and 10 mg/mL fluorescein-NHS in DMSO with around ??-fold molar excess dye. A typical labeling reaction used 200 μ L of 16 mg/mL NTF2 and 20 μ L dye stock mixed in an Eppendorf with an Eppendorf stir bar.
- (3) Incubate mixture, stirring, protected from light, at room temperature for one hour.
- (4) Equilibrate TALON cobalt resin with PTB in a column that can be spun in a centrifuge. TALON resin has a stated capacity of 5-15 mL protein per mL resin. Using significantly more than needed can lead to nonspecific binding of free dye. Equilibrate with at least 10 bed volumes PTB.
- (5) Cap column and add reaction mixture. Nutate at 4°C for one hour, protected from light.
- (6) Allow column to drain and wash with approximately 100 bed volumes of PTB, protected from light as best as possible. Occasionally cap column and resuspend resin to remove free dye from column cap and sides. Test flow-through using UV light to ensure that no dye is visible by the end of the wash. Resin should still be bright yellow.
- (7) Spin column 500 rpm (convert to rpm, spun in mini centrifuge) for 20 s to remove remaining wash buffer. Immediately cap and elute with 300 μ L of 500 mM imidazole in PTB. Nutate 4°C for half an hour and collect elution. Resin should return to pink.
- (8) Dialyze elution against PTB to remove imidazole. No more than 24 hours after labeling, aliquot and freeze labeled NTF2.
- (9) Run a sample of labeled NTF2 on a native PAGE gel along with a sample of fluorescein-NHS. Use the Typhoon to compare the concentration of free dye to labeled protein in the

protein sample.

3.9.3 Labeling NTF2-cys or FSFG-cys with Alexa Fluor 488 - maleimide

- (1) Resuspend lyophilized Alexa Fluor 488 at 10 mg/mL in anhydrous DMSO in the darkroom. Discard the remaining DMSO aliquot. Make 10- μ L aliquots of dye solution. Store with desiccant in ultra-low freezer, protected from light.
- (2) Mix protein in PTB pH 7.0 and 50 μ M TCEP (with no other reducing agent present) and 10 mg/mL dye in DMSO. Check molar ratios, pg 70 LKM book 5.
- (3) Incubate mixture, stirring, protected from light, at room temperature for two hours.
- (4) Equilibrate TALON cobalt resin with PTB in a column that can be spun in a centrifuge. TALON resin has a stated capacity of 5-15 mL protein per mL resin. Using significantly more than needed can lead to nonspecific binding of free dye. Equilibrate with at least 10 bed volumes PTB.
- (5) Cap column and add reaction mixture. Nutate at 4°C for one hour, protected from light.
- (6) Allow column to drain and wash with approximately 100 bed volumes of PTB, protected from light as best as possible. Occasionally cap column and resuspend resin to remove free dye from column cap and sides. Test flow-through using UV light to ensure that no dye is visible by the end of the wash. Resin should still be bright yellow.
- (7) Spin column 500 rpm (convert to rpm, spun in mini centrifuge) for 20 s to remove remaining wash buffer. Immediately cap and elute with 300 μ L of 500 mM imidazole in PTB. Nutate 4°C for half an hour and collect elution. Resin should return to pink.
- (8) Dialyze elution against PTB to remove imidazole. No more than 24 hours after labeling, aliquot and freeze labeled NTF2.

- (9) Run a sample of labeled NTF2 on a native PAGE gel along with a sample of fluorescein-NHS. Use the Typhoon to compare the concentration of free dye to labeled protein in the protein sample.

0.1 M sodium bicarbonate buffer and 10 mg/mL fluorescein-NHS in DMSO with around ??-fold molar excess dye. A typical labeling reaction used 200 μ L of 16 mg/mL NTF2 and 20 μ L dye stock mixed in an Eppendorf with an Eppendorf stir bar.

The major change is the increased wash step, and the immediate aliquoting and freezing before use. I also began to be much more careful with characterizing the results of the labeling. Immediately after finishing dialysis, I run a BCA to quantify the protein concentration in the labeled sample. The same day, I aliquot and freeze all the protein except a sample for the remaining tests. As soon as possible, I run a native PAGE gel, including the labeled protein sample as well as a free dye sample. After running the gel, I image it in the Alexa488 channel using the Typhoon, and then stain with Coomassie to make sure the protein hasn't degraded. I use Matlab to compare the amplitude of the labeled-protein band and the free-dye band that remains in the labeled-protein sample. Typically, the free dye band is 1-3% the amplitude of the labeled-protein band. Finally, I measure the absorbance of the labeled protein at 494 (check this wavelength) nm and use Beer's law to find the concentration of Alexa488. I can compare this measurement with the protein measurement from the BCA to calculate a labeling efficiency. Include some sample efficiencies here. I typically get lower efficiencies than other people report. I spoke to Annette and she had no major suggestions. In principle, doing the reaction under nitrogen would help, but Annette gets something like 90% efficiency without doing that. I use the labeled NTF2 immediately after thawing if possible, and no more than a week after thawing.

We also tried to make NTF2-GFP to fix the free dye problem (see section above).

In addition to the tests I run on each batch of labeled NTF2, at one point I did some mathematical analysis to confirm that the free dye was only a minor problem in the experiments I had already run. In order to confirm that, I fit the accumulation curves to single or double

exponentials (they really should have been erfc functions but I approximated.)

If there is no free dye, as in the case of the mCherry accumulation, the accumulated intensity $I(t)$ can be approximated as

$$I(t) = A_1 \exp(-t/\tau_1) + C \quad (3.1)$$

with some amplitude A_1 , equilibration lifetime τ_1 , and constant offset C . In this case, a non-zero value of C is likely due to background fluorescence. If, on the other hand, a sample contains a population of small, free dye molecules as well as large labeled protein, both populations will equilibrate at different rates, leading to an accumulated intensity of

$$I(t) = A_1 \exp(-t/\tau_1) + A_2 \exp(-t/\tau_2) + C \quad (3.2)$$

where each population has an equilibration lifetime as well as an amplitude related to its abundance in the sample.

I fit a collection of 43 accumulation experiments to both Eqns. 3.1 and 3.2. I compared the resulting parameters as well as the adjusted R-square value of each fit. Adding more parameters to the fit will always improve the fit, but the adjusted R-square is intended to account for the effect of adding more parameters to a model. A higher adjusted R-square therefore means a better fit.

The mCherry accumulation fits did not noticeably improve when moving from the single to the double exponential. In addition, the lifetimes and amplitudes of each component of the two-component fit were apparently uncorrelated. Both results support the fact that there is no free dye in the red channel, since the only fluorescence is coming from mCherry.

On the other hand, the NTF2 fits did result in a higher adjusted R-square value on average with the double-exponential fit. Strikingly, the two components sorted themselves into two categories: a low-amplitude, short-lifetime component and a high-amplitude, long-lifetime one. The most straightforward interpretation is that the low-amplitude component is the free dye, which should be present in low amounts and equilibrate much more rapidly than labeled protein, thanks to its small size.

The median amplitude of the free-dye signal was 1.2% that of the labeled-protein signal,

using a sample of 43 experiments. The median free-dye equilibration lifetime was 50 minutes, as compared to approximately 2000 minutes for the labeled-protein lifetime. These results confirm that the new, more stringent dye-labeling protocol is successful in removing almost all free dye from the labeled-protein sample, and that the hydrolysis of the dye is negligible on the time scale of the experiment and enforced shelf life of the labeled protein.

Also made GFP-NTF2 (didnt bind to FSFG)

Chapter 4

Bound diffusion measurements

Following up on the principles of the bound-diffusion theory, we wanted to see whether we could measure bound diffusion in a biomaterial inspired by the nuclear pore complex. In order to do that, we made Nup-filled hydrogels and measured the diffusion of transport factors and inert proteins within them. We measured the diffusion in a few different ways: monitoring the concentration profile and total accumulation as the proteins diffused into the cell, and using fluorescence recovery after photobleaching (FRAP).

4.1 Experimental setup

4.1.1 Hydrogels

Applying the lessons learned in the previous chapter, the nuclear pore mimics were 6% acrylamide hydrogels with FSFG-bis anchored in. The precursor solution had a final concentration of 6% premixed acrylamide/bisacrylamide (29:1) in PTB pH 7.0. The crosslinker was either 1 mM LAP or 0.1% ammonium persulfate and 0.5% TEMED (check these concentrations). Lyophilized FSFG-bis was resuspended in PTB, allowed to sit at room temperature for at least 20 minutes, and added to the precursor solution. I used nominal FSFG concentrations between 5 and 10 mg/mL, depending on whether it was FSFG concat 1 or FSFG concat 2. If a photoinitiator was used, it was added in the darkroom, and the solution was protected from light as much as possible afterwards.

After the precursor solution was thoroughly mixed, it was degassed in a vacuum desiccator for 10 minutes and immediately pipetted into a disassembled 400- μ m-thick PDMS gasket chamber.

Drops between 0.5 and 2 μL were carefully pipetted onto the plastic slide and the chamber assembled around the drops. Typically, each chamber measured a few centimeters on a side and contained a control gel with no Nups as well as one or more Nup-filled gels. The chamber was then illuminated with UV light at some intensity that I will look up as uniformly as possible for 30 seconds using a ThorLabs etc. LED. Condensation around the gels indicated that they had crosslinked. The chamber was immediately rinsed with at least 100 μL of PTB, filled with fresh PTB, and sealed with PDMS and clingwrap. The gels were left to soak at 4°C for at least 12 hours so that any remaining precursor solution and protein could leave the gel.

4.1.2 Influx experiments

After soaking in buffer, the buffer solution was removed by pipette or wicking with a Kimwipe (not by aspirating) and a fluorescent reservoir solution added. The reservoir solution contained 20 μM each NTF2-fluorescein (NTF2-F) and mCherry in PTB. The chamber was resealed after adding the solution. If a profile and accumulation experiment was being run, the experiment was run immediately after adding the reservoir solution. Experiments were run on an Olympus widefield using a 4x objective with FITC and TRITC filter cubes (should I put exact specifications here). Typical experiments were run for 120 minutes at a rate of one frame per minute. Exposure times were usually 30-100 ms with 3-8 dB gain in both channels. Minimal photobleaching took place over the course of these experiments. Data was analyzed as described below. After the end of an influx experiment, the chamber could be stored at 4°C, protected from light, for a further 12-24 hours in order to equilibrate. A FRAP experiment could then be performed.

4.1.3 Fluorescence recovery after photobleaching

Fluorescence recovery after photobleaching (FRAP) relies on the redistribution of fluorophores after patterned photobleaching in order to determine their diffusion constant. After a small portion of the hydrogel is bleached, the bleached spot gradually exchanges with the non-bleached fluorophores outside, and the average fluorescence intensity within the bleached spot recovers. The

recovery lifetime can be used to determine the fluorophore's diffusion constant, and the final recovered intensity as compared to the intensity outside the bleach spot can be used to determine the mobile fraction of fluorophore.

FRAP is often performed with a confocal microscope, but we were able to manage it with the Olympus widefield. In order to photobleach the gel, a 40x objective was used and the field of view exposed to near-UV (the DAPI cube - find precise specifications) at maximum power for 5 seconds. The objective was rapidly changed to 4x and a time series begun. Typical time series consisted of 15-30 frames taken as rapidly as possible (5-10 seconds per frame) and 30-60 frames taken at a slower rate (1-2 minutes per frame). Total experiment time ranged from 1 to 4 hours. Typical exposure times were 10 ms for NTF2-F and 40 ms for mCherry with a gain of 3 dB for both channels.

We had problems equilibrating the gels. Sometimes the gels were crosslinked inhomogeneously, and sometimes they didn't fully equilibrate even after 24 hours. Smaller gels ($0.5 \mu\text{L}$) helped solve the equilibration problem, but then the exchange of fluorescent proteins with the buffer was a major problem, because a significant fraction of the gel area was being bleached. We accounted for these problems during the data analysis, described below.

4.2 Influx analysis

In principle, the diffusion constants of NTF2-F and mCherry within the NPC mimics can be determined using the concentration profiles or total fluorescence accumulation within the hydrogel over time. We used several mathematical models to fit the profiles and accumulation in an attempt to extract diffusion coefficients. The noise inherent in the data made this difficult, and ultimately we used FRAP instead to find the diffusion constants.

Fickian diffusion was always assumed, although in practice the presence of binding and of the hydrogel network lead to slightly non-Fickian behavior. It was also assumed that the length of a binding event was negligible on the timescale of diffusion, so that the observed diffusion constant of the NTF2-F could be treated as Fickian diffusion and written as a weighted average of the diffusion

constants while free and bound. This is a good approximation because we think the dissociation constant of NTF2 and FSFG is $K_D \approx 1$ mM, with a diffusion-limited on-rate and correspondingly high off-rate.

4.2.1 Profile analysis

Using these assumptions, the method of [?] was followed in order to fit the profile and accumulation data. This method assumes that an arbitrary shape is initially empty but held in an infinite reservoir kept at a constant concentration. The shape fills according to the diffusion equation. Although there are slightly different numerical factors for different shapes, they show that a circle is a good approximation for many shapes. Since our gels are usually nearly circular, the circular solution is a good one. Using this method, the protein concentration $c(r, t)$ as a function of radial distance r from the gel center and time t is given by

$$\frac{c(r, t)}{c_0} = 1 - 2 \sum_{n=0}^{\infty} \frac{J_0(\alpha_n r)}{\alpha_n a J_1(\alpha_n a)} \exp(-\alpha_n D t) \quad (4.1)$$

where c_0 is the equilibrium concentration within the shape, D is the diffusion constant, a is the shape radius, and $\alpha_n a$ is the n th zero of the Bessel function of the first kind J_0 .

Mortensen et al define a characteristic timescale for equilibration $\tau = (\mathcal{A}/\mathcal{P})^2(\pi/4D)$ where \mathcal{A} and \mathcal{P} are the shape's area and perimeter, respectively. For a circle $\mathcal{A}/\mathcal{P} = a/2$, but this ratio can be numerically calculated for our hydrogels using their precise shapes. For times $t \ll \tau$, the concentration profile can be approximated as

$$c(r, t) = c_0 \operatorname{erfc} \left(\frac{r}{\sqrt{4Dt}} \right) \quad (4.2)$$

In order to fit to these equations, I averaged the intensity of a thin slice cutting through the reservoir and the gel to the center of the gel. I normalized the data by dividing by the average reservoir intensity (the entire reservoir in the field of view, not just the thin slice). I normalized on a time-point basis to eliminate drift in the illumination or reservoir concentration. After normalizing, I tried to fit the first time-points to Eqn. 4.2, both at a fixed time for many positions and vice

versa. The fits worked fairly well for the NTF2-F plots, as those had a well-defined gel edge. It was more difficult for the mCherry fits.

I also tried to use the full equation, Eqn. 4.1. I fit to the first 100 terms using Matlab, and that worked slightly better, but it was still difficult for the mCherry fits.

4.2.2 Accumulation analysis

Next, I tried to fit to the total accumulation. From Mortensen et al, the averaged intensity inside the gel $N(t)$ is

$$\frac{N(t)}{N_0} = 1 - \sum_{n=0}^{\infty} \frac{4}{(\alpha_n a)^2} \exp\left(-\frac{(\alpha_n a)^2 \pi t}{16\tau}\right) \quad (4.3)$$

I fit the first 100 terms of this in Matlab, but it didn't work terribly well either. This one worked better for mCherry than for NTF2-F, likely because binding was throwing off the NTF2 results. Overall, the most important data points were near the edge of the gel and the beginning of the experiment, and the edge effects and uncertainty in experiment start time meant that both of those types of points had lower signal-to-noise than the rest of the experiment.

4.2.3 Gel dimension estimations

In order to fit the influx and FRAP data, I needed to estimate several parameters of the gel geometry: the radius of the gel, its perimeter, and its area. Although the gels were not perfectly circular, most were close, and so I took the radius to be half of the longest dimension in the video's field of view. Typically, the entire gel did not fit into the field of view. To estimate the radius, I used the mask of the entire gel and counted the number of non-zero elements by row. I took the maximum number of nonzero elements, divided by two, and multiplied by the pixel spacing: 1.58 μm per pixel for the 4x objective on the Olympus widefield.

To estimate the area and perimeter, I embedded the image in a larger frame, and created a ROI that covered the entire gel, estimating where necessary. I summed the non-zero elements of the ROI and scaled using the pixel spacing. For the perimeter, I called the Matlab function that returns only the outline of an ROI, and summed and scaled that.

4.2.4 Partition coefficient and bound probability calculations

In order to calculate the bound diffusion coefficient, I needed to estimate the amount of time that a given transport factor spends bound to Nups. When the system is in chemical equilibrium, the concentration of free transport factor (T), free Nup (N), and transport factor - Nup complex (C) is related to the dissociation constant K_D by $K_D = NT/C \approx N_T T/C$ in the linear approximation $N \approx N_T$ when N_T is the total Nup concentration, both free and bound, and is a constant. The fraction of transport factors that are bound is then given by

$$p_B = \frac{C}{C+T} = \frac{C}{C + \frac{CK_D}{N_T}} = \frac{1}{1 + \frac{K_D}{N_T}} \approx 1 - \frac{K_D}{N_T} \quad (4.4)$$

where the final step applies if $K_D \ll N_T$, which might be the case but now I'm confused again.

It's difficult to measure the total Nup concentration anchored to the hydrogels, so we'd like to remove that term in favor of an experimental quantity that's easier to measure. The partition coefficient is much easier to measure. The partition coefficient is the ratio of a fluorescent protein's concentration just inside and just outside an equilibrated hydrogel. To measure it, just take the ratio of the average intensity within the gel to that in the reservoir. The concentration c_0 of the inert protein and the transport factor is equal in the reservoir. If γ_T is the partition coefficient of the transport factor and γ_I that of the inert protein, then the transport factor concentrations can be expressed as

$$T = \gamma_I c_0 \quad (4.5)$$

$$C = T_T - T = \gamma_T c_0 - \gamma_I c_0 \quad (4.6)$$

The total transport factor concentration within the gel is $T_T = T + C$ and is a constant. Therefore, within the gel, the chemical equilibrium condition can be expressed as

$$\frac{K_D}{N_T} = \frac{T}{C} = \frac{\gamma_I c_0}{\gamma_T c_0 - \gamma_I c_0} = \frac{\gamma_I}{\gamma_T - \gamma_I} \quad (4.7)$$

Combining Eqns. 4.4 and 4.7, the bound probability can be expressed only in terms of the partition coefficients as

$$p_B = \frac{1}{1 + \frac{K_D}{N_T}} = \frac{1}{1 + \frac{\gamma_I}{\gamma_T - \gamma_I}} = 1 - \frac{\gamma_I}{\gamma_T} \quad (4.8)$$

4.2.5 Bound-diffusion calculation

Once the observed diffusion constants for NTF2 and mCherry have been calculated, along with the bound probability (using the partition coefficients), the bound diffusion is given straightforwardly by the weighted average

$$D_{\text{obs,TF}} = p_B D_B + (1 - p_B) D_F \quad (4.9)$$

Taking the free diffusion coefficient of the transport factor to be approximately equal to the observed diffusion of the inert protein ($D_F = D_{\text{obs,I}}$), the bound diffusion coefficient of the transport factor is

$$D_B = \frac{D_{\text{obs,TF}} - (1 - p_B) D_{\text{obs,I}}}{p_B} \quad (4.10)$$

4.3 FRAP analysis

4.4 Discussion

Chapter 5

FG Nup aggregation under crowded conditions

Disordered proteins are often prone to aggregation, often causing disease, and the aggregation behavior of FG Nups is important to understand. It is not clear what the aggregation state of Nups is within the pore or how their aggregation might play into nuclear transport [?]. *In vitro*, many Nups spontaneously aggregate into amyoids over the course of a few hours, but there is evidence that this aggregation does not happen in the cellular environment [?, 14]. We investigated aggregation behavoir of an aggregation-prone Nup fragment in a number of different crowders. Inert crowders such as PEG and PVP help mimic the extremely crowded cellular environment, but they may interact different with the protein than nonspecifically-binding crowders such as cell lysate or BSA. We wanted to understand how different crowders affected the aggregation properties of Nups.

We used a 124-amino-acid fragment of the Nup Nsp1. The FG-repeat segment of Nsp1 contains an aggregation-resistant portion (used as the basis for the FSFG peptide) as well as one that aggregates in buffer over the course of a few hours. This aggregation-prone portion is the basis of the FG124 peptide used in the following aggregation experiments.

We used aggregation timecourses with thioflavin T as a readout, as well as fluorimetry, NMR, and x-ray scattering. Our conclusion is something about the phenylalanines and how they behave differently in when crowded with PEG than with PVP (which also has an aromatic ring).

5.1 Results

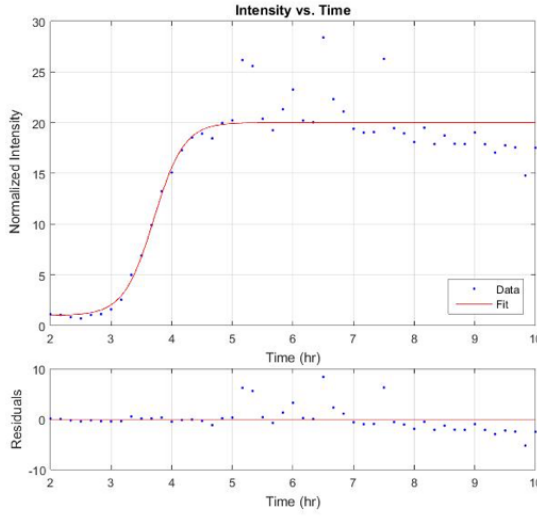
5.1.1 Thioflavin timecourses

We analyzed aggregation dynamics using thioflavin T, a fluorophore whose excitation and emission maxima shift and which grows much brighter in the presence of thioflavin. Samples containing FG124, crowding agent, and thioflavin T were incubated while shaking overnight in a 96-well plate and their fluorescence intensity recorded every ten minutes. The resulting traces show a typical aggregation pattern, with a lag phase, burst phase, and saturation phase.

Thioflavin T (ThT) is a dye that grows much brighter when bound to amyloids. Upon binding, its absorption maximum shifts from 385 nm to 450 nm and its emission maximum from 445 nm to 482 nm [50]. Although ThT is a more reliable indicator of amyloids than other fluorescence methods, notably Congo red stain, it suffers from reproducibility problems. There is no consensus on the mechanism of ThT binding to amyloids. Some proposed mechanisms rely on the presence of ThT micelles, which form above a critical concentration of about 4 μ M, while others advocate for avoiding micelles [51, 52]. There is some evidence that amyloid fibrils can adsorb to the plastic surface of a multiwell plate, decreasing ThT fluorescence intensity as the fibrils mature [53]. Often in our timecourse experiments, the ThT fluorescence did reach a maximum and then decrease. The fluorescence intensity also depends on the sample pH, an effect which we noticed in our timecourses. Despite these challenges, thioflavin T is the most consistent dye for detecting the process of amyloid formation.

The final concentration of crowding agent was 19% serine w/v, 13% PEG, and 13% PVP. Lysate concentration varied between time courses and was in the 1-10 mg/mL range. Two timecourses were run with varying PEG and PVP concentrations: 25%, 20%, 13%, and 5%. Samples with no crowding agent ('buffer' samples) were run as a reference, and samples in 7M guanidine hydrochloride (GuHCl) with no crowding agent were run as negative controls in each timecourse. No aggregation was observed in the GuHCl samples. In every case, blanks were run alongside the sample conditions. In the blanks, the FG124 was omitted.

Figure 5.1: Sample sigmoid fit. Look up conditions. (Pulled this from Sophie's thesis but I did the fit)



First the data were normalized to the blanks. In nearly all cases, the blank intensity remained steady over time, as expected. In those cases, the mean blank intensity was subtracted from the corresponding data. (In cases where the blank intensity changed over time, it was subtracted pointwise from the data.)

Then the normalized curves were fit to a sigmoid given by

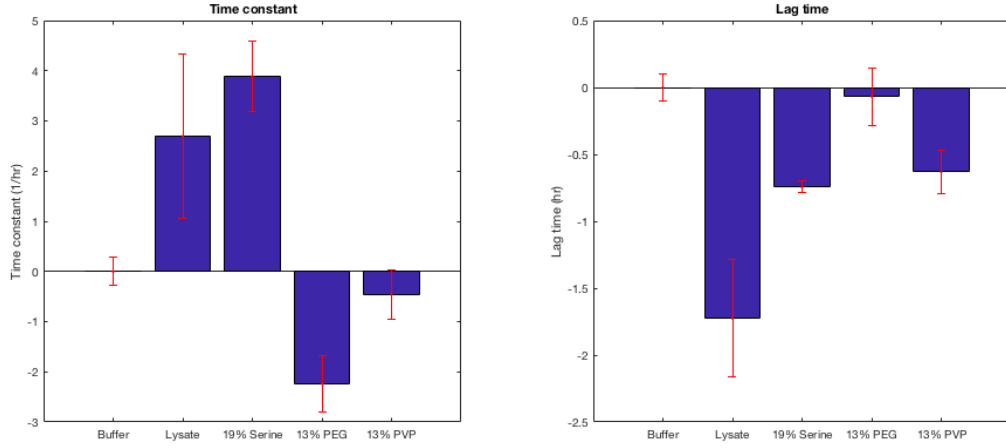
$$I(t) = C + \frac{A}{1 + \exp(-k(t - T_{1/2}))} \quad (5.1)$$

where $I(t)$ is the normalized fluorescence intensity as a function of time. The useful physical parameters for our purposes are the time constant k , which gives a measurement of the steepness of the slope at the beginning of the burst phase, and the lag time T_l . The lag time is calculated as

$$T_l = T_{1/2} - \frac{2}{k} \quad (5.2)$$

and represents the duration of the lag phase [].

Ideally, we expect $C = 1$, as aggregation should not have begun at the start of the experiment, so there should be no increase in sample fluorescence over that of the blank. Experimentally, C usually ranged between 1 and 2, up to about 10 for some sample conditions. This might have been

Figure 5.2: test

because aggregation had already begun, but this seems unlikely because the lag phase continued for some time. I don't know why C wasn't close to unity for all conditions and replicates.

The saturation phase asymptotes to an intensity given by $I_{\text{sat}} = C + A$. We found significant variation in I_{sat} for the same condition between timecourses, and the relative magnitudes of different conditions also varied between timecourses. I think this is a limitation of the thioflavin tests. Therefore, we do not consider I_{sat} in our analysis, leaving k and T_l as parameters of interest.

Next we normalized once again to account for differences between timecourses. It was impossible to hold the concentration exactly fixed between timecourses, and there were probably some other environmental variables we couldn't control perfectly, so it was important to normalize again. Within each timecourse, we averaged the fit parameters for all buffer replicates and subtracted that average from each other replicate.

We then combined replicates from all timecourses by condition and took the final average and standard error of the mean for both fit parameters. The results are shown in Fig. 5.2. I ran a one-factor ANOVA to reject the null hypothesis that all means were the same, and then two-sample t-tests on each pair of conditions to find which differences were statistically significant. For the time constant, all pairs of conditions were significantly different from each other with $p < 0.05$.

except buffer-PVP. For the lag time, all pairs of conditions were significantly different from each other with $p < 0.05$ **except** buffer-PEG and serine-PVP.

I followed the same process for the timecourses involving the concentration series for PEG and PVP, but there were fewer significant differences between concentrations, as seen in Fig. 5.3. The ANOVA for the PEG time constants gave $p = 0.0024$ with the t-test showing differences between: buffer-25% PEG, buffer-13% PEG, and 25% PEG-20% PEG. The ANOVA for the PEG lag times was likewise significant with $p = 0.0102$. The significant pairs were: buffer-25% PEG, buffer-20% PEG, buffer-5% PEG, and 25% PEG-13% PEG.

For PVP, there were no significant differences in the time constant. For the lag time, after the ANOVA and t-tests, there were differences between: buffer and everything except 5% PVP, 25% PVP and everything but 20% PVP, and 20%PVP-13% PVP.

For both conditions, it looks roughly like the lag time increases with the crowder concentration, but given the large error bars, I wouldn't read too much into it. The time constants don't follow any particular trend and are mostly indistinguishable anyway.

We tested the effects of pH on FG124 aggregation by running several experiments in buffer at varying pH. We ran six replicates of each condition, for pH values between 5 and 8. No significant differences were found in the lifetimes or lag times of any pH condition. Results are summarized in Table 5.1. We concluded that aggregation is not affected by pH in the range 5-8.

Table 5.1: FG124 aggregation lifetime and lag time with varying pH. Each condition run with 6 replicates in PTB buffer. One-way ANOVAs show no statistically significant differences between conditions. Standard errors are shown.

pH	Lifetime τ (hr)	Lag time T_{lag} (hr)
5	0.34 ± 0.09	6.8 ± 0.1
6	0.35 ± 0.12	6.2 ± 0.2
7	0.38 ± 0.14	6.8 ± 0.4
8	0.50 ± 0.14	6.6 ± 0.2

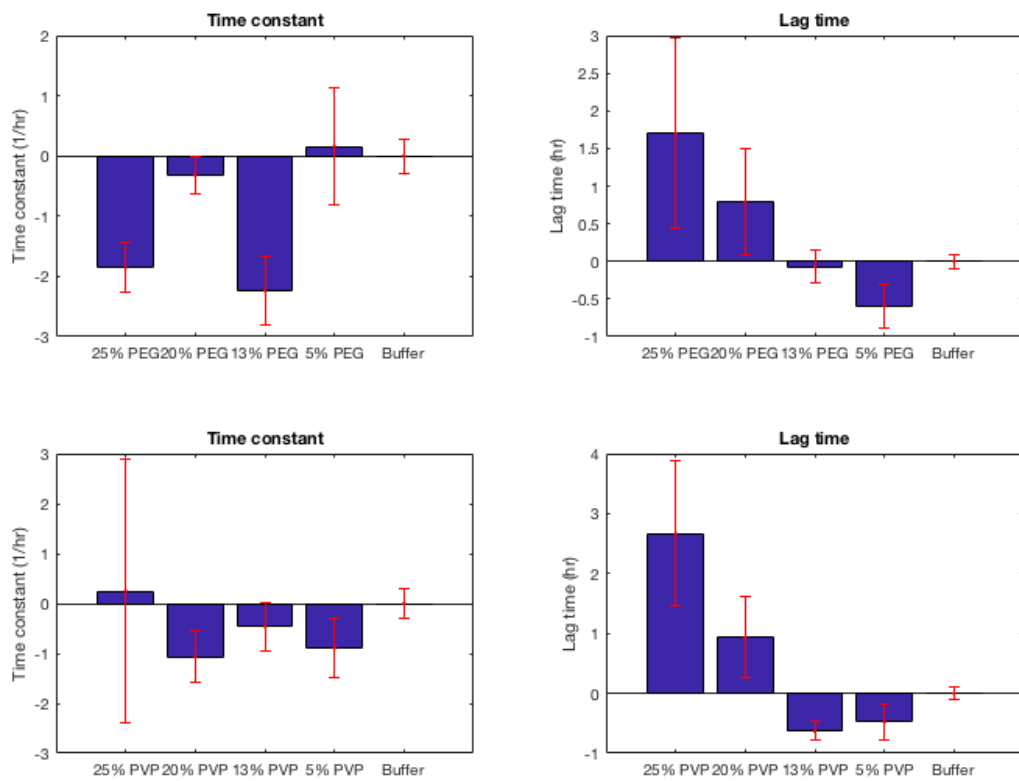
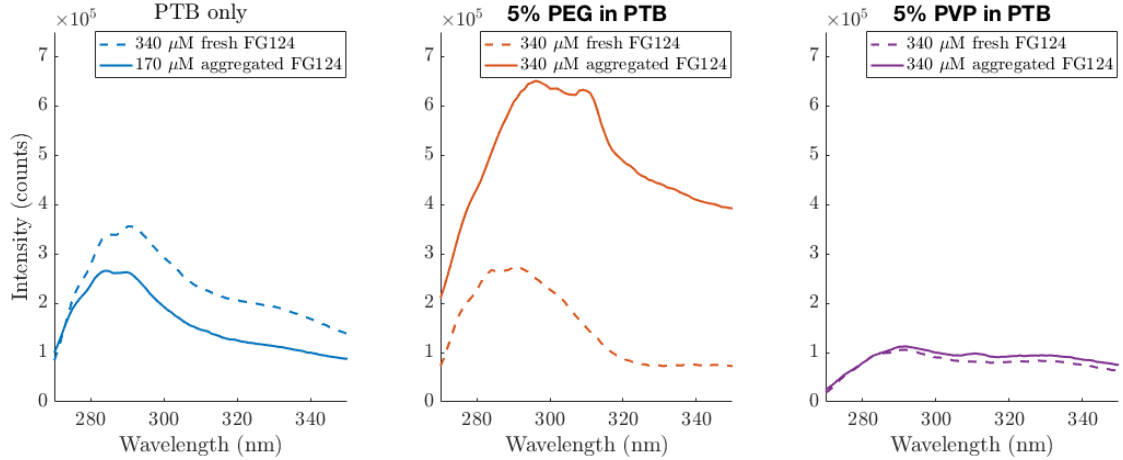
Figure 5.3: test

Figure 5.4: Emission scan of fresh and aggregated FG124 in crowded conditions. Data normalized by subtracting blank sample.



5.1.2 Fluorimetry

We hypothesized that the crowder-dependent difference in aggregation might arise from the aromatic ring in PVP, which could interact with the phenylalanine in FG124 in a ring-stacking interaction. To test this idea, I collected emission spectra of fresh and aggregated FG124 in PEG and PVP crowders near the phenylalanine peak wavelength (see Fig. 5.4). Only 5% PEG and PVP in PTB were tested because PEG has a peak near the FG124 peak which dominates at higher PEG concentrations. Data were normalized by averaging over two runs and subtracting a blank run (containing crowder and buffer but no protein). The PEG sample showed the largest difference upon aggregation, both in peak height and location. Figure 5.5 shows the same data, normalized to a maximum amplitude of one and offset, in order to emphasize the changes in peak shape. In both crowder conditions, but not in the buffer condition, a small peak appears in the aggregated FG124 near 310 nm.

Additionally, I compared the phenylalanine peaks in FSFG and fresh and aggregated FG124 to those of pure phenylalanine [?], as seen in Fig. 5.6. Data are blanked and normalized to a maximum intensity of one. The peak slightly shifts toward longer wavelengths as the data progress from phenylalanine to FSFG to fresh and aggregated FG124. I also measured PEG and PVP

Figure 5.5: Emission scan of phenylalanine, FSFG, and FG124. Excited at 240 nm. Phe data is not mine, need to check reference. Data normalized to a maximum amplitude of 1.

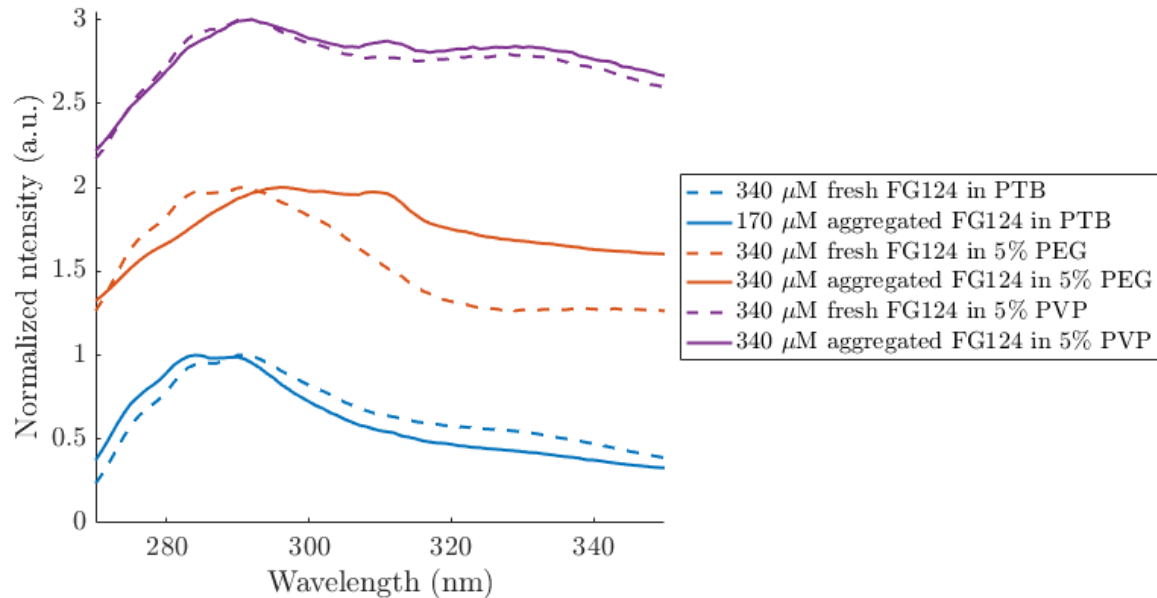


Figure 5.6: Emission scan of phenylalanine, FSFG, and FG124. Excited at 240 nm. Phe data is not mine, need to check reference. Data normalized to a maximum amplitude of 1.

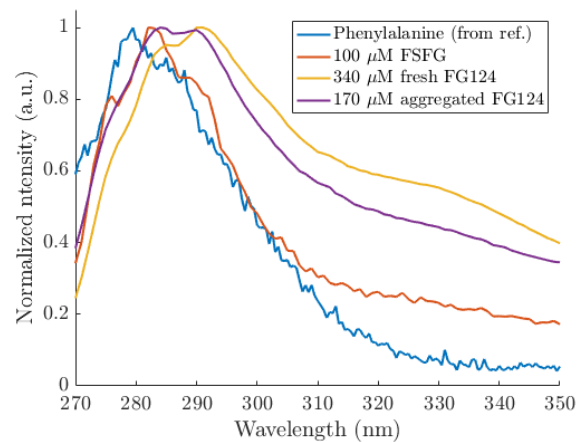
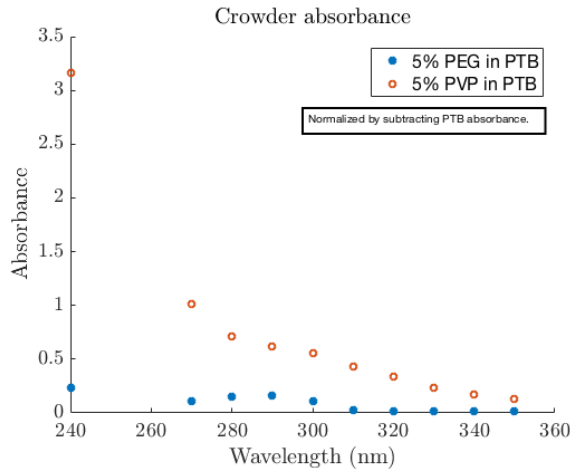


Figure 5.7: Absorbance of 5% PEG and PVP solutions in PTB. Normalized by subtracting PTB absorbance.



absorbance near 240 nm (see Fig. 5.7). PVP has a very high absorbance in that range, which might explain why the recorded counts were lowest for the PVP conditions.

5.2 Discussion

It's possible that the differences in aggregation time between PEG and PVP come from changes in viscosity. The two samples do have widely different viscosity, as measured by Steve Whitten. A 13% PEG solution in PTB has a dynamic viscosity of 15.87 mPa s, while that of a 13% PVP solution in PTB is 7.34 mPa s. The literature doesn't entirely agree on what happens to aggregation as a function of viscosity, but what we see could be due to that change. (Check in lab book where I have lit search notes.)

5.3 Materials and Methods

5.3.1 Buffers

Potassium transport buffer (PTB) (150 mM KCl, 20 mM HEPES, 2 mM MgCl₂) was used for all timecourse and NMR samples.

5.3.2 FG124 preparation

His-tagged FG124 was expressed in *E. coli* in the plasmid pRSF. Cultures were grown in LB and induced at 37 degrees C for 2-4 hr with 1 mM IPTG at OD 0.6-0.8. Periplasmic matrix was removed prior to lysis. Cells were then lysed via sonication and FG124 purified using TALON cobalt resin. All purification buffers were PTB with 7M GuHCl and PIC. The elution buffer also contained 250 mM imidazole.

5.3.3 Timecourse preparation

Stocks of PEG and PVP in PTB were prepared at 20 or 40% w/v; serine stocks were prepared at 30% w/v. PEG and serine were at pH 7; PVP was pH 7 or pH 5. A pH series with no crowding agent showed no significant differences based on pH. Lyophilized lysate was prepared by homogenizing BL21 DE3 Gold cells and spinning them down. The supernatant was lyophilized in a decomposing ammonium bicarbonate buffer and resuspended in PTB to the desired concentration when needed. A 10 mM stock solution of ThT in PTB was prepared and filtered no more than a week before the timecourse, stored at room temperature and protected from light. Immediately prior to starting the timecourse, FG124 was desalted into PTB to remove the imidazole and GuHCl. Samples were promptly prepared containing the appropriate percentage of crowder, a final concentration of 1-2 mg/mL FG124, and 200 uM thioflavin T. All samples in the same timecourse had the same concentration of FG124, including the buffer sample, which contained no crowding agent. Blanks were prepared with crowding agent and thioflavin T, but no FG124. Samples were pipetted into black, flat-bottomed, clear-bottomed 96-well plates with 150 uL per replicate. Each sample yielded four to six replicates. Only one blank replicate was used per condition. One negative control and corresponding blank were prepared per timecourse containing 7M GuHCl and no crowding agent but using the same protein sample as all other conditions. Each well contained a 3mm-diameter glass or teflon bead. The plate was sealed with a PCR seal and taken to a Safire II plate reader. The fluorescence was measured from the bottom at 10-minute intervals with an

excitation wavelength of 450 nm, emission wavelength of 482 nm, and 5 nm bandwidths. The plate shooook orbitally at high speed between measurements and was held at a temperature of 30 degrees C. The time between desalting and beginning the plate reader measurements was typically about an hour; the time of desalting was taken as $t = 0$ for the purposes of calculating lag time. In parallel with the sample preparation, the concentration of the desalted FG124 was measured with a BCA assay.

5.3.4 NMR sample preparation

5.3.5 NMR experiments

5.3.6 Fluorimetry

FG124 was purified as described above and stored in PTB with 7M GuHCl. Immediately before use, 130 uL of 520 uM FG124 was desalted with a Zeba spin desalting column to remove the GuHCl. The resulting stock was used in the crowder samples, which had a final concentration of 340 uM Fg124. I used the shared-instrumentation fluorimeter. I tested PTB, 5% PEG (MW, source, purity?) in PTB, and 5% PVP (same questions?) in PTB as blanks. I measured 340 uM FG124 in PTB and the two crowders as well. Between runs, I cleaned the cuvette (micro quartz cuvette from Kaar lab (sample volume?)) with ethanol 3x, then 5x with DI water, and gently blotted the outside with ethanol. Fluorimeter settings: 4 nm slits, 1000 V PMT, excitation wavelength of 240 nm. Step size = 1nm, average over 2 runs. After taking this data with fresh FG124, I let the samples sit at room temp overnight to aggregate (no shaking) and most were cloudy in the morning. I took similar data with the aggregated samples. I needed to rinse with 7M GuHCl, let soak in 7M GuHCl for 5 minutes, and then perform the same cleaning procedure as the previous day in order to remove the aggregates from the cuvette.

Bibliography

- [1] M. Beck and E. Hurt. The nuclear pore complex: Understanding its function through structural insight. *Nature Reviews Molecular Cell Biology*, 18(2):73–89, February 2017.
- [2] G. J. Stanley, A. Fassati, and B. W. Hoogenboom. Biomechanics of the transport barrier in the nuclear pore complex. *Seminars in Cell & Developmental Biology*, 68:42–51, August 2017.
- [3] L.-C. Tu and S. M. Musser. Single Molecule Studies of Nucleocytoplasmic Transport. *Biochimica et biophysica acta*, 1813(9):1607–1618, September 2011.
- [4] L. E. Kapinos, B. Huang, C. Rencurel, and R. Y. H. Lim. Karyopherins regulate nuclear pore complex barrier and transport function. *J Cell Biol*, page jcb.201702092, September 2017.
- [5] S. H. Yoshimura and T. Hirano. HEAT repeats – versatile arrays of amphiphilic helices working in crowded environments? *J Cell Sci*, 129(21):3963–3970, November 2016.
- [6] K. Ribbeck and D. Görlich. Kinetic analysis of translocation through nuclear pore complexes. *The EMBO Journal*, 20(6):1320–1330, March 2001.
- [7] J. P. Siebrasse and R. Peters. Rapid translocation of NTF2 through the nuclear pore of isolated nuclei and nuclear envelopes. *EMBO Reports*, 3(9):887–892, September 2002.
- [8] N. I. Kiskin, J. P. Siebrasse, and R. Peters. Optical Micowell Assay of Membrane Transport Kinetics. *Biophysical Journal*, 85(4):2311–2322, October 2003.
- [9] A. Paradise, M. K. Levin, G. Korza, and J. H. Carson. Significant proportions of nuclear transport proteins with reduced intracellular mobilities resolved by fluorescence correlation spectroscopy. *Journal of molecular biology*, 365(1):50–65, January 2007.
- [10] T. Dange, D. Grünwald, A. Grünwald, R. Peters, and U. Kubitscheck. Autonomy and robustness of translocation through the nuclear pore complex: A single-molecule study. *J Cell Biol*, 183(1):77–86, October 2008.
- [11] U. Kubitscheck, D. Grünwald, A. Hoekstra, D. Rohleder, T. Kues, J. P. Siebrasse, and R. Peters. Nuclear transport of single molecules: Dwell times at the nuclear pore complex. *The Journal of Cell Biology*, 168(2):233–243, January 2005.
- [12] A. Zilman, S. D. Talia, B. T. Chait, M. P. Rout, and M. O. Magnasco. Efficiency, Selectivity, and Robustness of Nucleocytoplasmic Transport. *PLOS Computational Biology*, 3(7):e125, July 2007.

- [13] M. P. Rout, J. D. Aitchison, A. Suprapto, K. Hjertaas, Y. Zhao, and B. T. Chait. The Yeast Nuclear Pore Complex Composition, Architecture, and Transport Mechanism. *The Journal of Cell Biology*, 148(4):635–652, February 2000.
- [14] S. Frey and D. Görlich. A Saturated FG-Repeat Hydrogel Can Reproduce the Permeability Properties of Nuclear Pore Complexes. *Cell*, 130(3):512–523, August 2007.
- [15] A. Vovk, C. Gu, M. G. Opferman, L. E. Kapinos, R. Y. Lim, R. D. Coalson, D. Jasnow, and A. Zilman. Simple biophysics underpins collective conformations of the intrinsically disordered proteins of the Nuclear Pore Complex. *eLife*, 5:e10785, May 2016.
- [16] H. B. Schmidt and D. Görlich. Nup98 FG domains from diverse species spontaneously phase-separate into particles with nuclear pore-like permselectivity. *eLife*, 4:e04251, January 2015.
- [17] J. Yamada, J. L. Phillips, S. Patel, G. Goldfien, A. Calestagne-Morelli, H. Huang, R. Reza, J. Acheson, V. V. Krishnan, S. Newsam, A. Gopinathan, E. Y. Lau, M. E. Colvin, V. N. Uversky, and M. F. Rexach. A bimodal distribution of two distinct categories of intrinsically disordered structures with separate functions in FG nucleoporins. *Molecular & cellular proteomics: MCP*, 9(10):2205–2224, October 2010.
- [18] A. R. Lowe, J. H. Tang, J. Yassif, M. Graf, W. Y. Huang, J. T. Groves, K. Weis, and J. T. Liphardt. Importin- β modulates the permeability of the nuclear pore complex in a Ran-dependent manner. *eLife*, 4:e04052, March 2015.
- [19] R. L. Schoch, L. E. Kapinos, and R. Y. H. Lim. Nuclear transport receptor binding avidity triggers a self-healing collapse transition in FG-nucleoporin molecular brushes. *Proceedings of the National Academy of Sciences of the United States of America*, 109(42):16911–16916, October 2012.
- [20] L. E. Hough, K. Dutta, S. Sparks, D. B. Temel, A. Kamal, J. Tetenbaum-Novatt, M. P. Rout, and D. Cowburn. The molecular mechanism of nuclear transport revealed by atomic-scale measurements. *eLife*, 4:e10027, September 2015.
- [21] J. Pulupa, M. Rachh, M. D. Tomasini, J. S. Mincer, and S. M. Simon. A coarse-grained computational model of the nuclear pore complex predicts Phe-Gly nucleoporin dynamics. *The Journal of General Physiology*, page jgp.201711769, September 2017.
- [22] T. Bickel and R. Bruinsma. The Nuclear Pore Complex Mystery and Anomalous Diffusion in Reversible Gels. *Biophysical Journal*, 83(6):3079–3087, December 2002.
- [23] J. Witten and K. Ribbeck. The particle in the spider’s web: Transport through biological hydrogels. *Nanoscale*, May 2017.
- [24] S. Pagliara, S. L. Dettmer, and U. F. Keyser. Channel-facilitated diffusion boosted by particle binding at the channel entrance. *Physical Review Letters*, 113(4):048102, July 2014.
- [25] M. Tagliazucchi, O. Peleg, M. Kroeger, Y. Rabin, and I. Szleifer. Effect of charge, hydrophobicity, and sequence of nucleoporins on the translocation of model particles through the nuclear pore complex. *Proceedings of the National Academy of Sciences of the United States of America*, 110(9):3363–3368, February 2013. WOS:000315841900039.

- [26] L.-C. Tu, G. Fu, A. Zilman, and S. M. Musser. Large cargo transport by nuclear pores: Implications for the spatial organization of FG-nucleoporins. *The EMBO journal*, 32(24):3220–3230, December 2013.
- [27] B. L. Timney, B. Raveh, R. Mironská, J. M. Trivedi, S. J. Kim, D. Russel, S. R. Wente, A. Sali, and M. P. Rout. Simple rules for passive diffusion through the nuclear pore complex. *J Cell Biol*, 215(1):57–76, October 2016.
- [28] J. S. Mincer and S. M. Simon. Simulations of nuclear pore transport yield mechanistic insights and quantitative predictions. *Proceedings of the National Academy of Sciences of the United States of America*, 108(31):E351–358, August 2011.
- [29] D. Gilchrist, B. Mykytka, and M. Rexach. Accelerating the Rate of Disassembly of Karyopherin-Cargo Complexes. *Journal of Biological Chemistry*, 277(20):18161–18172, May 2002.
- [30] B. L. Timney, J. Tetenbaum-Novatt, D. S. Agate, R. Williams, W. Zhang, B. T. Chait, and M. P. Rout. Simple kinetic relationships and nonspecific competition govern nuclear import rates *in vivo*. *J Cell Biol*, 175(4):579–593, November 2006.
- [31] S. Milles, D. Mercadante, I. V. Aramburu, M. R. Jensen, N. Banterle, C. Koehler, S. Tyagi, J. Clarke, S. L. Shammas, M. Blackledge, F. Gräter, and E. A. Lemke. Plasticity of an Ultrafast Interaction between Nucleoporins and Nuclear Transport Receptors. *Cell*, 163(3):734–745, October 2015.
- [32] B. Raveh, J. M. Karp, S. Sparks, K. Dutta, M. P. Rout, A. Sali, and D. Cowburn. Slide-and-exchange mechanism for rapid and selective transport through the nuclear pore complex. *Proceedings of the National Academy of Sciences*, 113(18):E2489–E2497, May 2016.
- [33] R. Y. H. Lim, B. Fahrenkrog, J. Köser, K. Schwarz-Herion, J. Deng, and U. Aebi. Nanomechanical Basis of Selective Gating by the Nuclear Pore Complex. *Science*, 318(5850):640–643, October 2007.
- [34] S. Milles and E. A. Lemke. Mapping Multivalency and Differential Affinities within Large Intrinsically Disordered Protein Complexes with Segmental Motion Analysis. *Angewandte Chemie International Edition*, 53(28):7364–7367, July 2014.
- [35] J. Howard. *Mechanics of Motor Proteins and Cytoskeleton*. Sinauer Associates, 1st edition, 2001.
- [36] V. Receveur-Bréchot and D. Durand. How Random are Intrinsically Disordered Proteins? A Small Angle Scattering Perspective. *Current Protein & Peptide Science*, 13(1):55–75, February 2012.
- [37] J. Tetenbaum-Novatt, L. E. Hough, R. Mironská, A. S. McKenney, and M. P. Rout. Nucleocytoplasmic Transport: A Role for Nonspecific Competition in Karyopherin-Nucleoporin Interactions. *Molecular & Cellular Proteomics : MCP*, 11(5):31–46, May 2012.
- [38] R. Blackwell, C. Edelmaier, O. Sweezy-Schindler, A. Lamson, Z. R. Gergely, E. O'Toole, A. Crapo, L. E. Hough, J. R. McIntosh, M. A. Glaser, and M. D. Betterton. Physical determinants of bipolar mitotic spindle assembly and stability in fission yeast. *Science Advances*, 3(1):e1601603, January 2017.

- [39] J. Braga, J. G. McNally, and M. Carmo-Fonseca. A Reaction-Diffusion Model to Study RNA Motion by Quantitative Fluorescence Recovery after Photobleaching. *Biophysical Journal*, 92(8):2694–2703, April 2007.
- [40] M. Kim, W. G. Chen, J. W. Kang, M. J. Glassman, K. Ribbeck, and B. D. Olsen. Artificially Engineered Protein Hydrogels Adapted from the Nucleoporin Nsp1 for Selective Biomolecular Transport. *Advanced materials (Deerfield Beach, Fla.)*, 27(28):4207–4212, July 2015.
- [41] S. Chatani, T. Gong, B. A. Earle, M. Podgórska, and C. N. Bowman. Visible-Light Initiated Thiol-Michael Addition Photopolymerization Reactions. *ACS Macro Letters*, 3(4):315–318, April 2014.
- [42] D. P. Nair, M. Podgrski, S. Chatani, T. Gong, W. Xi, C. R. Fenoli, and C. N. Bowman. The thiol-michael addition click reaction: A powerful and widely used tool in materials chemistry. *Chemistry of Materials*, 26(1):724–744, 2014.
- [43] B. D. Fairbanks, M. P. Schwartz, C. N. Bowman, and K. S. Anseth. Photoinitiated polymerization of PEG-diacrylate with lithium phenyl-2,4,6-trimethylbenzoylphosphinate: Polymerization rate and cytocompatibility. *Biomaterials*, 30(35):6702–6707, December 2009.
- [44] D. Bartolo, G. Degré, P. Nghe, and V. Studer. Microfluidic stickers. *Lab on a Chip*, 8(2):274–279, January 2008.
- [45] J. S. Paustian, R. N. Azevedo, S.-T. B. Lundin, M. J. Gilkey, and T. M. Squires. Microfluidic Microdialysis: Spatiotemporal Control over Solution Microenvironments Using Integrated Hydrogel Membrane Microwindows. *Physical Review X*, 3(4), November 2013.
- [46] M. Bruchet and A. Melman. Fabrication of patterned calcium cross-linked alginate hydrogel films and coatings through reductive cation exchange. *Carbohydrate Polymers*, 131:57–64, October 2015.
- [47] S. De and D. Robinson. Polymer relationships during preparation of chitosan-alginate and poly-l-lysine-alginate nanospheres. *Journal of Controlled Release*, 89(1):101–112, April 2003.
- [48] M. A. Masuelli. Dextrans in Aqueous Solution. Experimental Review on Intrinsic Viscosity Measurements and Temperature Effect. *Journal of Polymer and Biopolymer Physics Chemistry*, 1(1):13–21, January 2013.
- [49] C. Chaillan-Huntington, P. J. G. Butler, J. A. Huntington, D. Akin, C. Feldherr, and M. Stewart. NTF2 monomer-dimer equilibrium1. *Journal of Molecular Biology*, 314(3):465–477, November 2001.
- [50] M. M. Picken and G. A. Herrera. Thioflavin T Stain: An Easier and More Sensitive Method for Amyloid Detection. In M. M. P. M. FASN, A. D. M.D, and G. A. H. M.D, editors, *Amyloid and Related Disorders*, Current Clinical Pathology, pages 187–189. Humana Press, 2012.
- [51] R. Khurana, C. Coleman, C. Ionescu-Zanetti, S. A. Carter, V. Krishna, R. K. Grover, R. Roy, and S. Singh. Mechanism of thioflavin T binding to amyloid fibrils. *Journal of Structural Biology*, 151(3):229–238, September 2005.
- [52] M. Groenning. Binding mode of Thioflavin T and other molecular probes in the context of amyloid fibrils—current status. *Journal of Chemical Biology*, 3(1):1–18, August 2009.

- [53] A. N. Murray, F. L. Palhano, J. Bieschke, and J. W. Kelly. Surface adsorption considerations when working with amyloid fibrils in multiwell plates and Eppendorf tubes. *Protein Science*, 22(11):1531–1541, November 2013.

Appendix A

Appendix test

test appendix

Appendix B

Second virial approximation

DDFT requires approximation of the excess free energy [?]. In general, the excess free energy can be expressed as a perturbative expansion of integrals of the one-body density and the Mayer function [?]

$$\mathcal{F}^{\text{ex}} = \frac{1}{2} \int \int \rho(\mathbf{r}) \rho(\mathbf{r}') F_M(\mathbf{r} - \mathbf{r}') d\mathbf{r}' d\mathbf{r} \quad (\text{B.1})$$

$$+ \frac{1}{6} \int \int \int \rho(\mathbf{r}) \rho(\mathbf{r}') \rho(\mathbf{r}'') F_M(\mathbf{r} - \mathbf{r}') F_M(\mathbf{r}' - \mathbf{r}'') F_M(\mathbf{r} - \mathbf{r}'') d\mathbf{r} d\mathbf{r}' d\mathbf{r}'' \quad (\text{B.2})$$

$$+ \dots \quad (\text{B.3})$$

where $F_M = \exp(-\beta V) - 1$ is the Mayer function. This is the virial expansion. At low density, the free energy is given by the second virial approximation

$$\mathcal{F}^{\text{ex}} \approx -\frac{k_B T}{2} \int \int \rho(\mathbf{r}) \rho(\mathbf{r}') F_M(\mathbf{r} - \mathbf{r}') d\mathbf{r}' d\mathbf{r}. \quad (\text{B.4})$$

In the second virial approximation, the direct pair correlation function is

$$c^{(2)}(\mathbf{r}, \mathbf{r}') = -\beta \frac{\delta^2 \mathcal{F}}{\delta \rho(\mathbf{r}) \delta \rho(\mathbf{r}')} \approx F_M(\mathbf{r} - \mathbf{r}'). \quad (\text{B.5})$$

Consider steric interactions where overlap is forbidden. In this approximation,

$$c^{(2)}(\mathbf{r} - \mathbf{r}') = \begin{cases} -1 & \text{particles overlap} \\ 0 & \text{no overlap} \end{cases}. \quad (\text{B.6})$$

Thus in the second virial approximation, the correlations are approximated as correlation holes at distances corresponding to particle overlap, and non-overlapping particles are completely uncorrelated. Note that for a finite potential at high temperature, we can Taylor expand the Mayer

function to give

$$-\beta \mathcal{F}^{\text{ex}} \approx \frac{1}{2} \int \int \rho(\mathbf{r})\rho(\mathbf{r}')V(\mathbf{r} - \mathbf{r}') \, d\mathbf{r}' \, d\mathbf{r}, \quad (\text{B.7})$$

which is the mean field (random-phase) approximation [?]. For anisotropic particles, the Mayer function depends on the orientation $\hat{\mathbf{u}}$ of each particle, $F_M(\mathbf{r} - \mathbf{r}') \rightarrow F_M(\mathbf{r} - \mathbf{r}', \hat{\mathbf{u}}, \hat{\mathbf{u}}')$.

For spherocylinders in 2D, including finite width in the Mayer function in Eqn. ?? amounts to adding a constant to the free energy, which drops when taking the functional derivative. Therefore, the second virial approximation can only model the infinitely thin rod system.

Appendix C

Numerics for Brownian dynamics simulations

Here, I connect the Langevin equation and Brownian dynamics simulations [?]. The Brownian equation of motion is

$$\dot{x} = -\zeta^{-1} [f(x, t) + \xi(t)], \quad (\text{C.1})$$

where the force $f(x, t) = -\frac{dU}{dx}$ depends on time and the noise has the properties

$$\langle \xi(t) \rangle = 0, \quad (\text{C.2})$$

$$\langle \xi(t) \xi(t') \rangle = 2\zeta k_B T \delta(t - t'). \quad (\text{C.3})$$

Integrating from t to $t + \delta t$ gives

$$x(t + \delta t) = x(t) - \zeta^{-1} \int_t^{t+\delta t} dt' f(x, t') + \xi(t'). \quad (\text{C.4})$$

To numerically evaluate this, we approximate the delta function in the noise term variance (Eqn. ??) as

$$\delta(t - t') \approx \delta(t, t') = \begin{cases} \frac{1}{\delta t}, & \text{if } t \text{ and } t' \text{ are in the same time step } \delta t \\ 0, & \text{otherwise} \end{cases}. \quad (\text{C.5})$$

Thus, upon integration we get

$$x(t + \delta t) \approx x(t) - \zeta^{-1} \delta t \left[f(t) + c(t) \sqrt{\frac{2\zeta k_B T}{\delta t}} \right]. \quad (\text{C.6})$$

where $c(t)$ is a random number selected from a distribution with average zero and variance 1.

Typically, we select a number from the uniform distribution $r \in [-1/2, 1/2]$ which has a variance

of $1/12$. Thus, the position at time t_{n+1} is

$$x_{n+1} \approx x_n - \zeta^{-1} \delta t f_n + \sqrt{24D\delta t} r_n, \quad (\text{C.7})$$

where we have used the Einstein relation $D = \frac{k_B T}{\zeta}$. At each time step, f_n is calculated, and r_n is selected. In the absence of forces, the MSD is

$$\langle x_N^2 \rangle = 24D\delta t \langle r^2 \rangle N = 2Dt, \quad (\text{C.8})$$

after $N = t/\delta t$ steps. A step is randomly selected from a uniform distribution $\Delta x \in [-\sqrt{6D\delta t}, \sqrt{6D\delta t}]$ in a Brownian dynamics simulation. Note that one can select a random number from a Gaussian distribution instead of a uniform distribution. In that case, a random step length is selected from a Gaussian distribution with average $\mu = 0$ and variance $\sigma = \sqrt{2D\delta t}$.

Appendix D

Derivation of DDFT

This appendix describes how to go from the Smoluchowski equation to a closed form for the one-particle density using dynamic density functional theory [?]. The Smoluchowski equation describes the evolution of the N particle density $\rho^{(N)}(\mathbf{r}^N, t)$, the probability of finding the particles near $\mathbf{r}^N = [\mathbf{r}_1, \mathbf{r}_2, \dots, \mathbf{r}_N]$ in phase space, is

$$\frac{\partial \rho^{(N)}(\mathbf{r}^N, t)}{\partial t} = \nabla_i \left[\zeta_{ij}^{-1} \nabla_j U(\mathbf{r}^N, t) \rho^{(N)}(\mathbf{r}^N, t) \right] + \nabla_i D_{ij} \nabla_j \rho^{(N)}(\mathbf{r}^N, t), \quad (\text{D.1})$$

where U is the potential. In general,

$$U(\mathbf{r}^N, t) = \sum_{i=1}^N V_{\text{ext}}(\mathbf{r}_i, t) + \frac{1}{2} \sum_{j \neq i} \sum_{i=1}^N v_2(\mathbf{r}_i, \mathbf{r}_j) + \frac{1}{6} \sum_{k \neq j \neq i} \sum_{j \neq i} \sum_{i=1}^N v_3(\mathbf{r}_i, \mathbf{r}_j, \mathbf{r}_k) + \dots \quad (\text{D.2})$$

where V_{ext} is the potential from external fields and v_n is the n -body interaction potential. We are deriving an equation for the one-body density

$$\rho^{(1)}(\mathbf{r}) = N \int d\mathbf{r}_2 \dots \int d\mathbf{r}_N \rho^{(N)}(\mathbf{r}^N), \quad (\text{D.3})$$

which describes the probability of finding a particle at position \mathbf{r} irrespective of the other particles' locations. In general, the n -body particle density is [?]

$$\rho^{(n)}(\mathbf{r}^n) = \frac{N!}{(N-n)!} \int d\mathbf{r}_{n+1} \int d\mathbf{r}_N \rho^{(N)}(\mathbf{r}^N, t). \quad (\text{D.4})$$

We can integrate the Smoluchowski equation over coordinates $\mathbf{r}_2, \dots, \mathbf{r}_N$ to get

$$\frac{\partial \rho^{(1)}(\mathbf{r}_1, t)}{\partial t} = \nabla_1 D \nabla_1 \rho^{(1)}(\mathbf{r}_1, s) + \zeta^{-1} \nabla_1 \left(\rho^{(1)}(t) \nabla_1 V_{\text{ext}} \right) \quad (\text{D.5})$$

$$+ \nabla_1 D \int d\mathbf{r}_2 \rho^{(2)}(\mathbf{r}_1, \mathbf{r}_2) \nabla_1 v_2(\mathbf{r}_1, \mathbf{r}_2) \quad (\text{D.6})$$

$$+ \nabla_1 D \int d\mathbf{r}_2 \int d\mathbf{r}_3 \rho^{(3)}(\mathbf{r}_1, \mathbf{r}_2, \mathbf{r}_3) \nabla_1 v_3(\mathbf{r}_1, \mathbf{r}_2, \mathbf{r}_3) + \dots \quad (\text{D.7})$$

This is not a closed equation because the evolution of $\rho^{(1)}$ depends on the higher order densities $\rho^{(2)}, \dots, \rho^{(n)}$. Evans found a way to express the two-body density in terms of the direct correlation function $-k_B T \rho^{(1)}(\mathbf{r}_1) \nabla_1 c^{(1)}(\mathbf{r}_1) = \int d\mathbf{r}_2 \rho^{(2)}(\mathbf{r}_1, \mathbf{r}_2) \nabla_1 v_2(\mathbf{r}_1, \mathbf{r}_2)$ for a liquid in equilibrium [?].

This can be generalized for higher order terms [?] to give

$$-k_B T \rho^{(1)}(\mathbf{r}_1) \nabla_1 c^{(1)}(\mathbf{r}_1) = \sum_n \int d\mathbf{r}_2 \dots \int d\mathbf{r}_n \rho^{(n)} \nabla_1 v_n(\mathbf{r}^n). \quad (\text{D.8})$$

Plugging this into Eqn. ?? gives a closed form for our equations if $c^{(1)}$ is known and not dependent on higher order densities. The direct correlation function in equilibrium can be expressed as a functional derivative of the excess free energy, *i.e.*, free energy contribution from interactions, with respect to the single body free energy [?, ?, ?, ?]

$$c^{(1)}(\mathbf{r}) = -\beta \frac{\delta \mathcal{F}^{\text{ex}} [\rho^{(1)}(\mathbf{r})]}{\delta \rho^{(1)}(\mathbf{r})}. \quad (\text{D.9})$$

This assumes that Eqn. ?? and ?? are valid for a fluid out of equilibrium [?]. This gives the DDFT equation of motion [?, ?, ?, ?]

$$\frac{\partial \rho(\mathbf{r}, t)}{\partial t} = \nabla \cdot \left[\zeta^{-1} \rho(\mathbf{r}, t) \nabla \frac{\delta \mathcal{F}[\rho(\mathbf{r}, t)]}{\delta \rho(\mathbf{r}, t)} \right], \quad (\text{D.10})$$

where we have dropped the superscript (1) from the one-body density. The free energy is separable into contributions from the ideal gas entropy, excess/interactions, and external fields [?]

$$\mathcal{F} = \mathcal{F}^{\text{id}} + \mathcal{F}^{\text{ex}} + \mathcal{F}^{\text{ext}}. \quad (\text{D.11})$$

The ideal gas and external contributions are exact [?, ?]:

$$\mathcal{F}^{\text{id}} = k_B T \int d\mathbf{r}^d \rho(\mathbf{r}) \left[\ln \Lambda^d \rho(\mathbf{r}) - 1 \right], \quad (\text{D.12})$$

where Λ is the thermal de Broglie wavelength and

$$\mathcal{F}^{\text{ext}} = \sum_{i=1}^N V_{\text{ext}}(\mathbf{r}_i, t). \quad (\text{D.13})$$

The excess free energy is not necessarily known and may be approximated [?]. DDFT, although built on the stochastic Langevin equation, is deterministic [?] because we have taken the noise ensemble average.